

## Chapter 4: Analysis of the dynamic response of large cages considering the influence of disturbed wave fields on nets under regular waves

### 4.1 introduction

At present, the most widely used mariculture structure is still the traditional gravity cage [109, 151, 152]. Because the main structure of the whole gravity cage is a net coat and a slender floating ring, the characteristic size of each component is much smaller than the wavelength, and there are no other large-scale components in the cage, so in the hydrodynamic analysis of the cage, it can be considered that the cage is only affected by the incident wave, ignoring the influence of the cage structure on the flow field, that is, the flow field is only generated by the incident wave, and there is no diffraction wave and radiation wave.

In recent years, with the vigorous development of marine aquaculture, the offshore aquaculture industry has become saturated<sup>[153]</sup>, and marine aquaculture has gradually shifted to the deep sea<sup>[14, 154]</sup>. For this reason, the deep-sea large-scale floating aquaculture structure, which is more suitable for the open sea, has developed rapidly. In order to ensure the safe operation of large cages, it is necessary to evaluate the loads of each part of the cages under various sea conditions. Large cage is an emerging large-scale marine aquaculture structure composed of large floating bodies, nets and steel frames. Different from traditional culture cages, huge buoys generate diffraction waves and radiation waves in waves, which together with the incident waves of the wave field form the disturbed wave field around the cage. The disturbance of the wave field will lead to the change of the velocity point velocity of the water quality point in the velocity field, which will cause a significant change in the flow field velocity around the net, which in turn will affect the hydrodynamic load of the net and the strength of the main steel structure. With the development of large-scale cages in the world in recent years, some scholars have also carried out some studies on the hydrodynamic response and structural strength verification of large-scale cages. At present, the research on large cages uses the potential flow theory to solve the hydrodynamic load and hydrodynamic coefficient of the float in the frequency domain, and then converts it into the hydrodynamic load in the time domain by a certain method, but the influence of the diffraction wave and radiation wave generated by the float on the hydrodynamic load of the net coat is not considered in the calculation of the net load in the time domain analysis. In order to simplify the description, the disturbance wave field is used to represent the wave field after considering the diffraction wave and the radiation wave generated by the floating body, that is, the wave field composed of the incident wave, the diffraction wave and the radiation wave.

In this chapter, the influence of the buoys on the velocity field of the regular waves around the net is analyzed by using the three-dimensional potential flow theory, considering the influence of the diffracted waves and radiated waves of the buoys, and the influence of the floating disturbance on the velocity field of the regular waves around the net is analyzed by using the established coupled large-scale cage model including rigid buoys, flexible meshes, steel frames and mooring systems, and the numerical methods are used to analyze the time domain of the large cages under the action of the disturbance regular wave field, and the influence of the floating disturbance on the tension of the network cable and the bearing of the connector under the action of the regular wave is studied. At the same time, the finite element model of the main steel structure (including the floating body and the steel frame) was established, and the strength analysis of the main steel structure considering the influence of the floating body on the net load under regular wave was carried out based on the quasi-static method.

## 4.2 Dynamic analysis theory of large cage considering the influence of perturbation wave field on net coat under regular wave

The main hydrodynamic bearing components of the large-scale cage studied in this paper include two parts: a flexible mesh coat and a main steel structure, in which the main steel structure includes a floating body and a steel frame. Due to the large main scale of the buoy, according to the analysis results in Chapter 3, the influence of fluid viscosity on the buoy under wave action can be ignored. However, as a typical slender structure, the viscous effect of the fluid is significant, and the diffraction effect of the wave is negligible. Therefore, the potential flow theory is used in this chapter to obtain the load of the floating body under the action of waves, while the hydrodynamic load of the steel frame and net clothing is still calculated by Morrison's formula.

### 4.2.1 Solve the disturbance wave field considering the influence of buoy disturbance under regular waves

- (1) A method for solving the disturbance wave field considering the influence of floating body disturbance under regular waves

Under the regular wave, the presence and motion of the floating body will produce diffraction wave and radiation wave respectively, which will disturb the velocity distribution of the water quality point in the wave field, thereby directly leading to the change of the hydrodynamic force of the net. The disturbance wave field is obtained by the linear superposition of incident waves, diffraction waves, and radiation waves, so it can be assumed that in the wave field after disturbance, the water quality point velocity  $\mathbf{v}$  is obtained by the **linear superposition of the water quality point velocity generated by the incident wave, the diffraction wave, and the radiation wave**.

$$\mathbf{v} = \mathbf{v}_I + \mathbf{v}_D + \mathbf{v}_R = [v_x \quad v_{Ard} \quad v_{With}]^T \quad (4-1)$$

where  $\mathbf{vI}$ ,  $\mathbf{vD}$ , and  $\mathbf{vR}$  are expressed as the water quality point velocity vectors generated by the incident wave, diffracted wave, and radiation wave, respectively  
 $vX$ ,  $vY$ , and  $vZ$  represent the velocity components of the water quality point velocity  $\mathbf{v}$  in the  $X$ ,  $Y$ , and  $Z$  directions, respectively.

The wave used in this article is a linear wave (Airy wave), so the water quality point velocity  $\mathbf{vI}$  produced by the incident wave can be expressed as:

$$\mathbf{v} = \begin{pmatrix} \mathbf{v}_I \\ \mathbf{v}_{I2} \\ \mathbf{v}_{I3} \end{pmatrix} = \begin{pmatrix} \zeta_A |_{TF1} \sin(\omega\tau + \theta_A) \\ \zeta_A |_{TF2} \sin(\omega\tau + \theta_A) \\ \zeta_A |_{TF3} \sin(\omega\tau + \theta_A) \end{pmatrix} \quad (4-2)$$

where  $vI_1$ ,  $vI_2$ , and  $vI_3$  denote the components of  $\mathbf{vI}$  in the  $X$ ,  $Y$ , and  $Z$  directions,

respectively.  $\zeta_A$  denotes the amplitude of the incident wave.  $\theta_{Ik}$

Indicates that the wave surface is in  $k$  Direction ( $k = 1, 2, 3$ ) of the phase angle. For the incident wave in  $k$  Direction ( $k = 1, 2, 3$ ) caused

The velocity field transfer function. Operator  $| |$  indicates the amplitude of the parameter.

The superscript I represents the parameter corresponding to the incident wave. The

subscripts 1, 2, and 3 represent the components in the  $X$ ,  $Y$ , and  $Z$  directions, respectively.

The water quality point velocity  $v_D$  produced by the diffracted wave can be expressed as:

$$\mathbf{v}_D = \left\{ v_D^1, v_D^2, v_D^3 \right\} = \left\{ \begin{array}{l} \zeta v D_{TFI}^1 \sin(\omega \tau + \theta_{D1}) \\ \zeta v D_{TFI}^2 \sin(\omega \tau + \theta_{D2}) \\ \zeta v D_{TFI}^3 \sin(\omega \tau + \theta_{D3}) \end{array} \right\} \quad (4-3)$$

where  $vD1$ ,  $vD2$ , and  $vD3$  represent the components of  $vD$  in the  $X$ ,  $Y$ , and  $Z$  directions, respectively.  $\theta_{\Delta k}$  indicates that the diffracted wave is in the  $k$  direction

The velocity of the water quality point in the direction of  $(k=1, 2, 3)$  and the phase angle of the wave surface.  $vD$  is the lead of the diffracted wave in the  $k$  direction ( $k=1, 2, 3$ ).

The velocity field transfer function of the start. Operator  $|$  indicates the amplitude of the parameter. The superscript D indicates the parameter corresponding to the diffraction wave. The subscripts 1, 2, and 3 represent the components in the  $X$ ,  $Y$ , and  $Z$  directions, respectively.

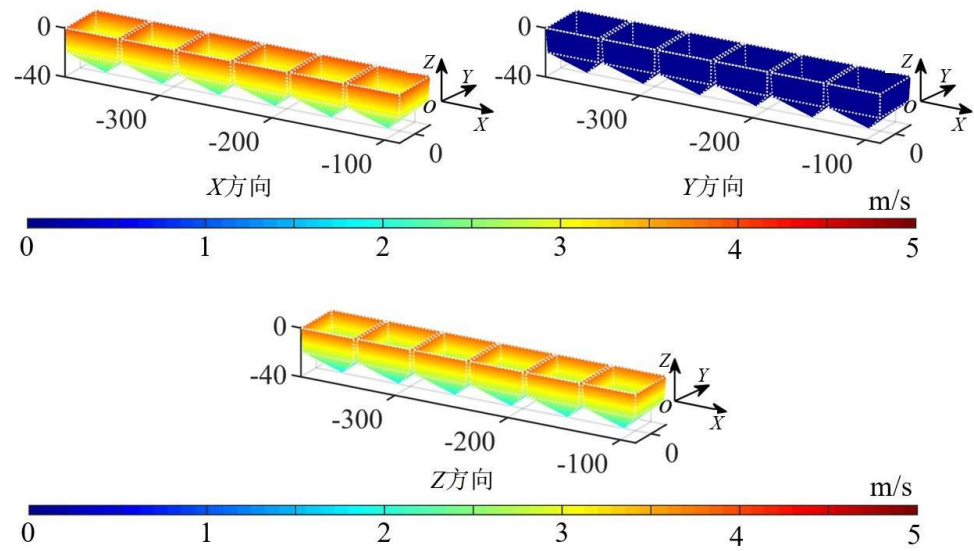
The water quality point velocity  $vR$  produced by the radiant wave can be expressed as:

$$vR = \left| \sum_{j=1}^6 vTF_j^R \sin(\omega_j t + \theta_{Rkj} + \eta_j) \right| - \left| \sum_{j=1}^6 vTF_j^R \sin(\omega_j t + \theta_{Rkj} + \eta_j) \right|_{without Fri} \quad (4-4)$$

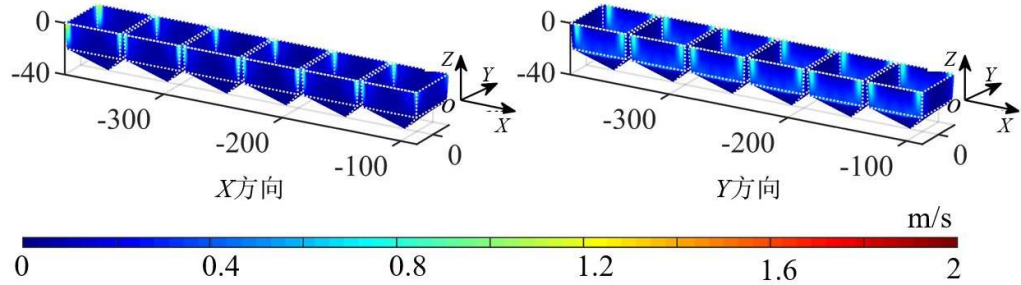
where,  $v_{R1}$ ,  $v_{R2}$  and  $v_{R3}$  And, With The component of the direction.  $Fri$  Separately  $v$  at  $X$ ,  $(k=1, 2, 3; j=1, 2, \dots, 6)$  is the velocity field transfer function in the  $k$  direction caused by the radiation wave generated by the movement of the buoy in the  $j$  direction.  $u_j$  and  $\eta_j$  are the  $j$  ( $j = 1, 2, \dots$ ) at the center of buoyancy of the body, respectively,  $6$  amplitude of motion and phase angle of 6 degrees of freedom. The superscript R represents the parameter corresponding to the radiant wave.  $\theta_{Rkj}$  ( $k=1, 2, 3; j=1, 2, \dots, 6$ ) Represents the phase angle of the velocity transfer function of the radiated wave in the  $k$  direction and the motion of the buoy in the  $j$  direction.

In this paper, the velocity transfer function of the water quality point at the location of the net structure is made using three-dimensional potential flow software

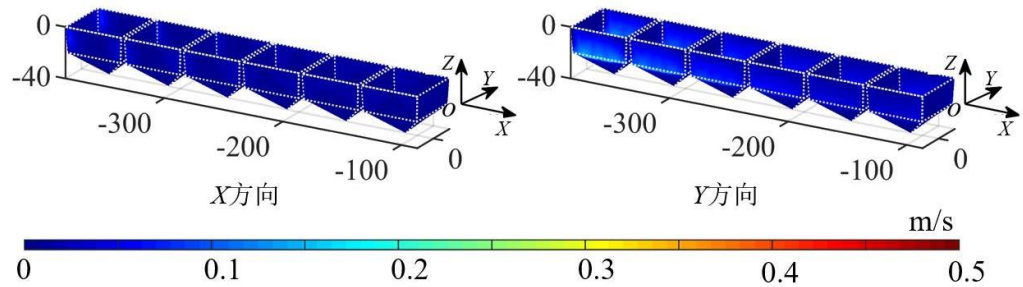
WAMIT is calculated by frequency domain analysis.



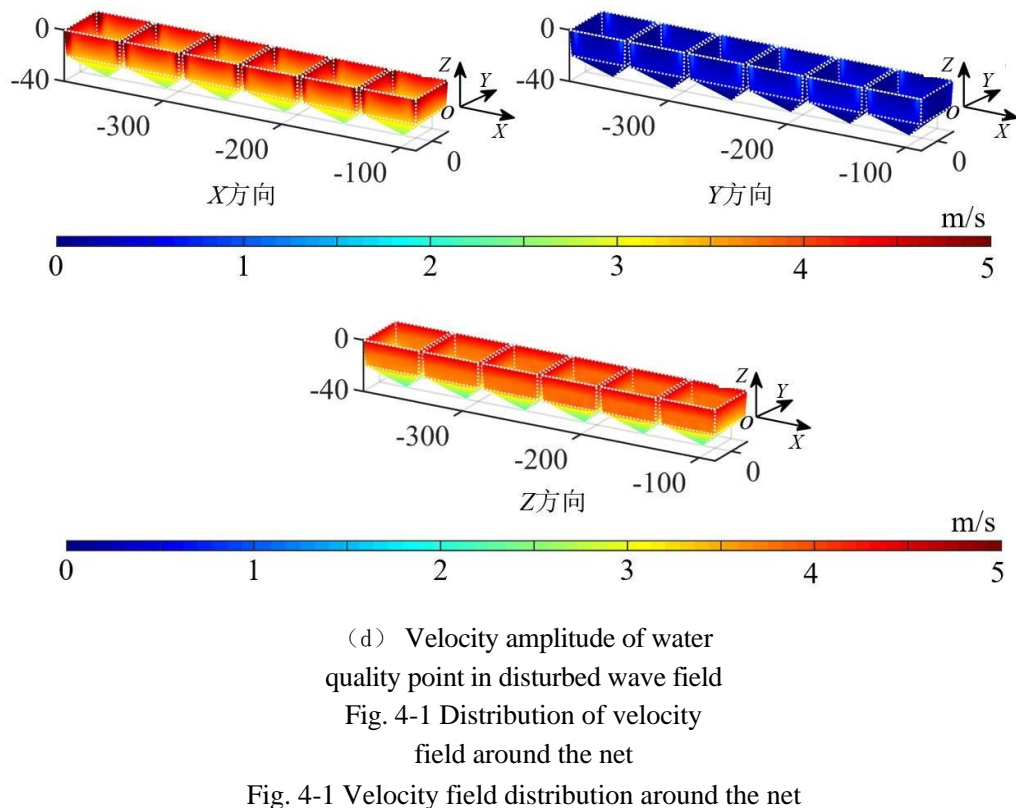
(a) The velocity amplitude of the incident wave water quality point



(b) The amplitude of the diffraction water quality point velocity



(c) Radiant wave water quality point velocity amplitude



(2) The distribution characteristics of water quality points in the disturbance wave field considering the influence of buoy disturbance under regular waves

According to the design wave method, the regular wave period and amplitude are selected, respectively 15.7 s and 9.6 m. fig 4-1 It's a perturbation

Under the wave field 6 The amplitude of the water quality point velocity of the wave field at the location of the breeding unit. composedFigure 4-1 It can be seen that the incident wave is in X Direction and With The velocity amplitudes of the water quality points in the direction are respectively 4.0 m/s and 3.9 m/s。, and in a perturbation wave field (incident wave + diffraction wave + radiated wave),X Direction and With The maximum water quality point velocity amplitude in the direction is reached 5.4 m/s和 4.6 m/s, which is increased when only the incident wave is taken into account 36%and 18%。 observefig 4-1 (b) and (c) fig 4-1 (a) and (d) The velocity amplitude of water quality points at different positions in the direction is equal. Since the wave propagation direction is 180 °, so in And The velocity of the water quality point in the direction is 0。 Taking into account the effects of diffraction and radiant waves, the amplitude of water quality point velocity increases significantly, especially And The increase in velocity in the direction is even more significant. The maximum water point velocity amplitude occurs near the corners of the flat-water aquaculture units, which, according to Morrison's formula, leads to an increase in the local tension of the net at these locations, which in turn affects the distribution of connector loads in the nearby area.

After obtaining the water quality point velocity of the disturbed wave field, the hydrodynamic load of the net is solved by Morrison's formula. As shown in Figure 4-2 , the hydrodynamic load per unit length of the mesh can be expressed as  $dF_N(t)$ :

$$dF(t) = C \frac{1}{N} \rho \delta \left[ \mathbf{U}_N(t) - \mathbf{one}(t) (\mathbf{U}_N(t) \cdot \mathbf{V}_N) \right] \quad (4-5)$$

$$\mathbf{V}_N = \dot{\mathbf{V}} + \mathbf{V} \cdot \boldsymbol{\varepsilon}$$

In the above equation,  $dN$  denotes the diameter of the equivalent model of the net       $\mathbf{vn}$  represents the water quality point velocity and acceleration perpendicular to the net

$\dot{\mathbf{u}}_n$  represents the velocity and acceleration of the movement of the steel frame element in the same direction as the net, and  $\mathbf{e}$  represents the unit vector in the same direction as the net  
 $CDN$  represents the hydrodynamic coefficient of the net.

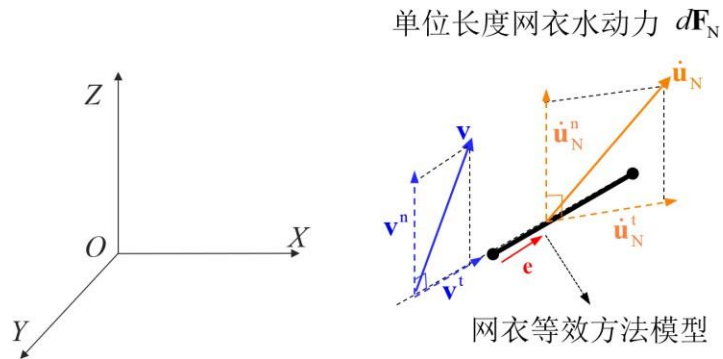


Figure 4-2 Hydrodynamics of netting under perturbation field  
Fig. 4-2 Hydrodynamic force on fish nets under disturbed wave field

#### 4.2.2 Dynamic response analysis of large cage considering the influence of disturbed wave field on net clothing under regular waves

In the dynamic analysis of large cages considering the influence of buoys on the hydrodynamics of the net coat under regular waves, the large cages are first separated into floating bodies and net coats according to the hydrodynamic characteristics of each part of the cage. For the large floating body of the cage, the hydrodynamic coefficient and wave excitation force of the floating body are solved in the frequency domain based on the three-dimensional potential flow theory, and the velocity field transfer function caused by the diffraction and radiation waves of the floating body at the position of the steel frame and the net coat is obtained. At the same time, based on the finite element method, the steel frame and the net coat were simulated by beam element and rod element respectively, and the Morrison formula was used to obtain the hydrodynamic load considering the influence of floating disturbance. Then, the floating body is regarded as a rigid body, and the motion of the node at the junction of the floating body and the mesh and steel frame is coupled, and the displacement and velocity of the node at the junction of the net coat and the steel frame are calculated from the motion of the float, so as to realize the motion coupling of the buoy, the steel frame and the net coat, and the overall motion equation of the cage considering the influence of diffraction wave and radiation wave in the disturbed wave field is established, and the overall motion response of the cage can be obtained by solving the equation in the time domain. Figure 4-3 shows the specific process of coupling analysis of large cages considering the influence of buoys on nets under regular waves.

In a coupled time-domain analysis under regular waves, the motion response equation for a

large cage can be expressed as:

$$\begin{aligned} (\mathbf{M} \square \mathbf{A}) \ddot{\mathbf{u}}(t) + \mathbf{X} \dot{\mathbf{v}}(t) + \mathbf{K} \mathbf{v}(t) &= \Phi \boldsymbol{\Omega}(t) + \mathbf{FCouple}(t) \\ \mathbf{FCouple}(t) &= \Phi \mathbf{H}(t) + \Phi \boldsymbol{\Gamma}(t) + \Phi \mathbf{B}(t) - \Phi \mathbf{I}(t) \end{aligned} \quad (4-6)$$

where  $\mathbf{FCouple}(t)$  represents the coupling load term generated by the net and the steel frame on the floating body,  $\mathbf{FH}(t)$ ,  $\mathbf{FG}(t)$ ,  $\mathbf{FB}(t)$  and  $\mathbf{FI}(t)$  represent the hydrodynamic loads of the mesh and steel frames, respectively, the expression of gravity, buoyancy, and inertial force load at the center of the buoyancy mass.

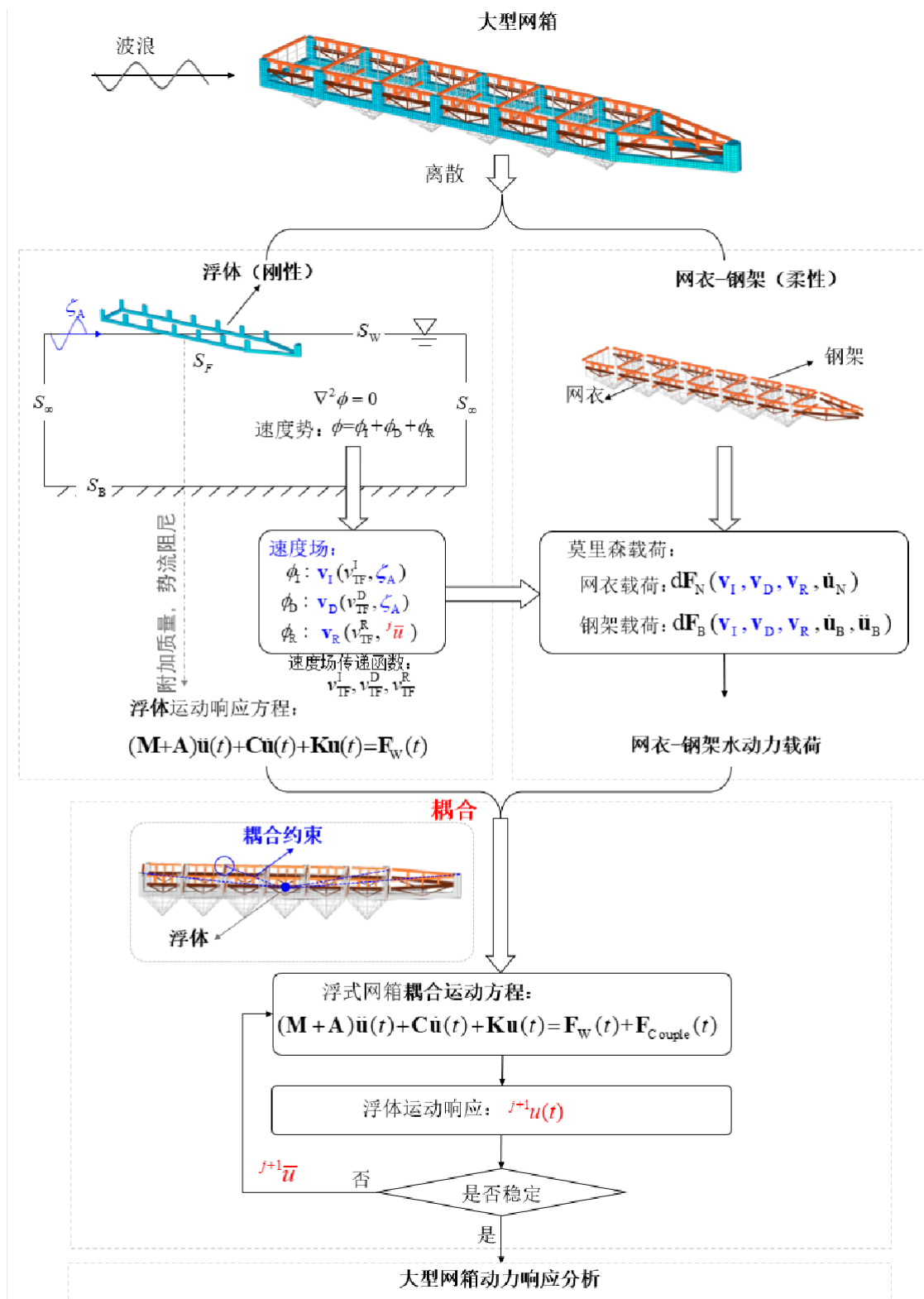


Figure4-3 Flow chart of coupling analysis of large cages under regular disturbance wave field

Fig. 4-3 Flowchart of large fish cage coupling analysis under disturbed regular wave

The floating body mass can be quickly obtained by performing a fast Fourier transform on the motion response time calendar  $u(t)$  at the floating center of gravity

Amplitude and phase angle of motion at the center:

$$(\bar{\mathbf{u}}, \delta_R) = \Phi \Phi T(\mathbf{v}(t)) \quad (4-7)$$

In the above equation, FFT stands for Fast Fourier Transform.

The disturbance of the buoy affects the hydrodynamic load of the net and steel frame by changing the water quality point velocity distribution of the wave field. Due to the float with a net coat-The steel frame system is coupled, which further affects the movement of the buoy. In the first cyclic calculation, the effect of the floating radiation wave is not considered, and only the action of the incident wave and the diffracted wave is considered in the velocity field, and then the integral coupled motion equation of the cage is solved in the time domain, and the time history of the floating centroid motion considering the load of the net and steel frame is obtained<sup>1u(t)</sup>, 1u is obtained by a fast Fourier transform and 1δ to determine the incident wave water point velocity of the wave field after the disturbance for the velocity field calculation of the next cycle. Contrast  $j+1$  sub-cyclical <sup>$j+1u$</sup> 、 <sup>$j+1\delta$</sup>  and the first  $j$  sub-cyclical <sup>$j$</sup>  in the  $\mathbf{D}$ , if in any degree of freedom

All are  $\|\mathbf{u}^j - \mathbf{u}^{j+1}\| \leq \epsilon$  (set in this article as  $\epsilon = 0.05$ ),  $\mathbf{u}^{j+1}$  satisfied

state, the disturbance wave field obtained at this time is the final result, and the iterative calculation is stopped, and then the dynamic response of the cage is analyzed. If it is not satisfied, the next study is calculated iteratively. It should be noted that each cycle calculation is a complete time cycle calculation, if the numerical simulation duration in each time domain is  $T$  and the number of iteration calculations is  $N$ , then a total of  $(N+1)$  calculations are required, and the total numerical simulation duration is  $(N+1)T$ .

### 4.3 Analysis of the influence of perturbation wave field on netting

In the web response analysis in this section, the net tension, the loss of culture volume in the culture unit, and the load transferred to the connector are analyzed, respectively.

#### 4.3.1 Netwear tension

As mentioned above, N11-N62 were selected separately in the mesh tension analysis 12 The net coating unit (or network cable unit) at each location is analyzed, as shown in the figure 3-15 show.fig 4-4 Different moments in the same regular wave period are given Tension distribution of unit Net 1. As can be seen from the figure, the tension of mesh 1 and mesh 3 is significantly higher than that of mesh 2

Mesh 4, which is mainly due to the fact that Mesh 1 and Mesh 3 are located in the waveside

direction. The maximum tension is generally found at the top of Mesh 1 and Mesh 3 in the horizontal wire perpendicular to the X direction, which is consistent with the results above. In addition, because the edge of the mesh is closer to the connector and is constrained by the connector, the cable tension at the edge of the mesh is significantly higher than the tension in the middle of the mesh.

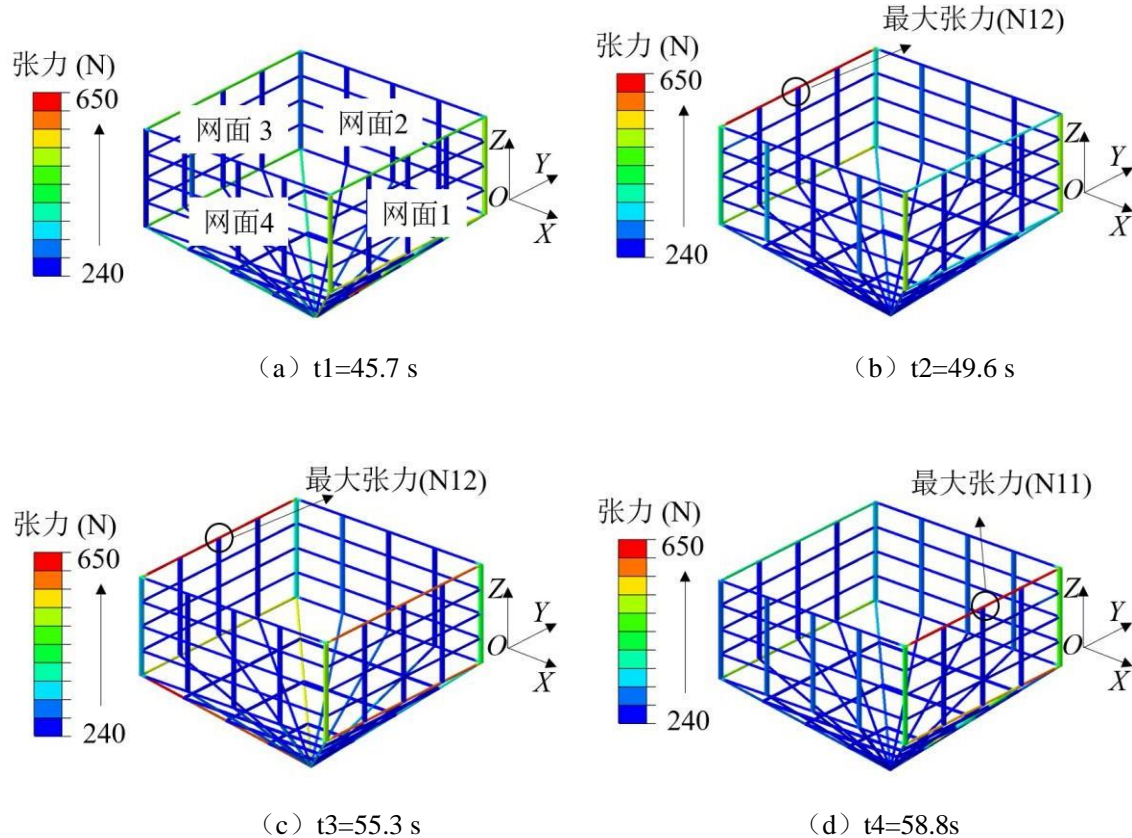


Figure 4-4 Diagram of the network cable tension of the breeding unit Net 1 at different times during the same wave period

Fig. 4-4 Contour of the tension in Net 1 at different time steps within one wave period

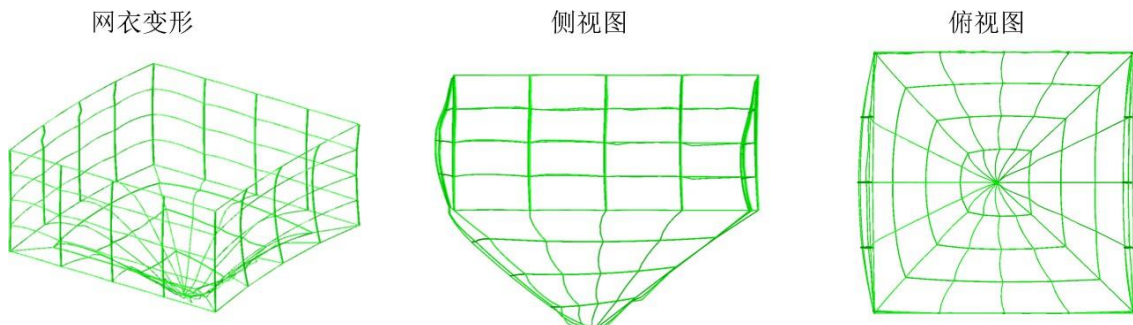


Figure 4-5 Deformation of netwear under a disturbed wave field

Fig. 4-5 The deformation of net under disturbed wave field

Figure 4-5 is a deformation diagram of the culture unit Net 1 under a disturbed wave field. As can be seen from the figure, the deformation amplitude of the side mesh is not obvious, which is mainly due to the limiting effect of the connector, and also shows that the connector has an obvious effect on ensuring the breeding volume of the net. Although the

deformation of the bottom mesh is relatively obvious, it is due to the hydrodynamic load on the bottom net

It is smaller, and there is a counterweight at the bottom, so the deformation is not noticeable.

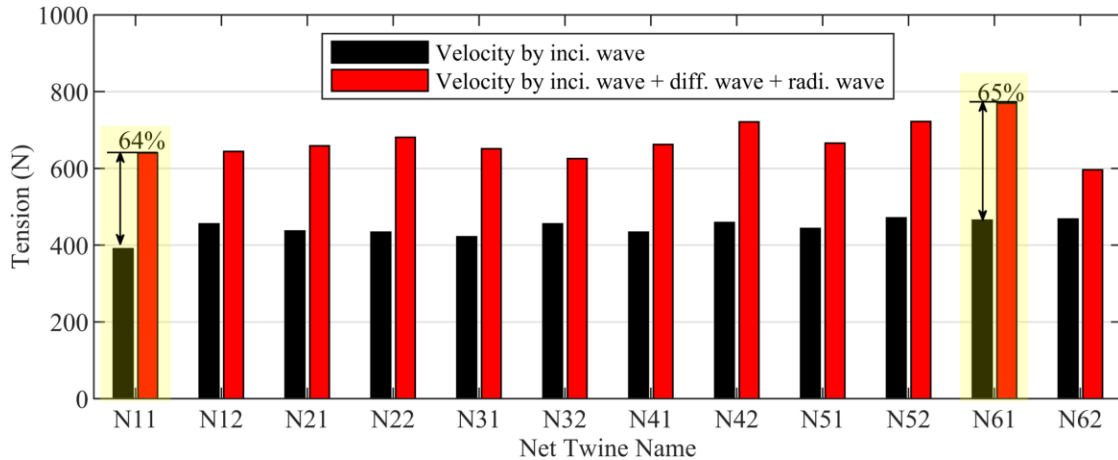


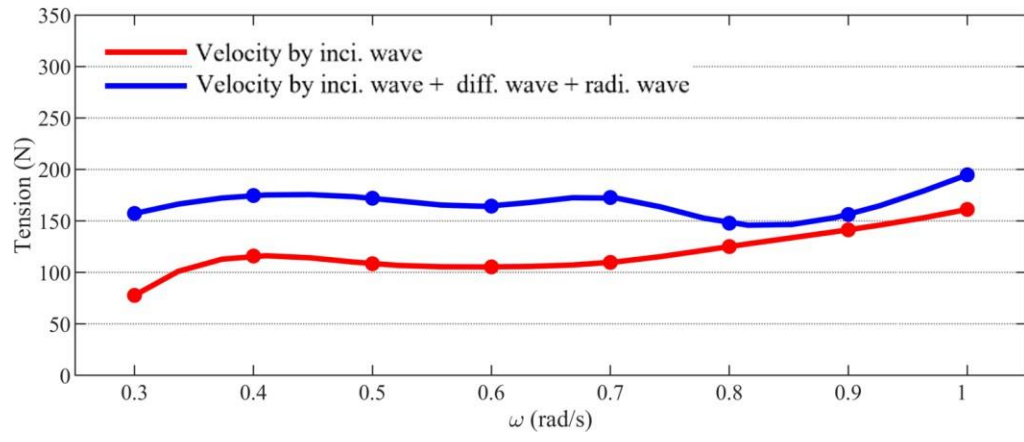
Figure 4-6 Maximum Cable Tension of the Selected Mesh Unit

Fig. 4-6 Maximum net tension at different selected net areas

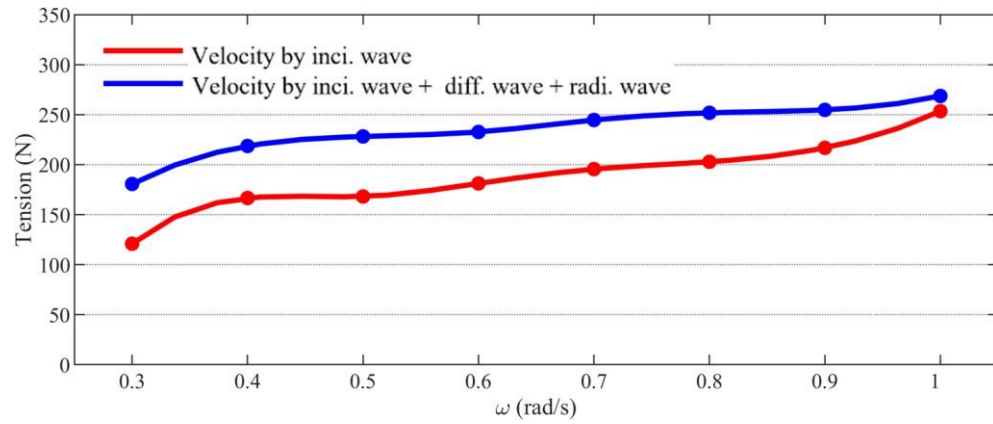
Figure 4-6 shows the maximum grid line tension distribution under the incident wave only and taking into account the disturbance wave field. At the 12 mesh units, the tension of the network cable taking into account the disturbed wave field increased by an average of 51%, with the largest increase of 65% and 64% for the N61 and N11 cables, respectively. The increase in the tension of the network cable is a good illustration of the increase in velocity at the point of maximum water quality in the velocity field. Relatively speaking, when only considering the action of the incident wave, the distribution of the network line tension at different positions is relatively uniform, which is due to the axial distribution of each breeding unit along the cage, and relative to the water quality point velocity, the movement speed of the cage is relatively small, and the net coat is limited by the connector, it is difficult to have obvious flexible deformation, resulting in similar boundary conditions of the breeding unit, resulting in little difference in the tension of the network cable at different positions. When the influence of diffraction and radiation waves is taken into account, although the boundary conditions of each farming unit remain similar, the dominant point velocity distribution of water quality has changed, which leads to the change of the network line tension distribution at different locations under the disturbance wave field.

Figure 4-7 shows the maximum tension of the network cable units N11 and N52 at different wave frequencies, and the wave amplitude is 4.75 m to ensure that the wave steepness is less than the breaking limit of the wave. When only the action of the incident wave is taken into account, the maximum tension of the network cable units N11 and N52 gradually increases with the increase of wave frequency, because the velocity of the water quality point near the still water surface increases with the increase of wave frequency. At the same time, when the influence of diffracted and radiated waves is taken into account, the tension of the network cable increases significantly at different frequencies. With the increase

of wave frequency, the increase of network cable tension will decrease to a certain extent, which is mainly due to the proportion of the increase in water quality point velocity caused by diffraction wave and radiated wave (defined in the text as  $\square = (\mathbf{vD} + \mathbf{vR})/\mathbf{vI}$ ) decreases as the wave frequency increases. For example, the increase in water point velocity in the X direction decreases from 37% at 0.3 rad/s to 28% at 0.8 rad/s.



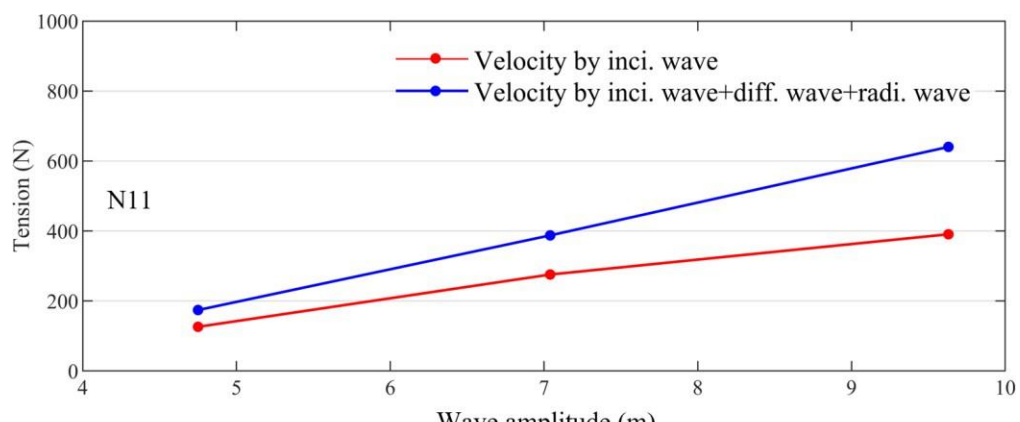
(a) Unit N11



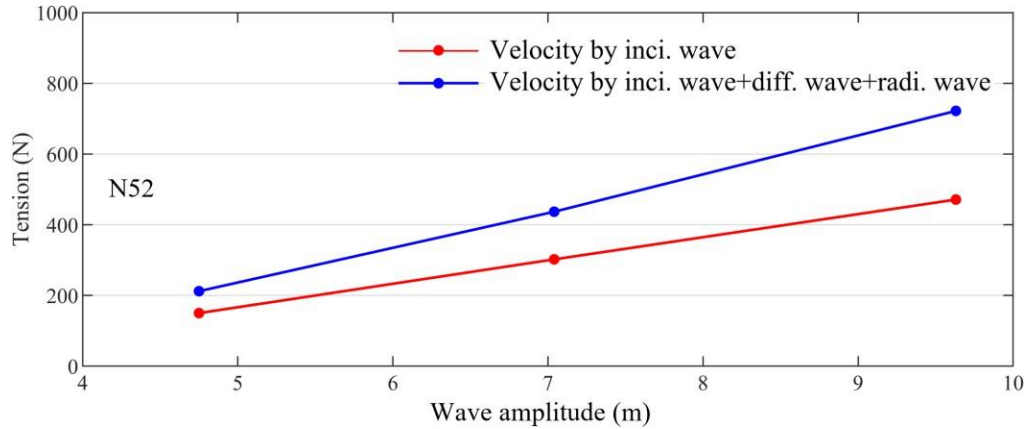
(b) Unit N52

Figure4-7 Maximum tension of the net at different wave frequencies

Fig. 4-7 Maximum net tension under different wave frequencies



(a) Unit N11



(b) Unit N52

Figure 4-8 Maximum tension of the net under different amplitudes

Fig. 4-8 Maximum twine tension under different wave amplitudes

Figure 4-8 shows the maximum tension of the cable elements N11 and N52 at different wave amplitudes. With the increase of wave amplitude, the maximum tension of the network cable increases rapidly, and the influence of diffracted wave and radiated wave is more significant. When the diffracted wave and radiated wave generated by the floating body are taken into account, the tension amplitude of the network cable unit N11~N52 increases by 12%, 21% and 23% respectively under the three wave amplitudes.

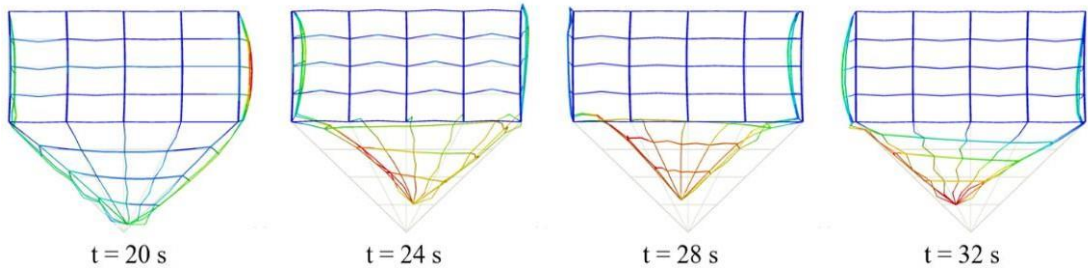
### 4.3.2 Loss of volume

Under the action of waves, the flexible net coat is easily deformed, resulting in a decrease in the breeding volume of the breeding unit to a certain extent, and this part of the lost breeding volume is called volume loss<sup>[117]</sup>。 In the previous study, the research object of breeding volume loss is mainly gravity cage, and there is very little research on large cages, on the one hand, because large cages are new structures, and related studies are not perfect, on the other hand, because large cages are arranged with a large number of connectors, which can reduce volume loss to a certain extent. However, from the perspective of optimal connector arrangement, it is still necessary to study the loss of breeding volume in large cages. Figures 4-9 show the amplitude of the wave at 8 m

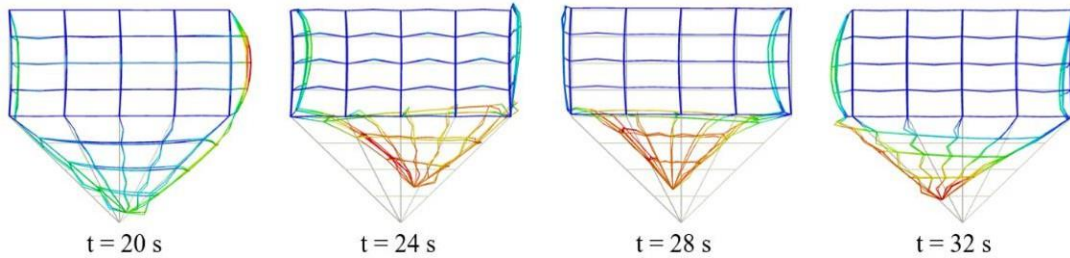
Deformation diagram of culture unit Net 1 with a wave period of 15.7 s. As can be seen from the figure, regardless of whether the influence of diffraction and radiation waves is taken into account, the breeding volume enclosed by the side net will not change significantly, while the bottom net will be greatly deformed. This is due to the fact that the connector is arranged at the edge of the side net, which effectively limits the flexible deformation of the net under the wave and reduces the volume loss, while the bottom net is only provided by 5

---

tons of weight, which is difficult to maintain the breeding volume of the bottom net.



(a) Only the incident wave action is considered



(b) Considering the combined effects of incident waves, diffracted waves, and radiated waves

Figure 4-9 Net 1 net deformation contour of culture unit

(side view).

Fig. 4-9 The contour of net deformation of Net 1 (side view)

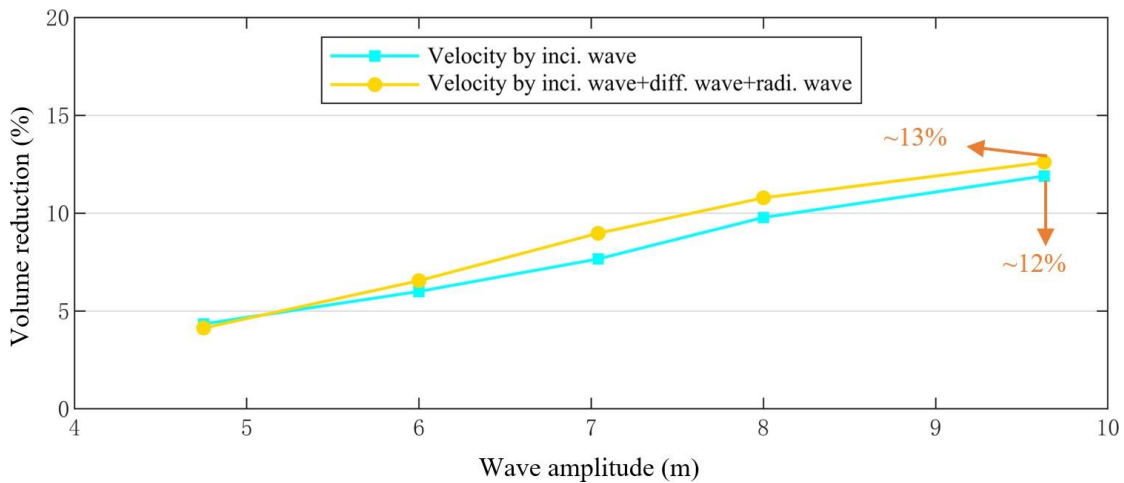


Figure 4-10 Volume loss rate at different amplitudes

Fig. 4-10 The volume reduction ratio under different wave amplitude

In order to further analyze the effects of diffraction and radiation waves on the culture volume of cages, fig 4-10 Breeding units at different amplitudes are given Net 1 maximum volume loss rate. The volume loss rate refers to the ratio of the breeding volume after the

deformation of the breeding unit to the breeding volume before the deformation. As can be seen from the figure, with the increase of volatility, the volume loss rate also increases gradually, but it is at a low level on the whole. When considering the effects of diffracted and radiated waves, the maximum volume loss rate is determined by 12%Left and right increase to approx 13%, the change is very small. This is due to the fact that the culture volume enclosed by the side nets is exceeded 4 10,000 cubic meters, accounting for the whole thing

The proportion of the volume of each unit is as high as 75%, while the volume loss of the side nets is not significant due to the limitation of the connectors, so the maximum volume loss rate changes very little.

#### 4.3.3 Connector load

Due to the uniform distribution of the connectors of different breeding units, the bearing analysis of 10 connectors on the same side of the breeding unit Net 1 was carried out. The selected 10 connectors are divided into edge connectors C1~C4 and middle connectors E1~E6, as shown in Figure 3-17.

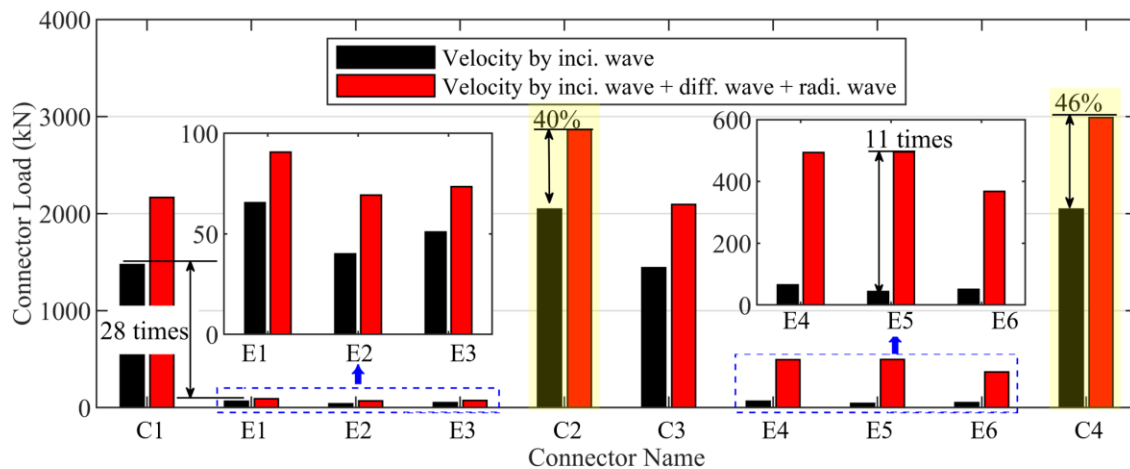


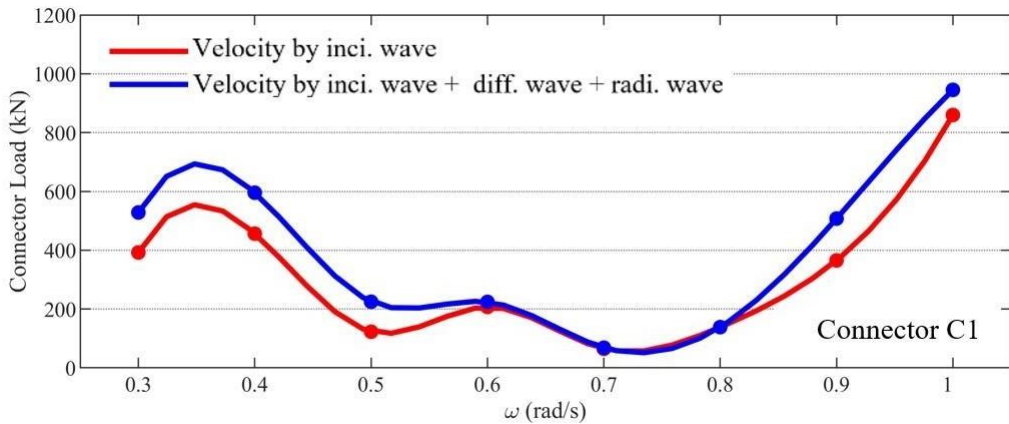
Figure 4-11 Connector Maximum Load  
Fig. 4-11 Maximum load on the connectors

Figure 4-11 shows the load amplitude of different connectors under regular waves, with a wave amplitude of 9.6 m and a wave period of 15.7 s. The load of the edge connector (C1~C4) is much larger than that of the middle connector (E1~E6), which is consistent with the analysis results in the previous article. When only the action of the incident wave is taken into account, the connector C1 carries 28 times more load than C2. When the effects of diffracted and radiated waves are taken into account, there is little difference in the load bearing increase of the edge connector (between 40%~46%). In addition, the bearing capacity of the middle connector of the lower layer will also increase to a certain extent, especially the bearing capacity of connector E5 has increased from the previous 44 kN to 495 kN, an increase of more than 11 times.

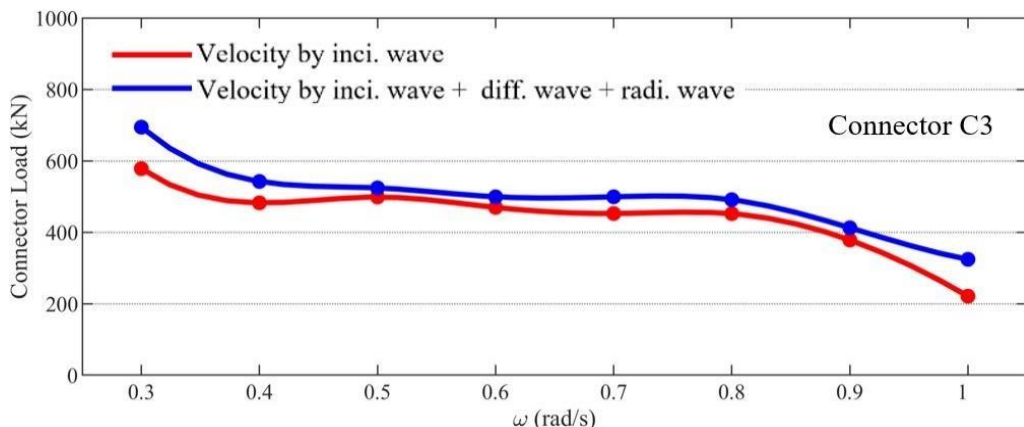
Figure 4-12 shows the loads of connectors C1 and C3 at different wave frequencies. As the wave frequency increases, the velocity of the water quality point near the still water surface increases significantly. However, at high frequencies, the attenuation of the water point velocity along the water depth direction is also more rapid, which leads to a "decrease-then

"increase" trend in the bearing capacity of connector C1 as the wave frequency increases. The diffracted and radiated waves have no obvious effect on the bearing of connector C1 in the range of 0.5 rad/s~0.8 rad/s. The reason for this phenomenon is that diffracted and radiated waves only have an effect on the local flow field area close to the position of the buoy, and have a limited effect on the flow field as a whole. Therefore, even if the diffraction wave and the radiated wave greatly increase the tension of the network cable at some local locations, the overall force of the network system will not change significantly

Change. The bearing of connector C3 is mainly caused by the hydrodynamic force of the bottom mesh and the side mesh perpendicular to the wave direction, which gradually decreases with the increase of wave frequency. This is mainly due to the fact that the position of connector C3 is deep from the water surface, and the water quality point velocity decreases exponentially with the water depth, so the bearing capacity of connector C3 decreases significantly. In addition, the diffracted and radiated waves have a similar effect on the bearing of connector C3 and connector C1.



(a) Bearing of connector C1



(b) Bearing of connector C3

Figure4-12 Maximum load of connectors at different wave frequencies

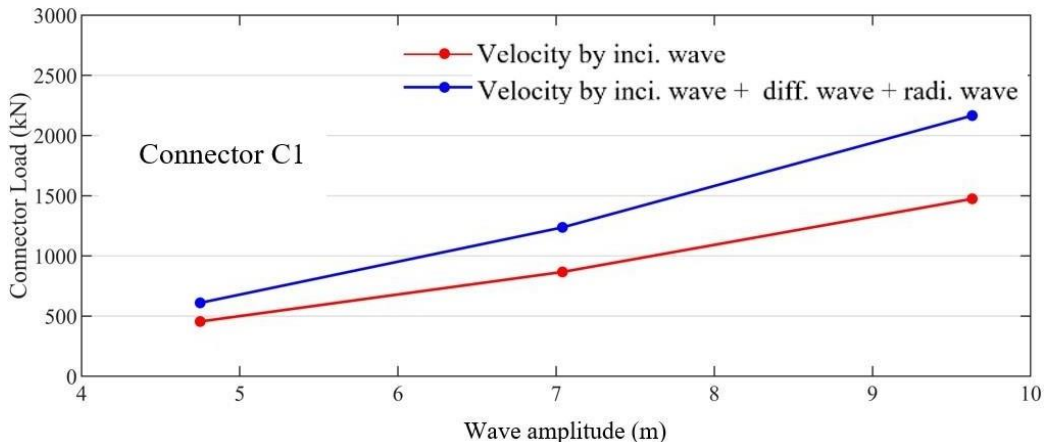
Fig. 4-12 Maximum connector load under different wave frequencies

Figure 4-13 shows the connectors C1 and C3 carrying at different amplitudes. As the amplitude of the wave increases, so does the bearing capacity of the connector. The effects of diffracted and radiated waves on the bearing capacity of the connector are similar to those on the tension of the net, and the increase of connector C1 is 32%, 37% and 45% respectively at the 3 wave amplitudes. The increases in C3 were 12%, 21% and 23%, respectively.

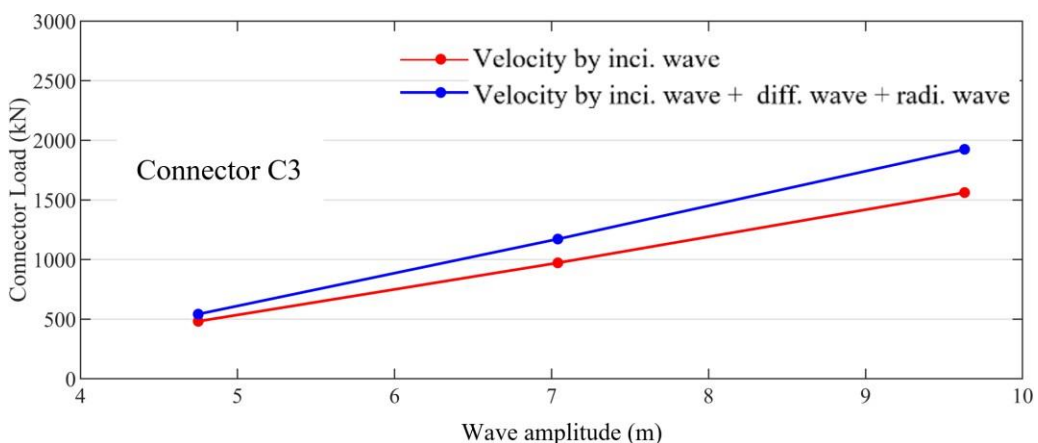
Figure 4-14 shows the increase in connector load due to diffracted and radiated waves at different amplitudes. With the increase of the amplitude, the overall bearing increase of the

---

connector also increases, which shows that the diffraction wave and the radiated wave have more obvious influence on the connector bearing under the large amplitude.



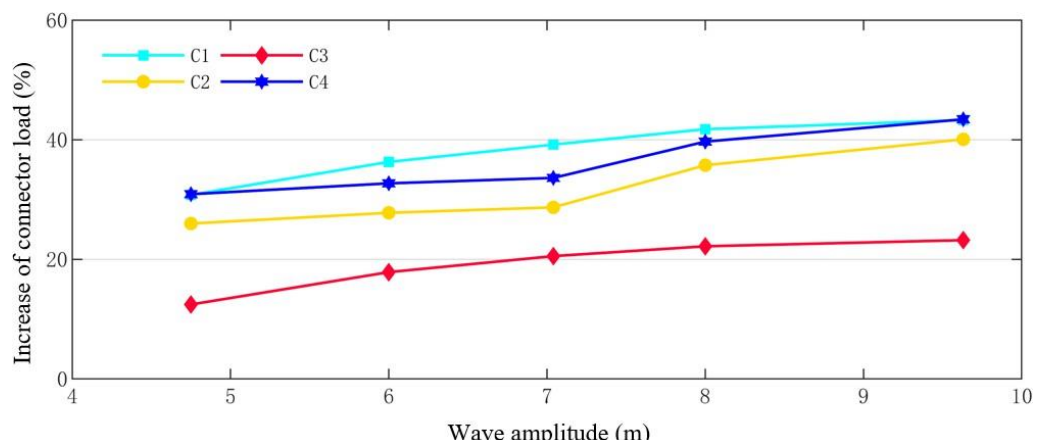
(a) Bearing of connector C1



(b) Bearing of connector C3

Figure4-13 Connector bearer at different wave amplitudes

Fig. 4-13 Maximum connector load under different wave amplitudes



(a) The load of connectors C1~C4

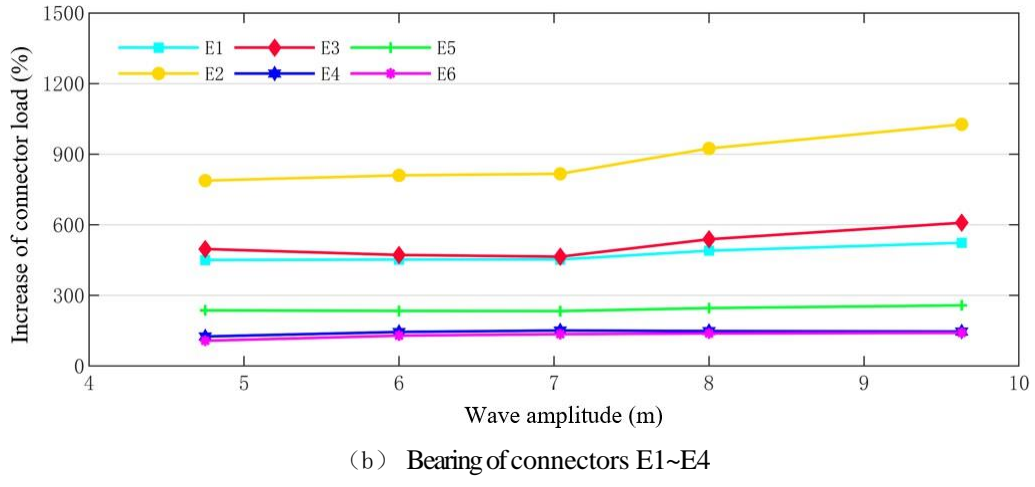


Figure 4-14 Connector load increase at different amplitudes

Fig. 4-14 Increase of the connector load under different wave amplitudes

## 4.4 Cross-sectional load characteristics of large cages considering the influence of perturbation wave field on net clothing

In this section, the cross-sectional load of the main steel structure is solved by a quasi-static method, and 7 steel cross-sections are selected

For analysis, the distribution of the cross-sections is shown in Figure 3-19 above.

### 4.4.1 Section bending moment

This subsection analyzes the vertical moments of the different cross-sections, and the selected cross-sections are shown above S1~S7. fig 4-15 It is the maximum cross-sectional vertical bending moment of the main steel structure under different sections.

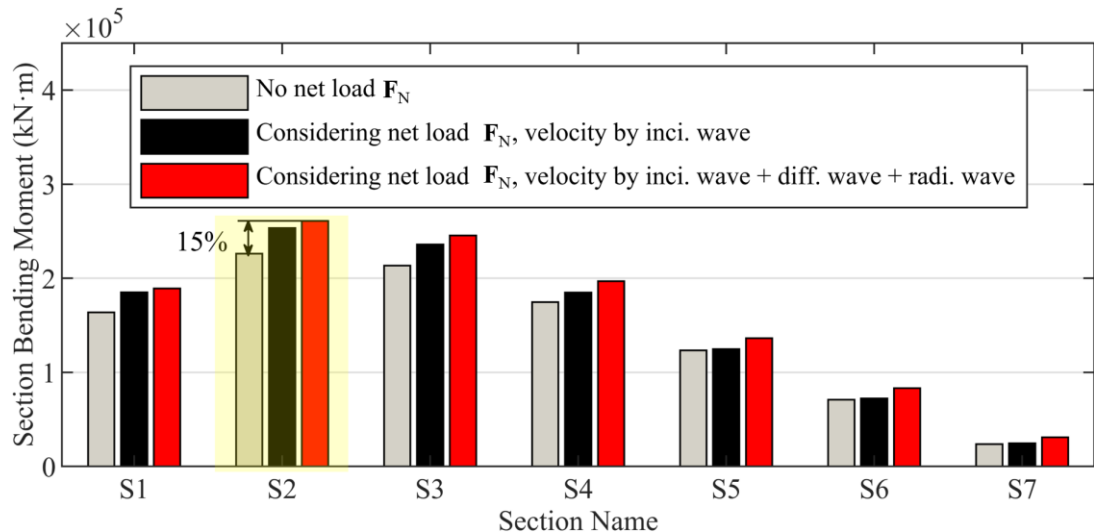


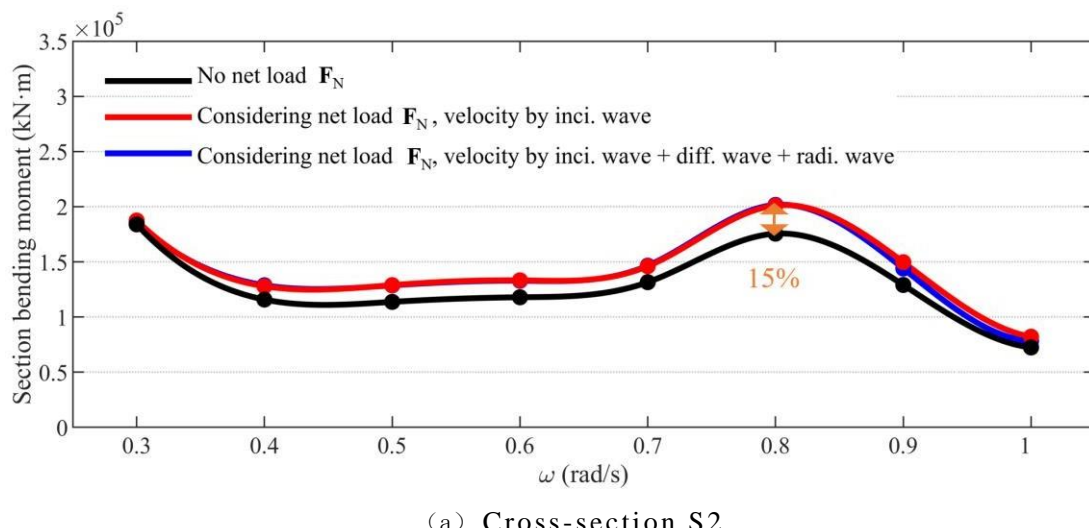
Figure 4-15 The maximum cross-sectional vertical bending moment of the main steel structure under

---

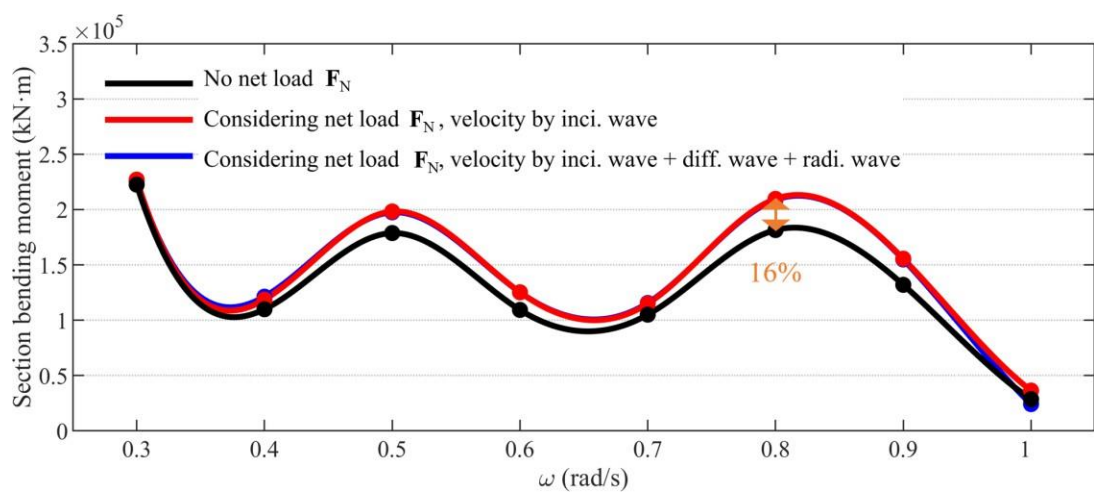
different cross-sections

Fig. 4-15 Maximum vertical bending moment of the main steel structure at different cross-sections

atfig 4-15 Under the three calculation models shown in (the model without netting, the model that only takes into account the action of the incident wave, and the model that takes into account the disturbance of the floating body), the maximum vertical bending moment of the cross-section occurs in the cross-section S2 Nearby, the cross-section is located on the side of the amidship near the bow of the cage, while the maximum bending moment of the traditional hull structure generally occurs near the amidships, and the reason for this difference may be that the large cage is a non-closed structure, resulting in the maximum vertical bending moment moving forward to the bow. Regardless of whether the effects of diffracted and radiated waves are taken into account, the cross-section moment increases to a certain extent when considering the hydrodynamic load of the net, as in the cross-section S2 , the vertical moment of the section appears 15% amplification. The cross-sectional bending moments considering the influence of diffraction and radiated waves are consistent with the results of only considering the incident waves, and the overall difference is not large, which indicates that the influence of the disturbance of the floating body on the wave field on the vertical bending moment of the cross-section of the main steel structure is limited.



(a) Cross-section S2



## (b) Cross-section S3

Figure4-16 Maximum vertical bending moment at different cross-sections at different wave frequencies  
Fig. 4-16 Maximum vertical bending moment of the main steel structure for different wave frequencies  
at different cross sections

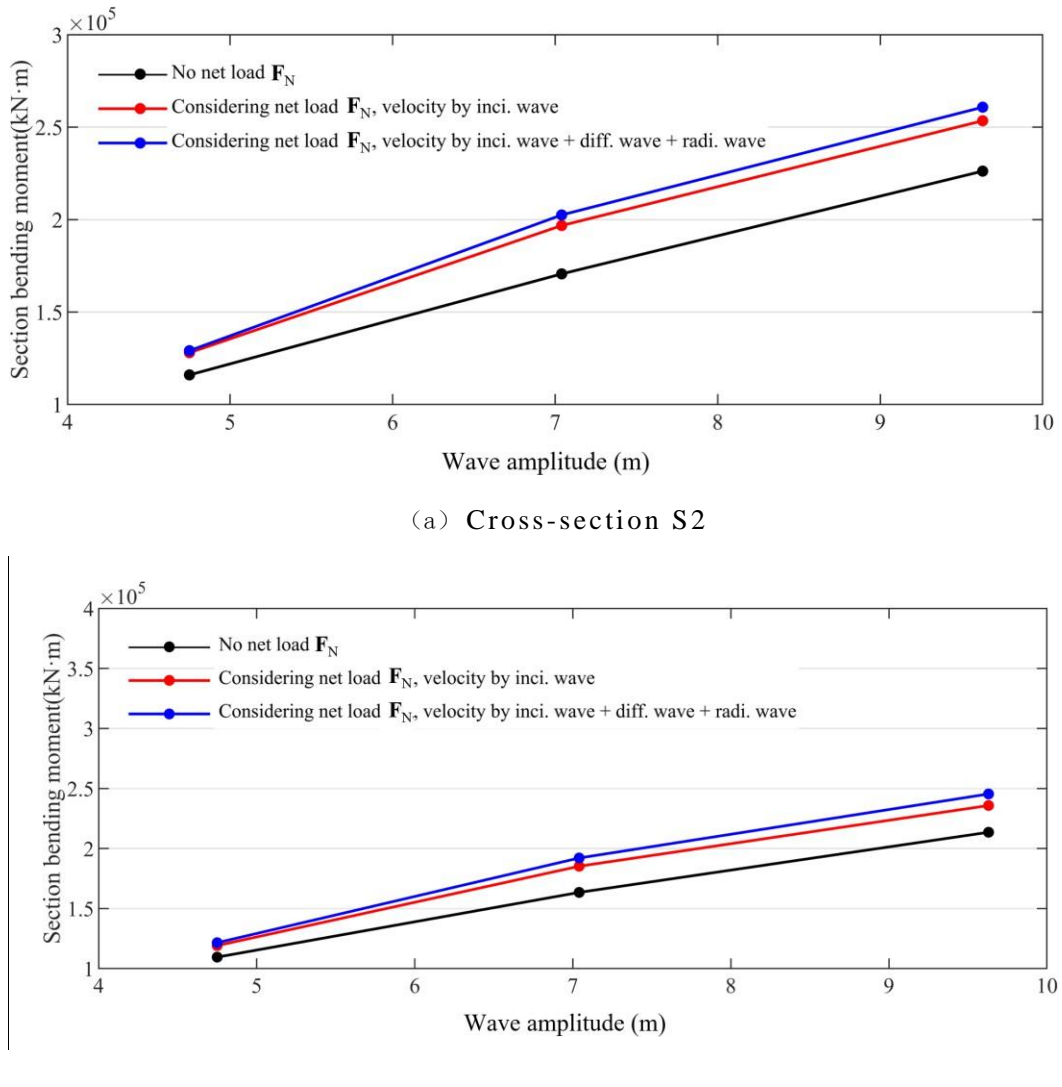


Figure 4-17 Maximum vertical bending moment at different cross-sections under the amplitude of the pass-through wave

Fig. 4-17 Maximum vertical bending moment of the main steel structure for different wave amplitudes at different cross sections

Figure 4-16 shows the maximum vertical bending moment at section S2 at different wave frequencies. Because the hydrodynamic load that float body and steel frame structure itself are subjected to is much greater than the net load that is transmitted to the main body steel structure by connector, therefore, when considering the net load, the change of cross-section vertical bending moment is not obvious. In addition, when the influence of diffracted and radiated waves is taken into account, the change in cross-sectional moment is not significant. Figure 4-17 Maximum vertical moment at cross-section S2 and cross-section S3 under the unpass amplitude. When the net load is taken into account, the maximum increase in cross-section moment is 19%. However, the change of cross-section moment is still not obvious under different amplitudes.

#### 4.4.2 Cross-section shear force

This subsection analyzes the vertical shear force of the cross-section, and the selected cross-section is S1~S7 as shown above (as shown in Fig

3-19 ).

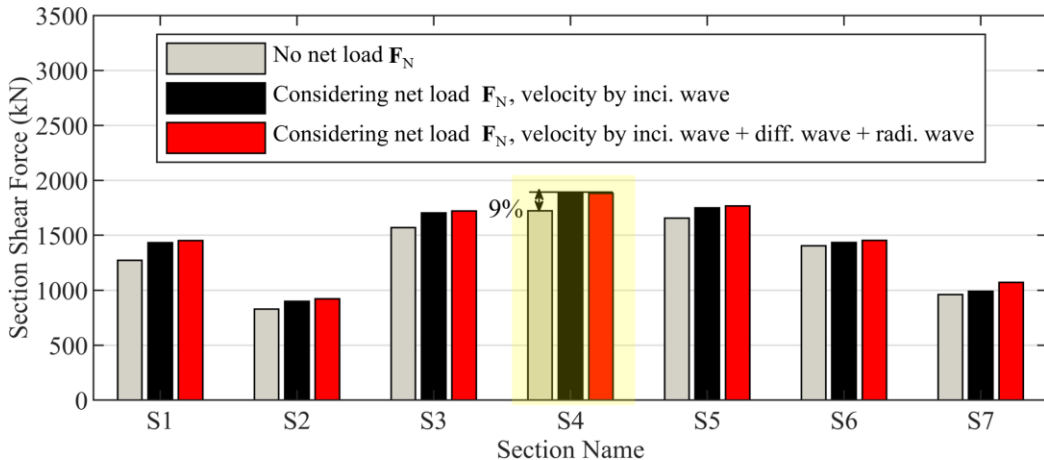
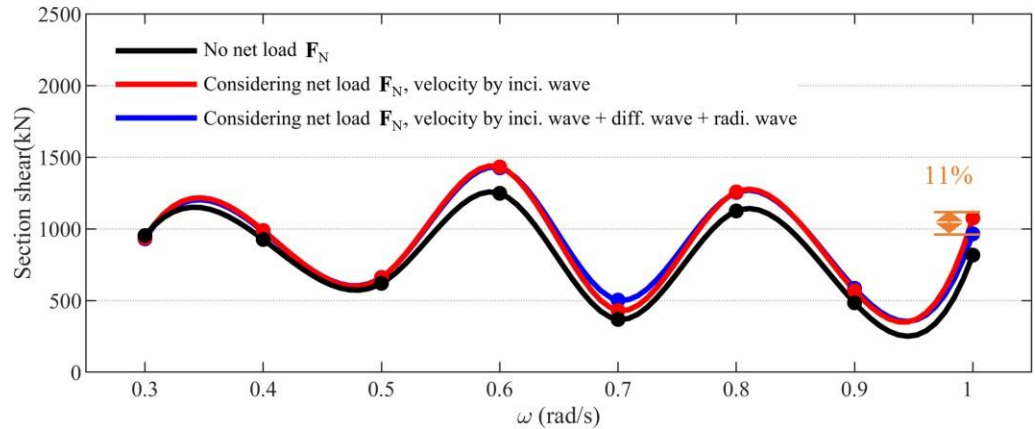


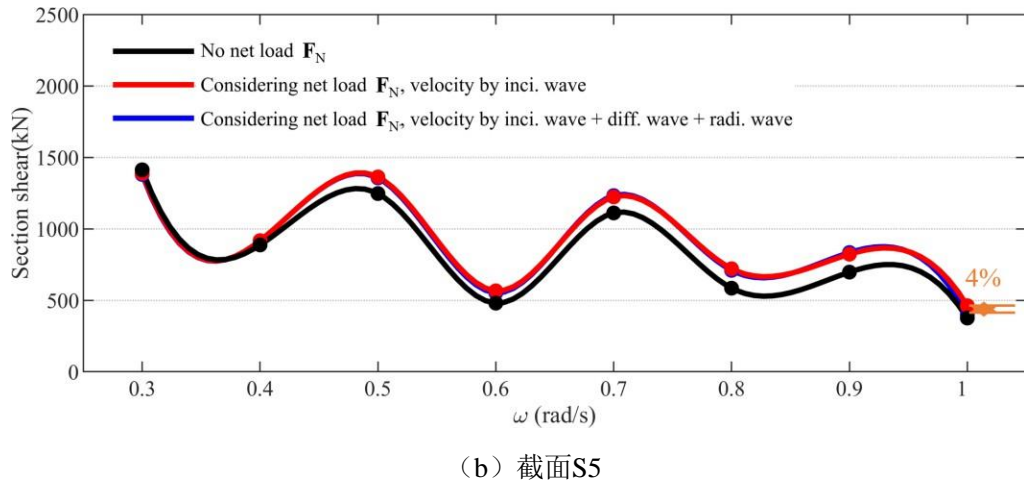
Figure4-18 The maximum cross-sectional vertical shear force of the main steel structure under different cross-sections

Fig. 4-18 Maximum vertical shear force of the main steel structure at different cross-sections

fig4-18 It is the maximum cross-sectional vertical shear force of the main steel structure under different cross-sections. In the three calculation models shown, the maximum vertical shear force of the cross-section is located at the cross-section S4. Nearby, this is close to the cage amidships, which is consistent with the location of the maximum bending moment of the conventional hull structure, but the cross-sectional shear force from the bow to the stern section is generally "reduced first".-After enlargement-The reason for this difference may be the same as the reason for the vertical moment trend of the maximum cross-section, which is due to the special structural form of the large cage. Regardless of whether the effects of diffracted and radiated waves are taken into account, the vertical shear force of each cross-section increases to a certain extent when considering the hydrodynamic load of the net, as in the cross-section S4 , the vertical shear force of the section appears 9% amplification. Considering the influence of diffraction wave and radiant wave, the variation trend of the cross-section shear force along the axial direction of the cage is not changed, and the influence degree is also small, which indicates that the influence of the disturbance of the floating body on the wave field on the cross-section vertical shear force of the main steel structure is not significant.



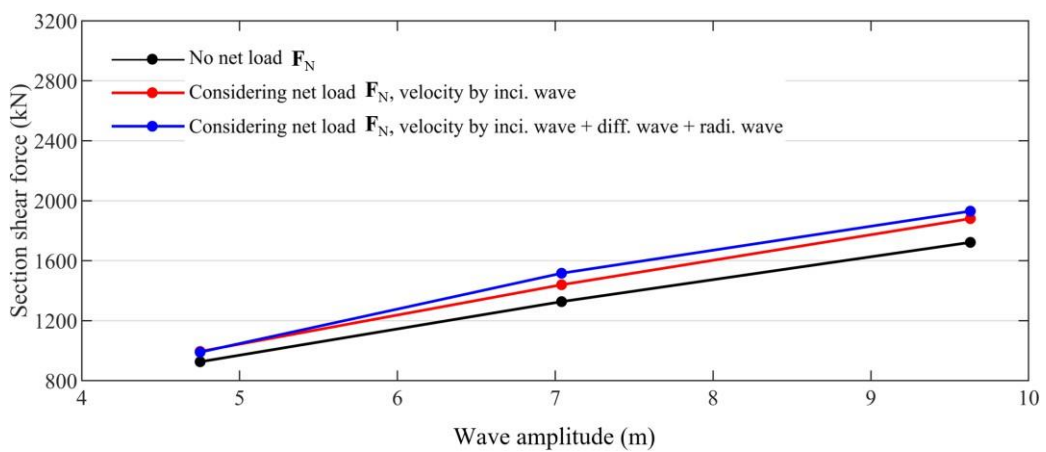
(a) 截面 S4



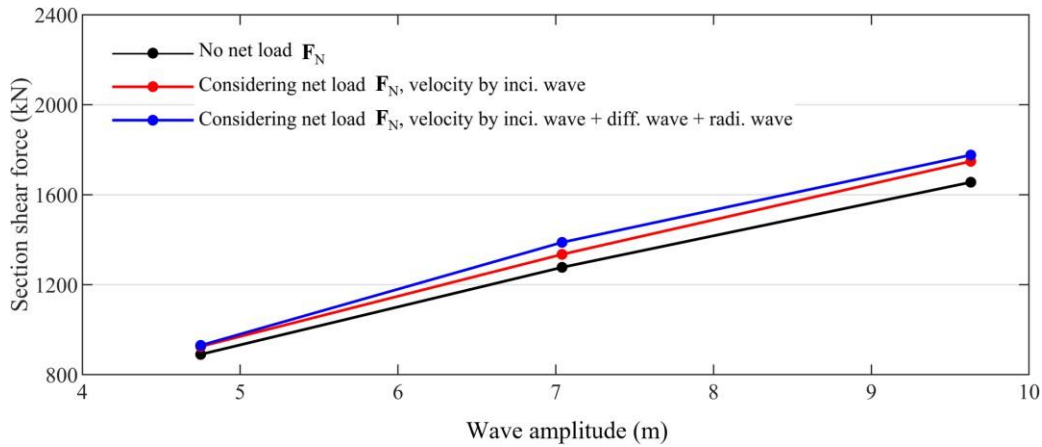
(b) 截面S5

Figure 4-19 Maximum vertical shear force at different cross-sections at different wave frequencies  
Fig. 4-19 Maximum vertical shear force of the main steel structure for different wave frequencies at different cross section

fig 4-19 It is a cross-section at different wave frequencies S4 and cross-sections S5 The maximum vertical shear force at . As can be seen from the figure, the vertical shear force of the cross-section increases to a certain extent when the mesh load is considered, but the overall change is not obvious. When the disturbance of the buoys to the wave field is taken into account, the change in cross-sectional moment is not significant. Figure 4 - 20 It is not through the amplitude of the lower cross-section S4 and the cross-section S5 The maximum vertical shear force at . When the net load is taken into account and the influence of diffraction wave and radiant wave is considered, the cross-sectional shear force value is the largest, and when the hydrodynamic load of the net is not considered, the cross-sectional shear force is the smallest, and the maximum difference increase is reached 13%。 On the whole, the presence of hydrodynamic load in the net coat will change the shear force and vertical bending moment of the cross-section under different amplitudes, but the influence is limited.



(a) Cross-section S4



(b) Cross-section S5

Figure 4-20 Maximum vertical shear force at different cross-sections at different wave amplitudes

Fig. 4-20 Maximum vertical shear force of the main steel structure for different wave amplitudes at different cross sections

## 4.5 Summary of this chapter

In this chapter, a dynamic analysis method of large-scale cages considering the influence of disturbed wave fields on nets under regular waves is established. Firstly, the three-dimensional potential flow theory is used to obtain the hydrodynamic load of the rigid floating body under the action of regular waves, and the velocity field of the floating body disturbance acting on the net under the regular wave is reconstructed. The hydrodynamic force of the mesh coating under the action of the disturbance wave field is balanced with the motion response of the floating body through the iterative method, and then the coupled motion equation of the large cage is solved to obtain the influence of the wave field after the disturbance of the floating body on the tension of the network cable, the loss of breeding volume and the bearing of the connector. Based on the quasi-static method, the cross-sectional strength check of the main steel structure considering the load of the net coating was carried out. Finally, the effect of wave frequency on the structural strength of large cages was studied. The main conclusions are as follows:

(1) Considering the diffraction wave and radiation wave generated by the disturbance of the floating body, the velocity field around the mesh coat will increase significantly, especially at the corner position of the edge of the net. Among the diffracted and radiated waves caused by the floating body, the diffracted wave dominates in the increase in the velocity generated. For the large cages in this paper, the variation area of the water quality point velocity in the wave field is concentrated at the corner of the mesh near the still water surface.

(2) Under the action of waves, the disturbance of the floating body will lead to a significant increase in the tension of the network cable, and the average increase of the network cable tension at different positions is about a significant one, and the average increase of the

network cable tension at different positions under extreme sea conditions reaches 51%, and the maximum increase even reaches 65%, so the impact of the disturbance of the floating body should be considered in the safety check of the net structure.

(3) For the loss of breeding volume of net clothing, due to the obvious limiting effect of the connector on the deformation of the side net, the overall loss rate of breeding volume is low, and the maximum loss rate under the working conditions in this paper is only 13%, and the impact of diffraction wave and radiation wave on breeding volume is very small, from the perspective of improving calculation efficiency, the impact of floating disturbance can be ignored in the analysis of breeding volume loss.

(4) Regardless of the effects of diffracted and radiated waves, the edge connector carries much more than the middle connector

bearing, the difference is close to thirty times. When taking into account the perturbation of the buoys to the regular wave field, the increase in the bearing capacity of the connectors at different edges is similar, and the perturbation of the buoys results in an approximately 11-fold increase in the bearing capacity of the connector E5.

(5) Under the action of waves, considering the load of the net coat will lead to the increase of the vertical bending moment and shear force of the main steel structure section to a certain extent, but the increase is not significant. At the same time, it is not obvious whether the floating disturbance is considered in the calculation of net clothing load.

(6) With the increase of wave frequency, the network cable tension and connector bearing gradually increase when considering the buoyancy disturbance, and the edge connector bearing shows a "W-shaped" trend with the increase of wave frequency. Overall, the mesh load leads to an increase in the vertical bending moment and shear force of the section at different wave frequencies. When considering the mesh load, considering the effect of the buoyancy disturbance may also lead to a reduction in the shear force of the individual sections.

## Chapter 5 Dynamic response analysis of large cages considering the influence of disturbance wave field on net clothing under irregular waves

### 5.1 introduction

According to the analysis in Chapter 4, it can be seen that the influence of large floating bodies on the hydrodynamics of the net coat cannot be ignored

The ring, in turn, will affect the movement of the floating body, and further affect the cross-sectional load of the main steel structure. According to the coupling analysis method of large cages considering the influence of buoy disturbance under regular waves in Chapter 4, this chapter proposes a dynamic response analysis method for large cages that is suitable for considering the coupling effect of rigid motion-disturbance wave field and hydrodynamic force of buoys under irregular waves. The statistical results of the response of large cages considering the influence of disturbance wave field on the hydrodynamics of net coats under the action of irregular waves were analyzed.

### 5.2 A dynamic analysis method of large cage considering the influence of floating disturbance on net clothing under irregular waves

#### 5.2.1 Solve the disturbance wave field considering the influence of floating body disturbance under irregular waves

- (1) A method for solving the disturbance wave field considering the influence of floating body disturbance under irregular waves

Since waves in the ocean are actually extremely irregular, it is necessary to use irregular waves to describe waves in the actual marine environment. In wave theory, irregular waves are composed of multiple linear regular waves with different circular frequencies, different amplitudes, and different phase angles, and the components of each regular wave can be determined according to the wave spectrum, and the phase angle is set randomly. When the influence of the diffracted and radiated waves of the buoy on the wave field is taken into account, the point velocity  $v_{irr}$  of the water quality under irregular waves can be obtained by superimposing the incident wave components, the diffraction wave components and the radiant wave components.

$$\mathbf{v}^{\text{mad}} = \mathbf{v}^{\text{mad}} + \mathbf{v}^{\text{mad}} + \mathbf{v}^{\text{mad}} \times [v_{And} \ v_{Wih}]^T \quad (5-1)$$

where  $\mathbf{virr}$ ,  $\mathbf{virr}$ , and  $\mathbf{virr}$  are represented as incident waves, diffracted waves, and radiant

---

waves, respectively, in an irregular wave field

The resulting water point velocity vectors,  $v_x$ ,  $v_y$ , and  $v_z$  represent the velocity of the water point velocity in the X, Y, and Z directions, respectively

Measure  
components  
ts.

Among them, the water quality point velocity  $v_I$  produced by the irregular incident wave can be expressed as:

$$\begin{aligned}
 & \text{Hymn} = \sum_{l=1}^N \left| v \right| \sum_{k=1}^{I-l} \left| vTF_1 \right| \left| \text{without}(\omega \lambda t + \theta I_1 + \square l) \right| \\
 & \quad + \sum_{l=1}^N \left| v \right| \sum_{k=1}^{I-l} \left| vTF_2 \right| \left| \text{without}(\omega \lambda t + \square l) \right| \\
 & \quad + \sum_{l=1}^N \left| v \right| \sum_{k=1}^{I-l} \left| vTF_3 \right| \left| \text{without}(\omega \lambda t + \square l) \right|
 \end{aligned} \tag{5-2}$$

where  $v$ ,  $v$ , and  $v$  represent the water quality point velocity virre in the X, Y, and Z directions, respectively, from the irregularly incident wave

,  $l$  denotes the ordinal number of the regular wave components in the irregular wave, and  $N$  denotes the regular wave component that makes up the irregular wave

Measure.  $\zeta A_l$  represents the amplitude corresponding to the  $l$ -th incident rule wave component.  $\theta \lambda$  indicates that the  $l$ -th incident regular wave component is in  $k$

The phase angle of the direction ( $k=1, 2, 3$ ),  $\varepsilon$ , denotes the random phase corresponding to the  $l$ -th incident regular wave component

$\varepsilon \lambda \in [0, 2\pi]$ .  $TF_k$  is the velocity field transfer function caused by the  $l$ -th incident regular wave component in the  $k$  direction ( $k=1, 2, 3$ ).

Number. Operator  $|$  indicates the amplitude of the parameter.  $\omega \lambda$  denotes the wave frequency corresponding to the  $l$ -th incident regular wave component. The superscripts  $I-l$  represent the parameters corresponding to the  $l$ -th incident rule wave component. Subscripts 1, 2, and 3 represent the components in the X, Y, and Z directions, respectively.

The water quality point velocity virre produced by diffracted waves under irregular waves can be expressed as:

$$\begin{aligned}
 & \text{Hymn} = \sum_{l=1}^N \left| v_{D1} \right| \sum_{k=1}^{D-l} \left| v_{TF1}^{D-l} \right| \left| \text{without}(\omega \lambda t + \square D_1 + \square l) \right| \\
 & \quad + \sum_{l=1}^N \left| v_{D2} \right| \sum_{k=1}^{D-l} \left| v_{TF2}^{D-l} \right| \left| \text{without}(\omega \lambda t + \square D_2 + \square l) \right| \\
 & \quad + \sum_{l=1}^N \left| v_{D3} \right| \sum_{k=1}^{D-l} \left| v_{TF3}^{D-l} \right| \left| \text{without}(\omega \lambda t + \square D_3 + \square l) \right|
 \end{aligned} \tag{5-3}$$

where  $v$ ,  $v$ , and  $v$  denote the water quality point velocity virre at X, Y, Z, respectively, produced by the diffracted wave under an irregular wave

The component of the direction,  $l$  denotes the ordinal number of the regular wave component in the irregular wave, and  $N$  denotes the regular wave component that makes up the irregular wave

Divide the quantity.  $\theta$  denotes the velocity of the point of the  $l$ th diffraction regular wave component in the  $k$  direction ( $k=1, 2, 3$ ) and the wave surface

The phase angle,  $\varepsilon$  denotes the random phase corresponding to the  $l$ -th incident regular wave component,  $\square l \in [0, 2\pi]$ .  $vD-l$  is the  $l$ -th winding

The velocity field transfer function caused by the component of the regular emission wave in the  $k$  direction ( $k=1, 2, 3$ ). Operator  $|$  indicates the amplitude of the parameter.  $\omega \lambda$  denotes the

wave frequency corresponding to the l-th incident regular wave component. The superscripts D-l represent the parameters corresponding to the l-th diffraction rule wave component. The subscripts 1, 2, and 3 represent the components in the X, Y, and Z directions, respectively.

The water quality point velocity virre produced by radiant waves under irregular waves can be expressed as:

$$\begin{aligned}
 \text{Hymn} = & v_R = \left\{ \sum_{j=1}^{N_6} \sum_{l=1}^{R1} \left| \sum_{d=1}^{R1} v_j^l T_{TF1}^d \right| \sin(\omega_{lt} + \theta_{R1j}^l + \delta_{R1j}^l) \right\} \\
 & + \left\{ \sum_{j=1}^{N_6} \sum_{l=1}^{R2} \left| \sum_{d=1}^{R2} v_j^l T_{TF2}^d \right| \sin(\omega_{lt} + \theta_{R2j}^l + \delta_{R2j}^l) \right\} \\
 & + \left\{ \sum_{j=1}^{N_6} \sum_{l=1}^{R3} \left| \sum_{d=1}^{R3} v_j^l T_{TF3}^d \right| \sin(\omega_{lt} + \theta_{R3j}^l + \delta_{R3j}^l) \right\} \\
 \end{aligned} \quad (5-4)$$

where,  $v_{R1}$ 、 $v_{R2}$  and  $v_{R3}$  Respectively, they represent the point velocity of water quality generated by radiation waves under irregular waves **Hymn** at  $X$ , **And**, **With**

The component of the direction,  $l$  denotes the ordinal number of the regular wave component in the irregular wave, and  $N$  denotes the regular wave component that makes up the irregular wave

The number of fractions,  $\omega_l$  denotes *the* wave frequency corresponding to the  $l$ -th incident regular wave component.  $vR_l^l$  ( $k=1, 2, 3$ ;  $j=1, 2, \dots$ ,

6) is *the radiated wave generated by the movement of the floating body in the j direction under the lth diffraction rule wave component*

向的速度场传递函数。 $u_j^l$  和  $\square_j^l$  分别为浮体质心处在波浪频率  $\square_l$  下第  $j$  ( $j = 1, 2, \dots$ ,

6) The amplitude of motion and the phase angle of the degrees of freedom,  $\varepsilon\lambda$  denotes the *random phase corresponding to the l-th incident rule wave component*

$\varepsilon\lambda \in [0, 2\pi]$ 。 The superscript  $R-l$  represents the parameter corresponding to the  $l$ -th radiation regular wave component.  $\theta_l^l$  ( $k=1, 2, 3$ ;  $j=1, 2, \dots$

6) Represents the phase angle of the velocity transfer function of the  $l$ -th radiated wave component in the  $k$  direction and the movement of the buoy in the  $j$  direction. Based on the above analysis, Eq. (5-1) can be rewritten as:

$$\text{virre} = \sum_{l=1}^{N_r} \left[ \zeta_{\text{ToTF1}} vI_l^l \sin(\omega_l t + \square_{11}^l + \square_{12}^l) + \zeta_{\text{ToTF1}} vD_l^l \sin(\omega_l t + \square_{11}^l + \square_{13}^l) + \sum_{j=1}^6 \zeta_{\text{TF1}j} u_j^l \cdot vR_{R1j}^l \sin(\omega_l t + \square_{R1j}^l + \square_{12}^l + \square_{13}^l) \right] \\ + \sum_{l=1}^{N_r} \left[ \zeta_{\text{ToTF2}} vI_l^l \sin(\omega_l t + \square_{12}^l + \square_{13}^l) + \zeta_{\text{ToTF2}} vD_l^l \sin(\omega_l t + \square_{12}^l + \square_{14}^l) + \sum_{j=1}^6 \zeta_{\text{TF2}j} u_j^l \cdot vR_{R2j}^l \sin(\omega_l t + \square_{R2j}^l + \square_{13}^l + \square_{14}^l) \right] \\ + \sum_{l=1}^{N_r} \left[ \zeta_{\text{ToTF3}} vI_l^l \sin(\omega_l t + \square_{13}^l + \square_{14}^l) + \zeta_{\text{ToTF3}} vD_l^l \sin(\omega_l t + \square_{13}^l + \square_{15}^l) + \sum_{j=1}^6 \zeta_{\text{TF3}j} u_j^l \cdot vR_{R3j}^l \sin(\omega_l t + \square_{R3j}^l + \square_{14}^l + \square_{15}^l) \right] \quad (5-5)$$

(2) Statistical analysis of water quality point velocity in disturbance wave field considering the influence of buoy disturbance under irregular waves

In this chapter, the JONSWAP wave spectrum is used to analyze the load extreme response for three different operating conditions, and the operating parameters are shown in Table 3-4. In order to ensure that the wave surface elevation within three hours does not repeat, the wave frequency interval is set

Set to a random number of no more than 0.1 rad/s. To eliminate the effect of the transient response, the calculation time is set to 11000 s.

The analysis step interval is set to 0.1227 s, which ensures that the time interval is small enough to capture the response of the smallest periodic regular wave component.

In order to study the interference of diffracted and radiated waves generated by floating bodies under irregular waves on the wave field, fig 5-1 ~ fig 5-6 The root mean square of the velocity field around the net coat and the water quality point velocity of the water quality point that takes into account the disturbance of the floating body under different working conditions is given (RMS) value. When only the incident wave is considered, in **X** and **With** The maximum water quality point velocity in the direction RMS The values are: 1.44 m/s and 1.40 m/s, when taking into account the interference of diffracted and radiated waves on the

velocity field, in *X and Z* The maximum water quality point velocity in the direction RMS values were reached 2.00 m/s and 1.74 m/s, the increase was reached 39% and 24%。 in working conditions LC1 and LC2 , the point velocity of water quality due to diffracted waves and radiated waves is in *Separately increased in the X direction* 20% and 29% at *With* The direction has been increased separately 14% and 19%。 In the figure, it can be observed that the areas of increased velocity in the wave field are located near the still water surface of the net, especially the increase is more obvious in the areas where the mesh is connected, and these regions are also the main areas of increase in the point velocity of water quality under regular waves. In addition, while diffracted waves and radiant waves are in *X* In the direction, the amplitude of the disturbance to the wave field is larger and the change is more obvious, but the overall floating disturbance does not change the distribution trend of the velocity field. at *And* In the direction, the disturbance of the buoyancy is mainly concentrated in the area close to the buoy.

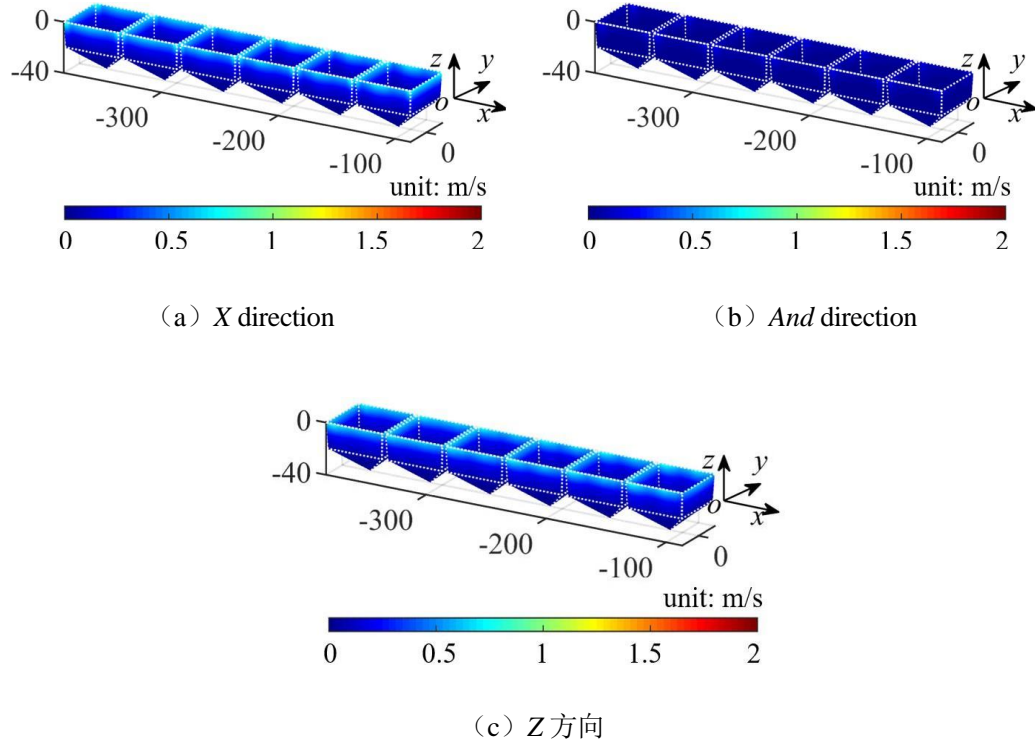


图5-1 工况LC1下由入射波、绕射波和辐射波共同引起的网衣周围速度场水质点速度RMS值

Fig. 5-1 The root mean square of the velocity field around the net induced by the incident wave, diffraction wave and radiation wave under LC1

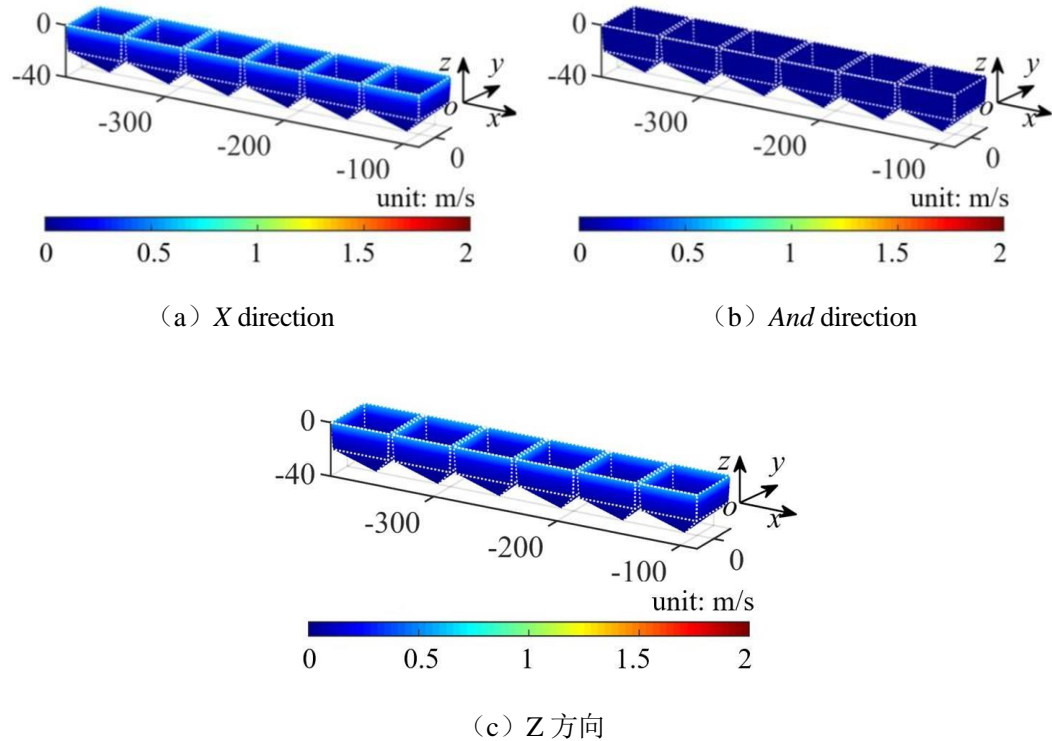


Figure 5-2 RMS values of the velocity field water quality point velocity around the mesh caused by the incident wave at LC1

Fig. 5-2 The root mean square of the velocity field around the net induced by the incident wave under LC1

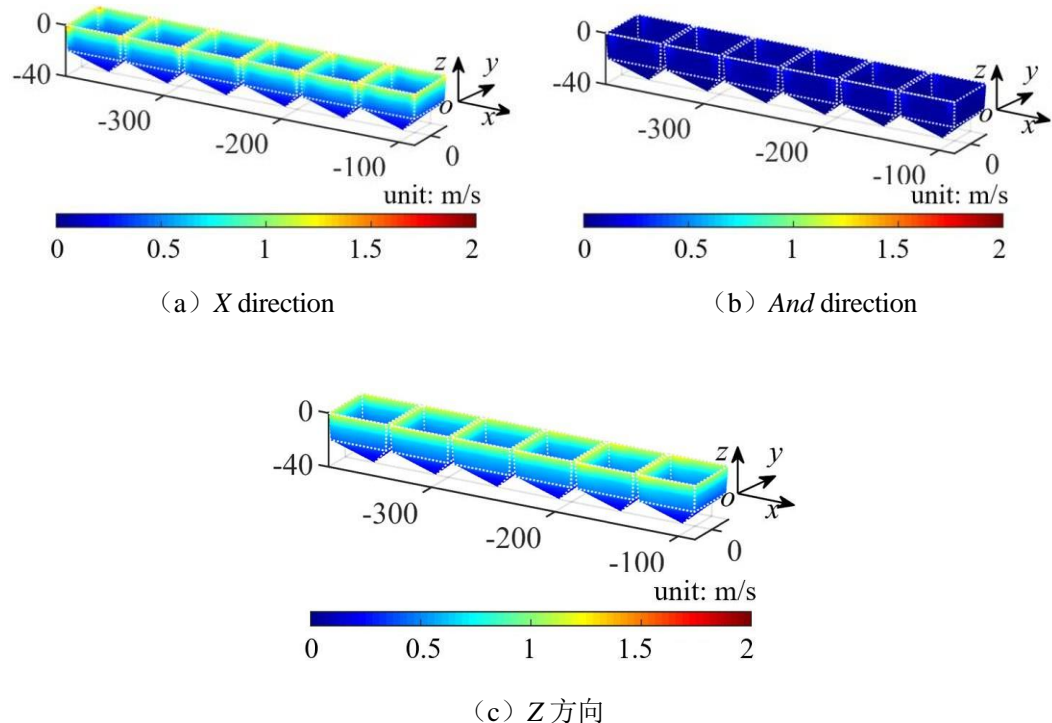


图5-3 工况LC2下由入射波、绕射波和辐射波共同引起的网衣周围速度场水质点速度RMS值

Fig. 5-3 The root mean square of the velocity field around the net induced by the incident wave, diffraction wave and radiation wave under LC2

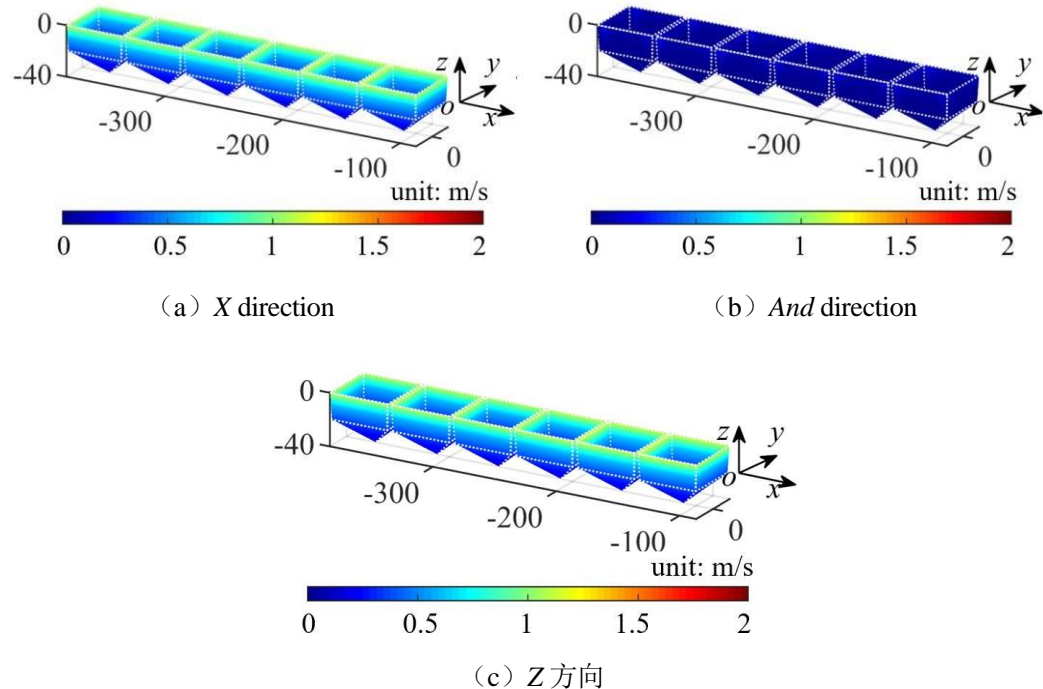


Figure 5-4 RMS values of the velocity field water quality point velocity caused by the incident wave at LC2 under the operating condition

Fig. 5-4 The root mean square of the velocity field around the net induced by the incident wave under LC2

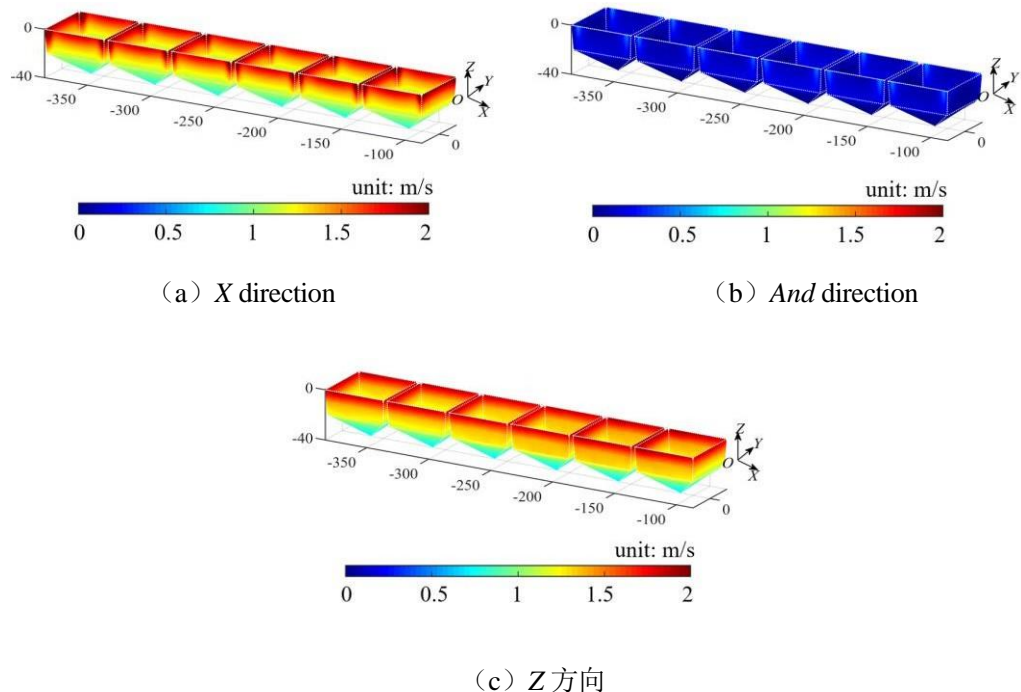


图5-5 工况LC3下由入射波、绕射波和辐射波共同引起的网衣周围速度场水质点速度RMS值

Fig. 5-5 The root mean square of the velocity field around the net induced by the incident wave, diffraction wave and radiation wave under LC3

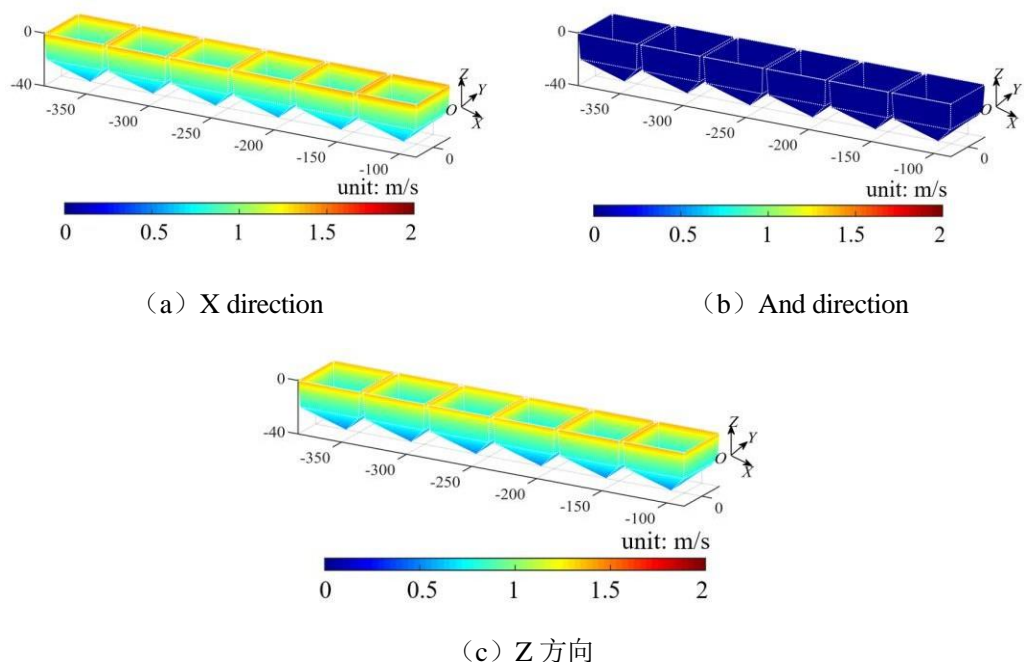
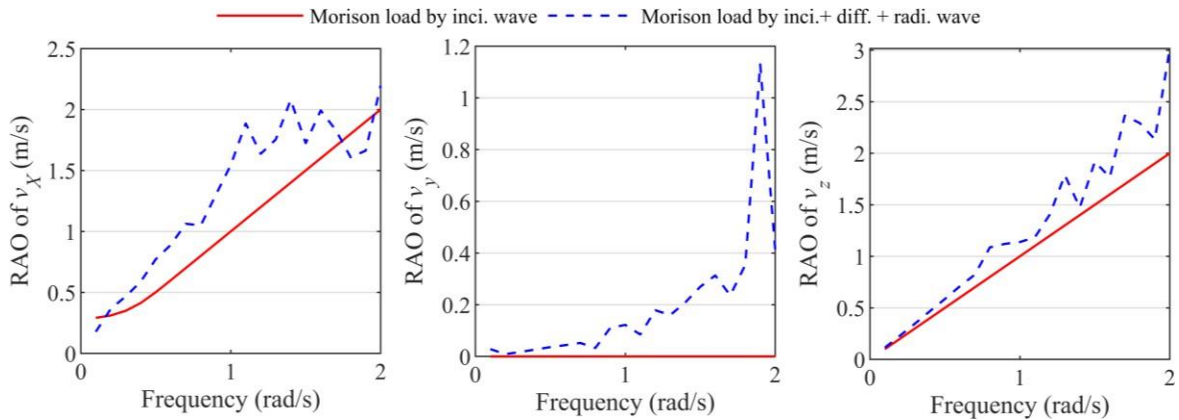
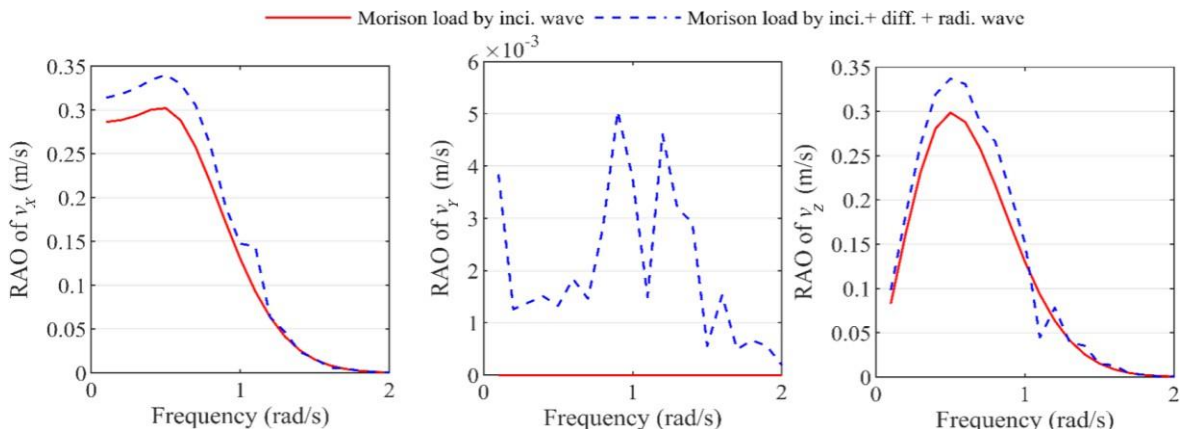


Figure 5-6 RMS values of the velocity field around the mesh caused by the incident wave at LC3  
 Fig. 5-6 The root mean square of the velocity field around the net induced by the incident diffraction and radiation wave under LC3



(a) The corner of the net is near the still water



(b) The corners of the netting are near the bottom of the side netting

Figure 5-7 Water quality point velocity RAO in three directions at different locations

Fig. 5-7 RAO of the water-particle velocity in three different directions

fig 5-7 is the response amplitude operator (response amplitude operators , RAO)。 fig 5-8 It is the spectral density function of the point velocity of the water quality near the corner of the still water surface of the net under different working conditions. It can be seen from the figure that when the influence of diffraction and radiation waves generated by the floating body is taken into account, the water quality point velocity in the key areas of the net coat (such as the corner of the net coat) will increase significantly, resulting in the local increase of the net tension.

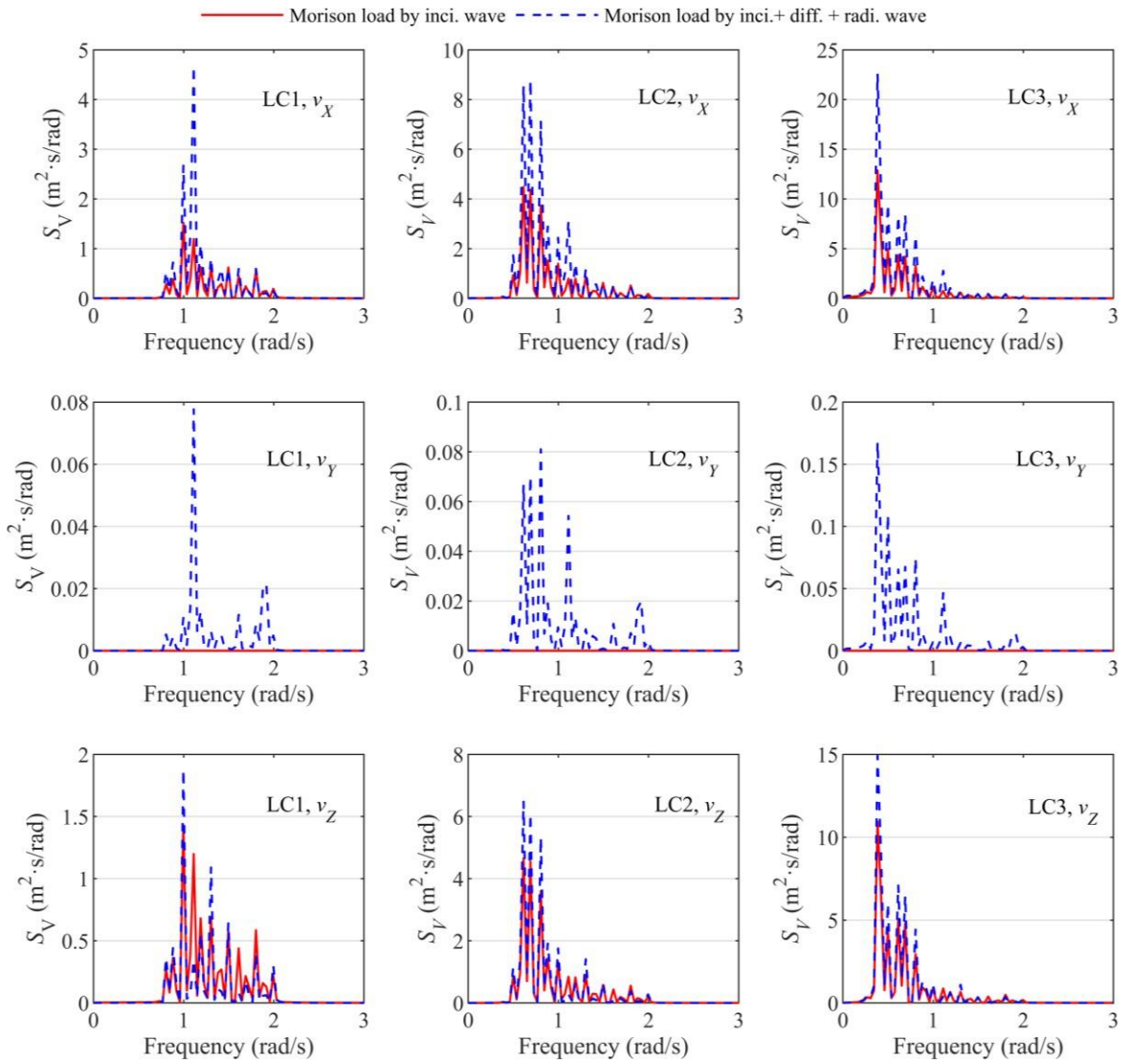


Figure 5-8 Velocity spectral density of water quality points at the corners of the net near the still water surface under different working conditions

Fig. 5-8 Spectral density of the water-particle velocity at the net corner near the still water surface under different load cases

### 5.2.2 The dynamic response analysis process of large cage considering the influence of disturbed wave field on net clothing under irregular waves

After obtaining the irregular wave velocity field, which takes into account the effects of diffracted and radiated waves, hydrodynamic calculations can be made for nets and steel frames according to Morrison's formula, which is consistent with the analytical approach in Chapter 4. Under irregular waves, the radiative load of the large cage buoy is solved by the state space method, so the coupled dynamic response equation of the large cage can be written as:

$$\begin{aligned}\mathbf{M}\ddot{\mathbf{u}}(t) + \mathbf{K}\mathbf{u}(t) + \Phi P\alpha\delta(t) &= \mathbf{FW}(t) + \mathbf{FCouple}(t) \\ \mathbf{FCouple}(t) &= \mathbf{FH}(t) + \Phi\Gamma(t) + \Phi\mathbf{B}(t) - \Phi\mathbf{I}(t)\end{aligned}\quad (5-6)$$

where  $\mathbf{FW}(t)$  denotes the wave excitation force acting on the buoy,  $\mathbf{FRad}(t)$  is the radiant load of the buoy, and  $\mathbf{FCouple}(t)$

Represents the coupling load terms of the net and steel frame on the buoy under irregular waves,  $\mathbf{FH}(t)$ ,  $\mathbf{FG}(t)$ ,  $\mathbf{FB}(t)$  and  $\mathbf{FI}(t)$  represent the integral terms of the hydrodynamic load, gravity, buoyancy and inertial force load at the center of the floating mass of the net and steel frame, respectively. In the calculations of this chapter, the viscous load of the buoy is neglected.

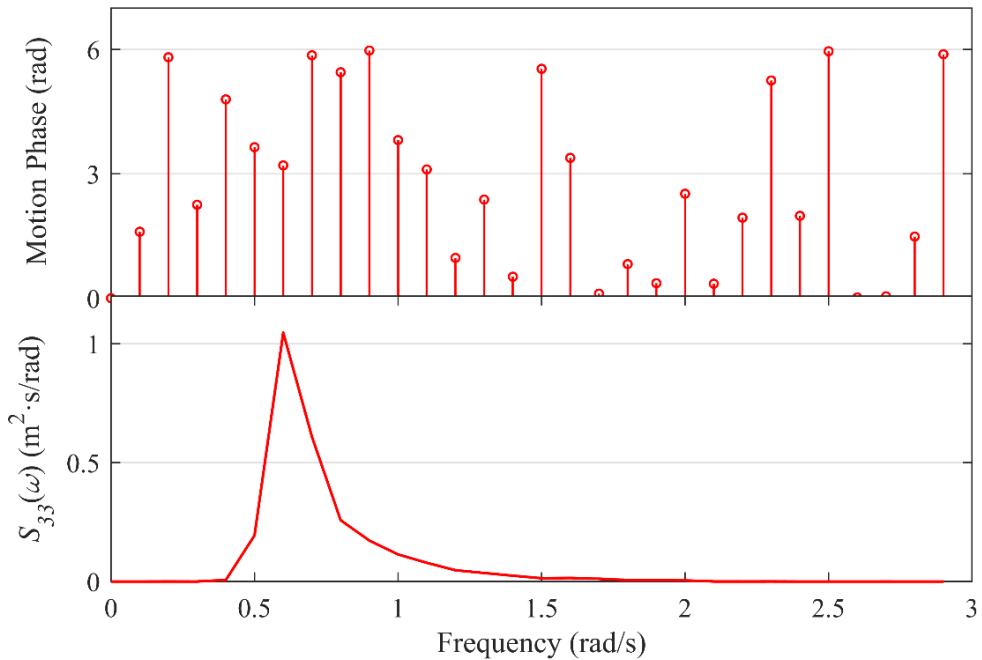


Figure 5-9 Cage swing amplitude and phase angle obtained by FFT, with a sense wave height of 5 m and a peak period of 10 s

Fig. 5-9 The spectral density and phase angle of heave motion obtained by FFT under irregular waves of  $HS = 5$  m and  $TP = 10$  s

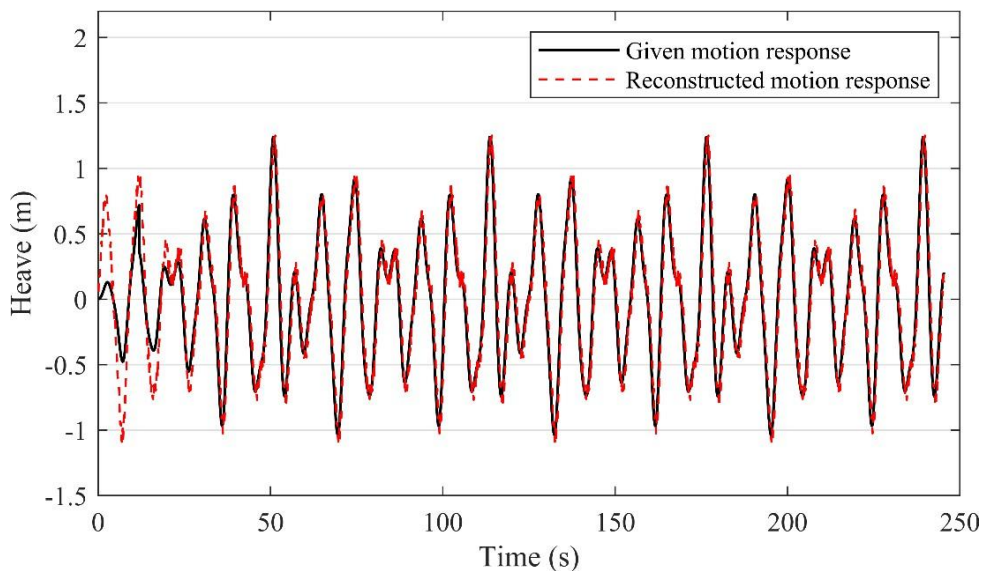


Figure 5-10 Comparison of the heave time of the cage under irregular waves and the time history obtained by amplitude and phase reconstruction (sense wave height 5 m,

谱峰周期 10 s)

Fig. 5-10 Comparison between the given heave motion of the floating body and the reconstructed time series based on the motion amplitudes and phase angles under irregular waves ( $HS = 5$  m and  $TP = 10$  s)

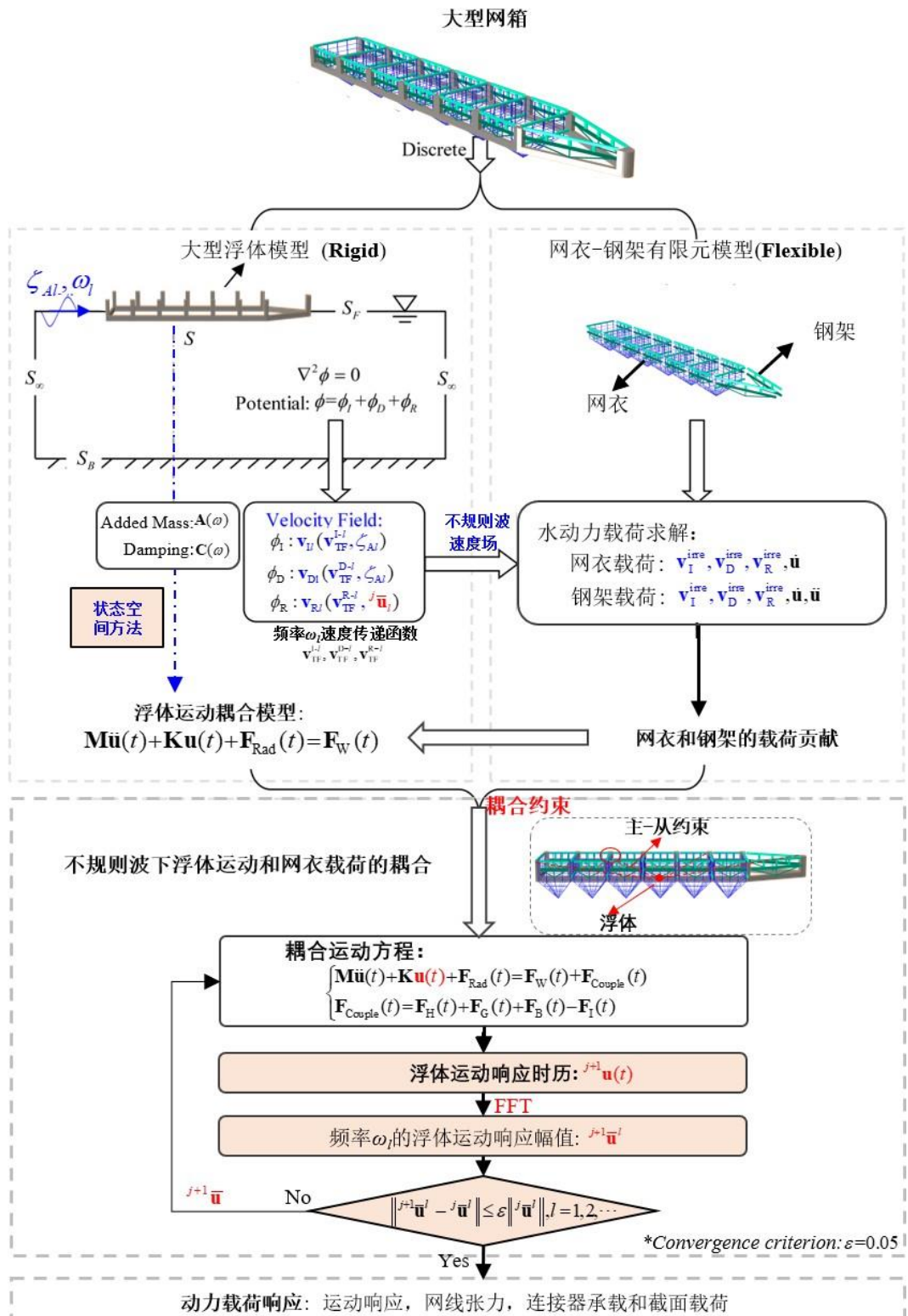


Figure5-11 Coupling dynamic analysis process of large cage under irregular waves

Fig. 5-11 Flowchart of large fish cage coupling analysis under irregular waves

Based on the above coupling dynamic equations of large cages, the influence of diffracted waves and radiated waves is considered under irregular waves

The load analysis method of large cages (i.e., disturbed irregular wave field) is summarized as follows: firstly, the first iterative calculation is carried out, in which the influence of the radiation wave of the buoy body is not considered, and the velocity field only considers the action of the corresponding irregular incident wave and the generated diffracted wave, and the preliminary irregular wave velocity field without radiation wave is constructed, and then the coupled motion equation of the whole cage under the irregular wave is solved in the time domain, and the floating centroid motion time calendar of  $1u$  considering the influence of the load of the net coat and the steel frame is obtained( $t$ ), the amplitude of motion  $1 \text{ ul}$  and the phase angle  $j \square 1\delta l$  of each wave frequency corresponding to  $1u(t)$  are οβτανεδ βψ φαστ Φουριερ τρανσφορμ .

fig 5-9 It is the amplitude, phase, and graph of the motion of a large cage obtained by using the fast Fourier transform 5-2 It is a motion calendar based on the resulting motion amplitude and phase reconstruction. composed fig 5-10 shown, adopted FFT The amplitude and phase of the motion obtained by the method are accurate.

The final stable results are achieved through iterative calculations, and the iterative process is developed from the analysis process in Chapter 4. The specific analysis process is described as follows: in the first iteration of the calculation, according to  $1 \text{ ul}$  and  $1\delta l$  at each frequency, the disturbance wave field containing the influence of radiation waves is reconstructed for the coupling dynamic calculation of the next large cage under irregular waves. Through continuous iterative calculations, the  $j \square 1ul$  and  $\square 1\delta l$  of the  $j+1st$  cycle and  $j ul$  of the  $jth$  cycle are compared .

$j \delta l$  if satisfied at all wave frequencies  $j \square 1ul - j \text{ ul} \leq \varepsilon \quad \frac{j}{ul}$  (set  $\varepsilon = 0.05$ )

The iterative calculation was stopped, and the dynamic results of the cage under disturbance irregular wave were analyzed. If not, the next calculation is performed iteratively until a stable result is obtained. Figure 5-11 shows the coupling analysis process of large cages for considering the influence of buoys on the net under irregular waves , which is basically the same as the dynamic response analysis process of the cage considering the influence of the disturbance wave field under regular waves, but it is very different when obtaining the motion response of the cage, constructing the disturbance wave field and quasi-static analysis, and should be noted.

### 5.3 Analysis of cage buoy motion considering the influence of disturbance wave field on net coat under irregular waves

Figure 5-12 is the motion response time of the cage under irregular waves and the corresponding response amplitude at different wave frequencies. It can be seen from the figure that the motion response of the cage is mainly dominated by the wave frequency load,

and when the influence of diffraction wave and radiated wave is considered, it almost coincides with the motion response under the action of the incident wave, and the motion amplitude at different frequencies also has the same characteristics. On the one hand, this is due to the fact that the hydrodynamic load on the buoy itself occupies a dominant position in the process of cage movement, and on the other hand, because the diffraction wave and radiation wave have limited influence on the velocity field, the velocity of the water quality point only increases at some local positions, resulting in the local increase of the hydrodynamic force of the net and the steel frame, but the influence on the two is limited at a certain time, that is, the overall hydrodynamic change of the net system is not obvious at this time. Therefore, the diffracted and radiated waves generated by the mesh and steel frame hydrodynamic loads and the floats have little influence on the movement of the cage. Based on the above analysis, the influence of diffracted and radiated waves generated by the buoys can be ignored in the analysis of the cage motion response under irregular waves.

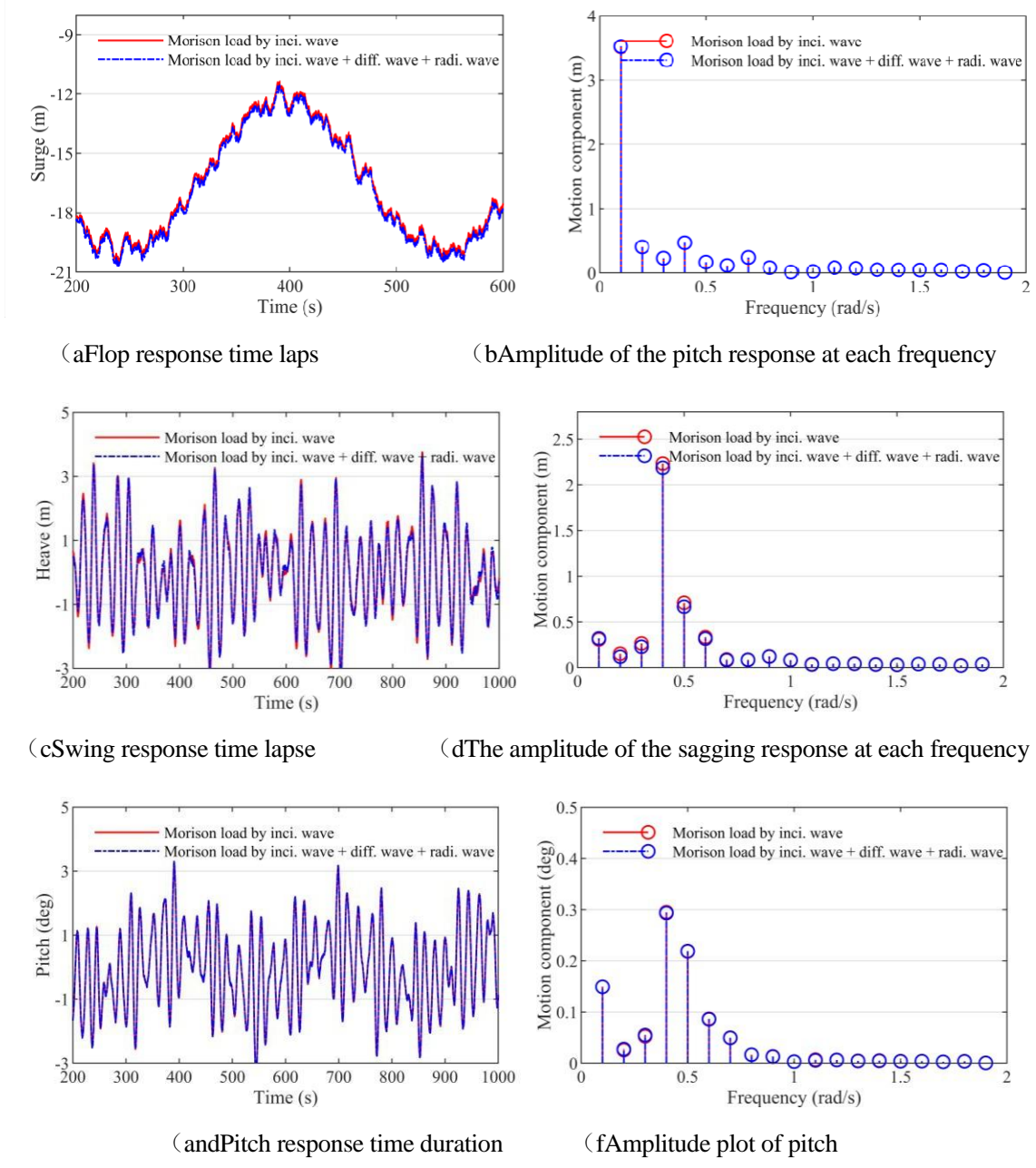


Fig. 5-12 The motion response of the vessel-shaped fish cage and the corresponding frequency components under LC3

#### 5.4 Analysis of the influence of the disturbed wave field on the tension of the net under irregular waves

In cages from bow to stern 6 breeding units Net 1~Net 6 , each unit is subjected to approximately the same environmental load. Thus this chapter will: Net 1 Divided into 8 mesh surfaces (side nets are s1~s4, the bottom net is b1~b4 see fig 5-13 and Fig 5-14).

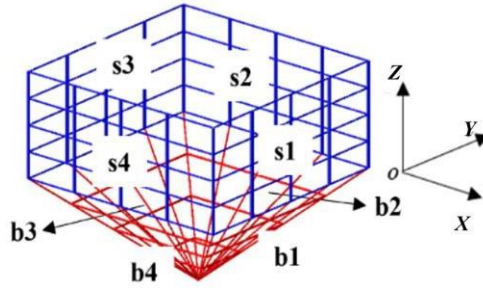


Figure 5-13 Different Mesh Surfaces of Net 1

Fig. 5-13 The different net panels of Net 1

Figure 5-14 shows the maximum RMS values for all cable tensions on different screens under LC1. In the wave-facing condition, the cable tension levels of the mesh S1 and S3 are significantly higher than those of the other meshes. According to the above analysis, it can be seen that the tension of the network cable at the horizontal edge of the mesh surface is higher than that of other positions, so the analysis of the network cable tension at these positions should be focused on from the perspective of mesh security.

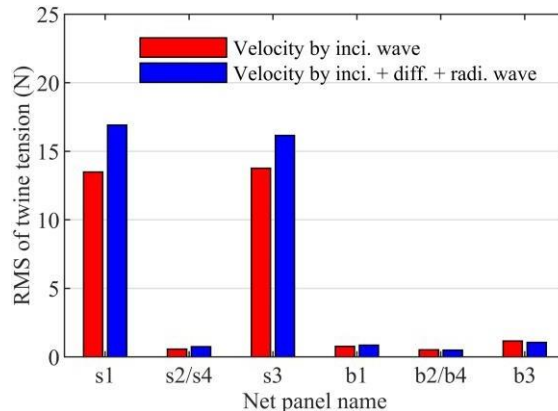


Figure 5-14 Maximum RMS values for different mesh tensions

Fig. 5-14 The maximum of tension RMS value at the different net panels

fig 5-15 It's mesh s1 Maximum tension level time lapse under different operating conditions, fig 5-16 is the corresponding spectrum analysis. As the wave height increases, the maximum network cable tension is taken into account, taking into account the effects of diffracted and radiated waves LC1~LC3. The following were added 12%、27% and 49%. The same growth trend can also be seen in the corresponding spectrum analysis results. According to the hydrodynamic calculation formula of the net, the relationship between the load of the net and the velocity of the water quality point is approximately quadratic. With the increase of the water quality point velocity caused by diffraction and radiation waves, the impact of buoy disturbance will gradually increase. In addition, it can be seen from the spectral analysis results that the wave frequency range that leads to the increase of network cable tension is mainly lower 0.5 rad/s scope.

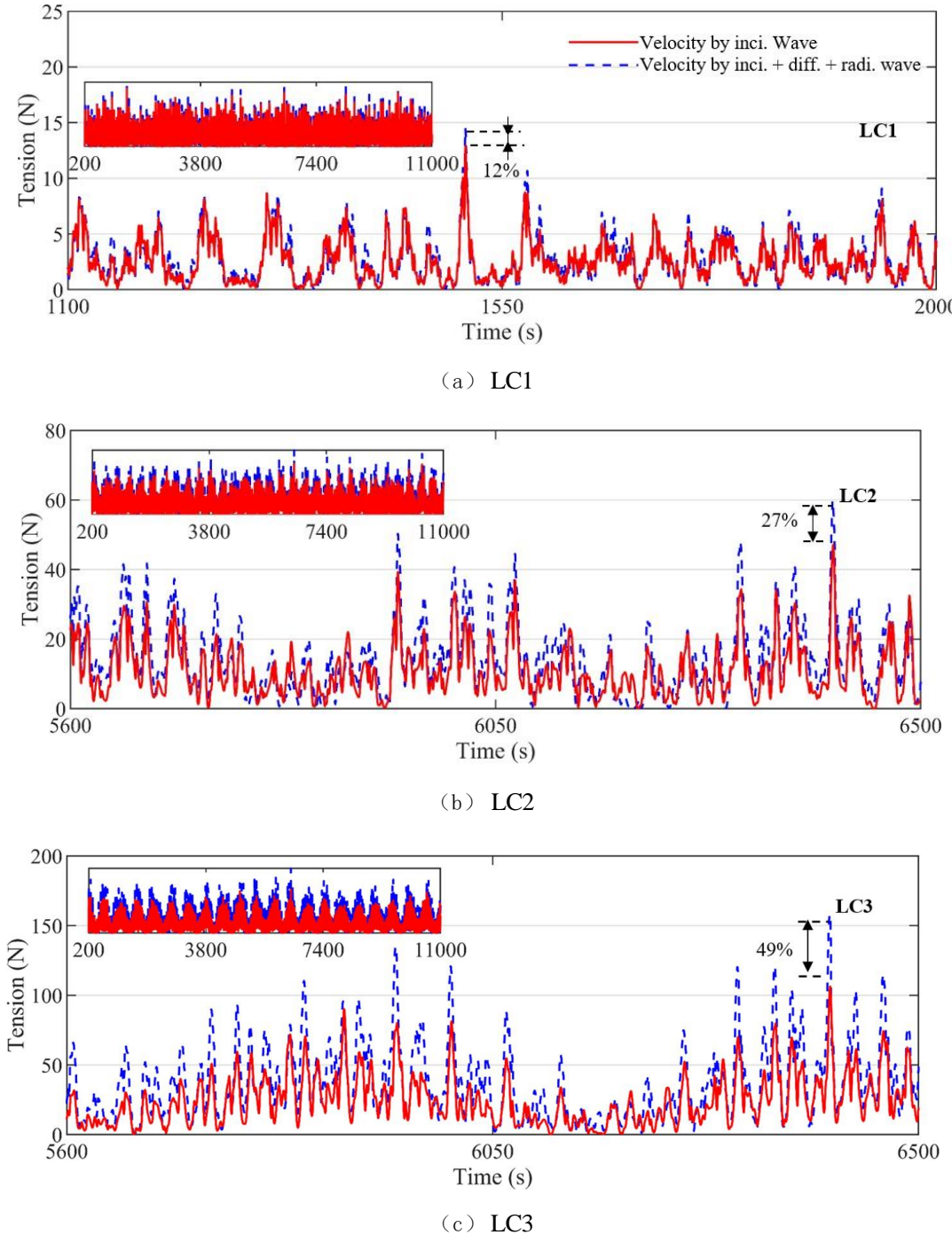


Figure 5-15 Tension time history of the maximum tension region at S1 of the mesh surface under different working conditions

Fig. 5-15 The time histories of twine tension at the maximum twine tension area of s1

Figure 5-17 is the standard deviation and extreme tension contour of the network cable tension of the breeding unit Net1 under different working conditions. For each irregularity case in this chapter, only one seed is selected, and the response extremum is assumed to satisfy the Weibull distribution, and the 99% quantile is selected as the response extremum. Although the calculation of only one seed will bring more uncertainty to the calculation results, the calculation results are still valuable because the wave surface elevation time calendar is the

same because the influence of buoys on the net coat is considered. As can be seen from the figure, the standard deviation of the network cable tension increases with the increase of the sense wave height

and tension extremes are also larger, with the maximum standard deviation and tension extremes increasing by a factor of about 17 and 8 times for LC2 and LC3 compared to the results for LC1.

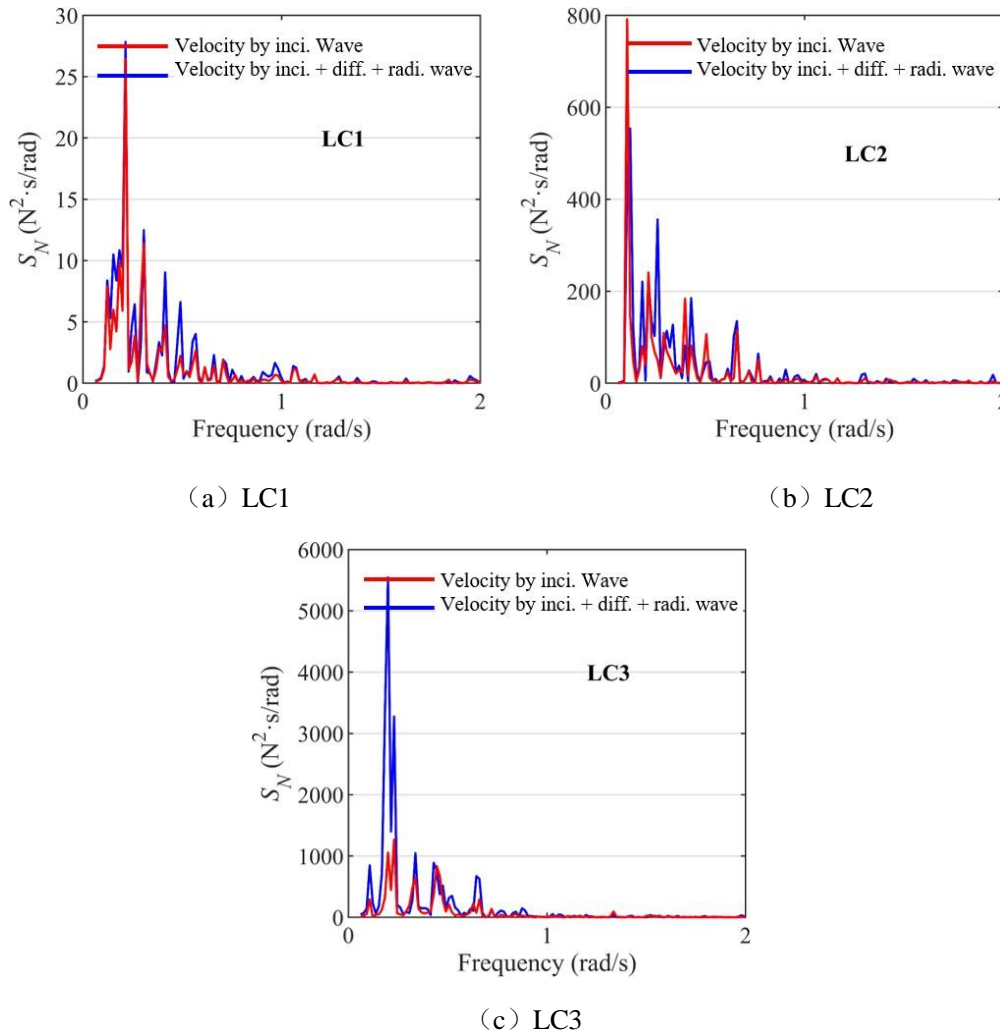
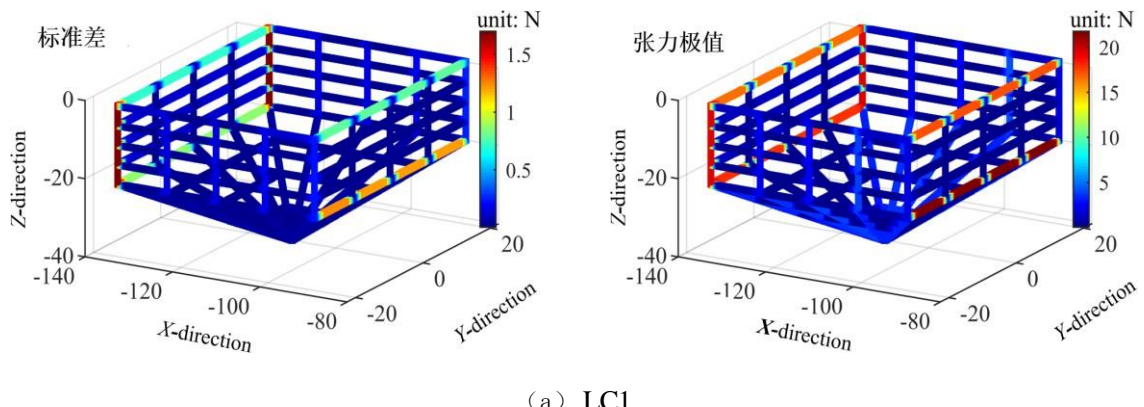


Figure 5-16 Spectral density of the maximum tension region at S1 of the mesh surface under different operating conditions

Fig. 5-16 The spectral density of twine tension at the maximum twine tension area of s1



(a) LC1

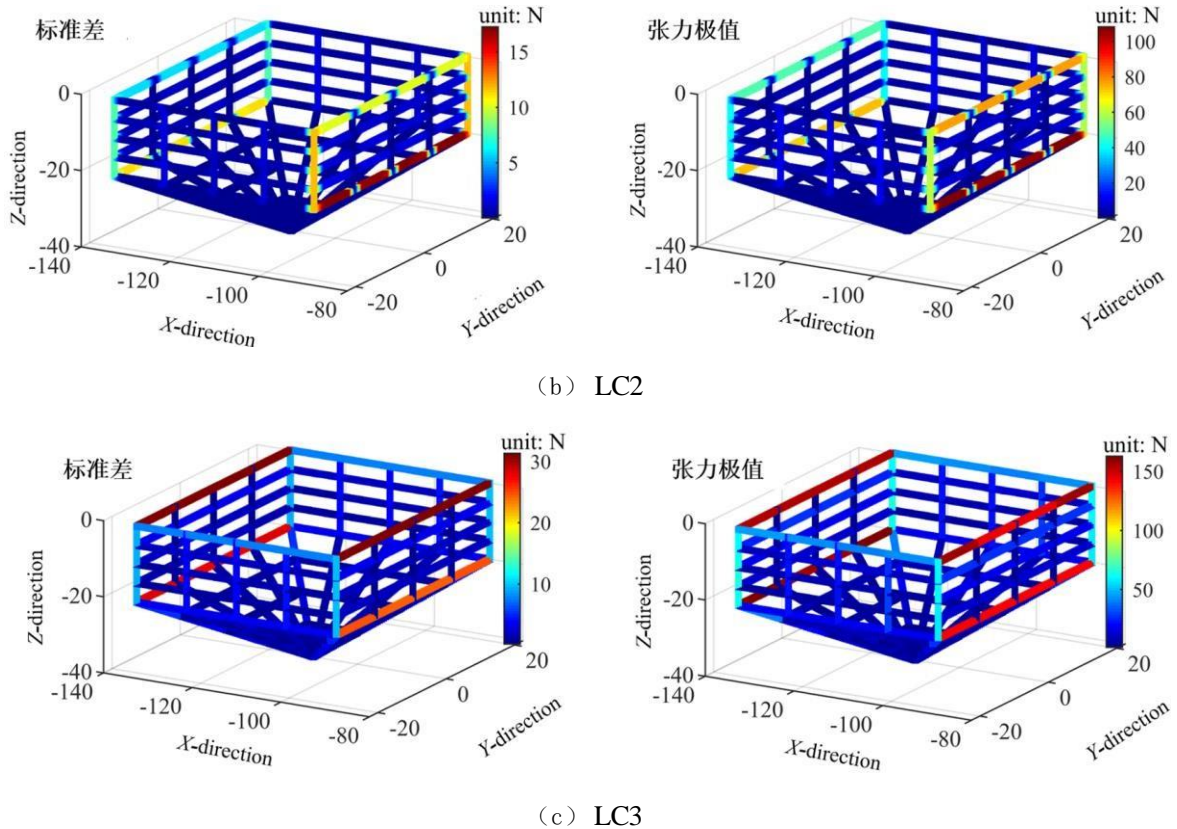


Figure 5-17 Net 1 Tension Standard Deviation and Extreme Evaluations for Diffracted and Radiated Waves under Different Operating Conditions

Fig. 5-17 The standard deviation of tension and the estimated extreme of tension of Net 1 considering diffraction and radiation waves under different wave conditions

In all cases, the maximum values of the standard deviation and extreme values of the cable tension occur at the horizontal cables where the mesh is S1 and S3. Even the horizontal network cable tension at the bottom is higher than the network cable tension in the middle position, which is due to the limitation of the edge connector, so that the bottom horizontal network cable can not offset the impact of the incoming flow through its own deformation movement, resulting in the network cable tension is significantly higher than the tension in the middle area of the mesh surface. This also shows that although the limitation of the connector can reduce the deformation of the mesh and help maintain the breeding volume, it will also have an adverse impact on the structural safety of the net.

## 5.5 Analysis of the influence of disturbance wave field on connector load under irregular waves

The large cage in this article has a total of 120 connectors, which are *symmetrically distributed along the XOZ plane, divided into upper and lower connectors, as shown in Figure 3-25*. From the above analysis, it can be seen that for the connector of the same breeding unit, the bearing capacity of the edge connector of the upper layer is significantly

---

greater than that of the other connectors.

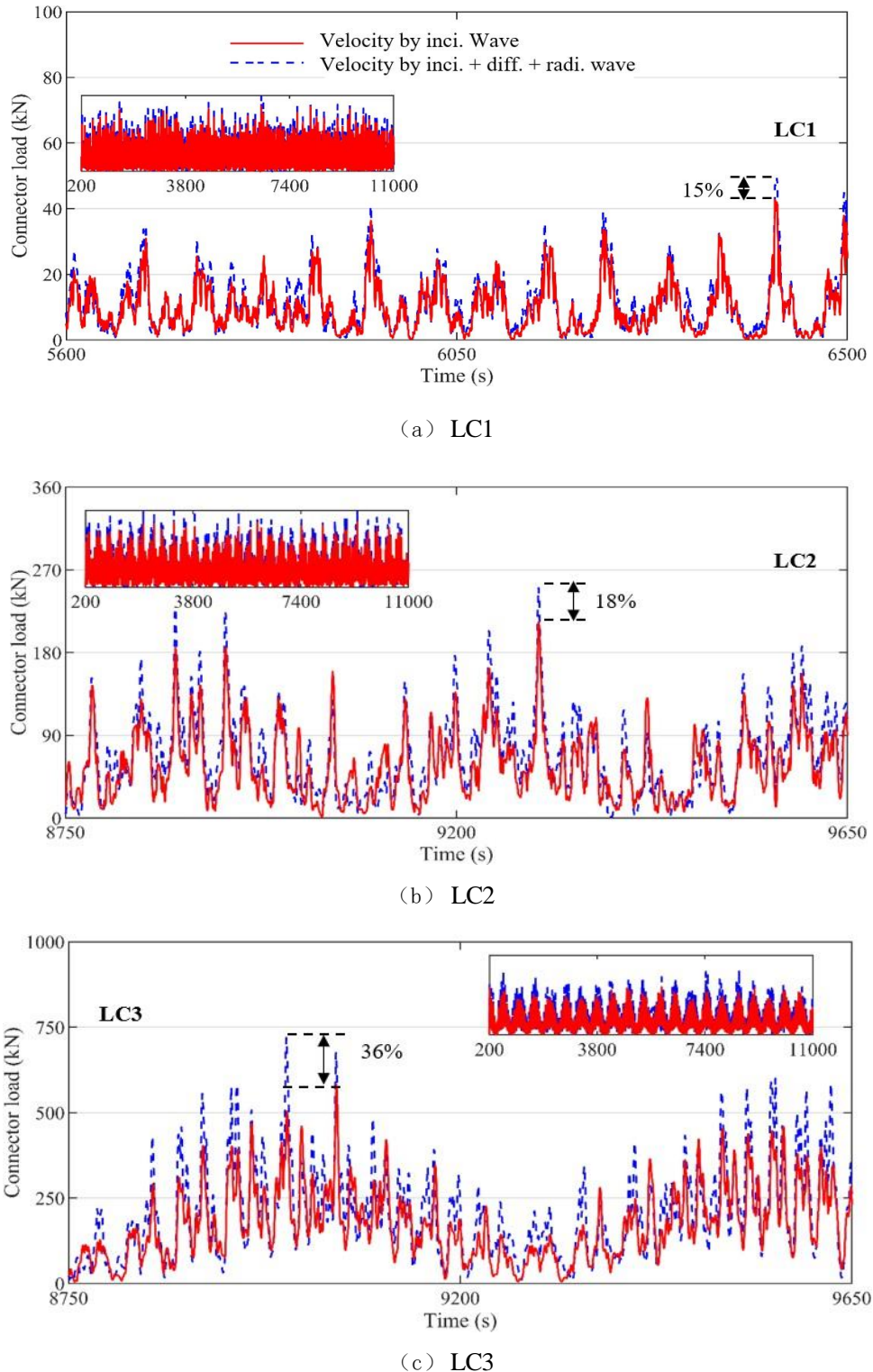


Figure 5-18 Bearing time of connector 5 under different operating conditions

Fig. 5-18 The time histories of load effect on connector 5 under different condition cases

fig 5-18 It is an upper edge connector 5 Bearing time under different working conditions, fig 5-19 It's a connector 5 The response spectral density of the bearing time lapse under different operating conditions. at LC1~LC3 Under different working conditions, the connector takes into account the influence of diffracted waves and radiated waves 5 The maximum load was

---

increased, respectively 15%, 18% and 36%. Among them: LC1 and LC2 middle

Whether the influence of diffracted wave and radiated wave is taken into account, the maximum connector bearing value occurs at the same time, but the maximum connector bearing time is different under LC3, which indicates that the influence of diffracted wave and radiated wave on connector bearing will be more obvious as the sea conditions become worse, and even change the trend of local peaks. As can be seen from Figure 5-19 , the overall spectral density increases when the diffracted and radiated waves are accounted for, rather than a local increase at certain frequencies, indicating that the diffracted and radiated waves generated by the buoyancy have a certain degree of influence on the connector bearing at all wave frequencies.

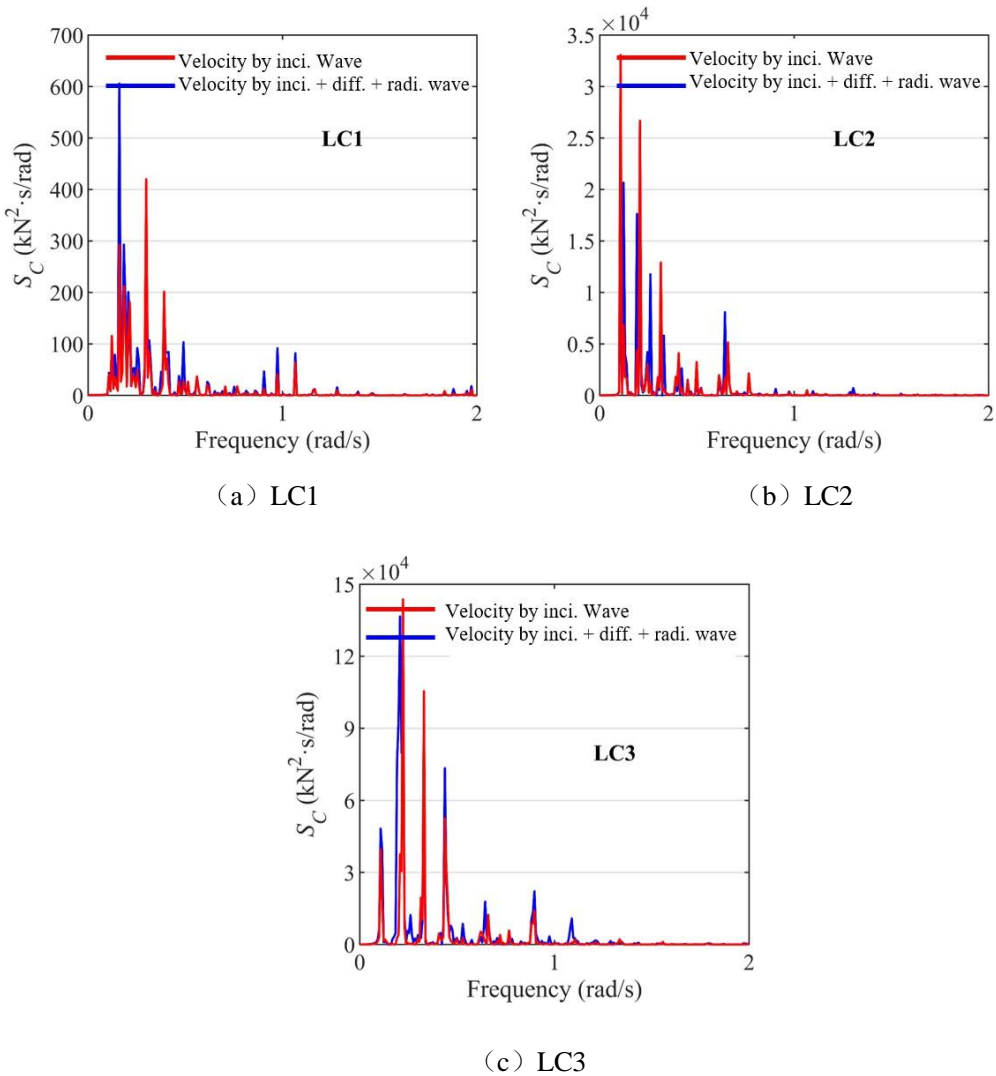


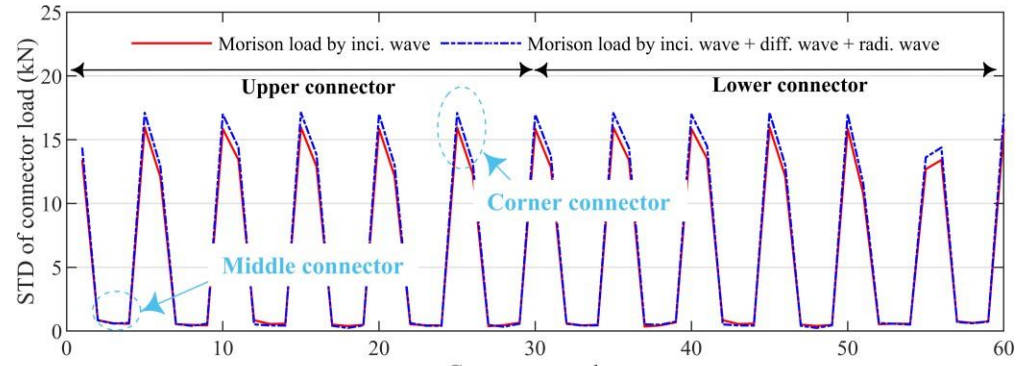
Figure 5-19 Bearing spectral density of connector 5 under different operating conditions

Fig. 5-19 The spectral density of load effect on connector 5 under different condition cases

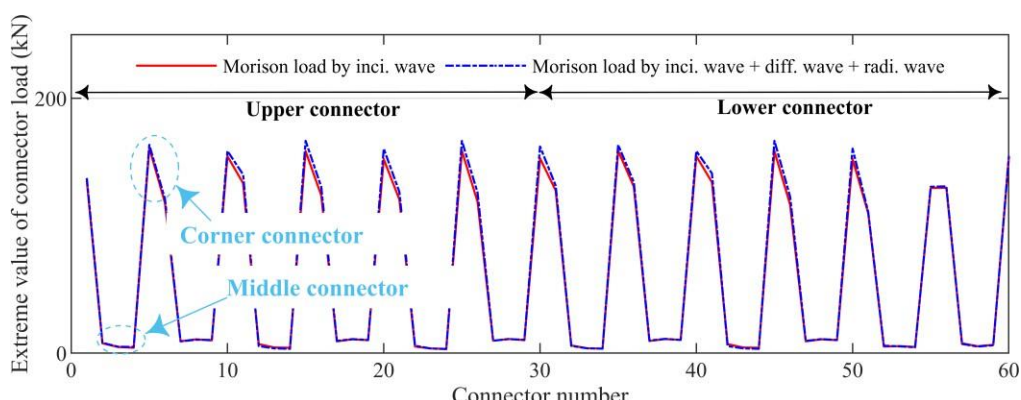
fig 5-20、fig 5-21 and fig 5-22 They are the working conditions LC1~LC3 under the connector 1~Connector 60 Statistical results of the standard deviation of the bearing and the extreme value of the bearing. composed fig 5-20~fig 5-22 It can be known that from LC1 reach LC3, the bearing capacity of the connector gradually increases, and the influence of diffracted waves and radiated waves is also gradually significant. in working conditions

LC3 , the maximum extremum value evaluated by the connector is located at the connector 5, when taking into account the effects of diffracted and radiated waves, the carrying extremum is reached 821kN, excluding the influence of diffracted and radiated waves, the bearing value is 636 kN, the increase reached 29%, and in the connector 10 position, bearing the increase even reached 32%。 For different farming units, the load distribution law is maintained

consistent, and the standard deviation and extremum of the edge connector were evaluated significantly more than the results for the middle connector. Overall, when taking into account the effects of diffracted and radiated waves, the increase carried by the connector is less than the maximum increase in the tension of the network cable.



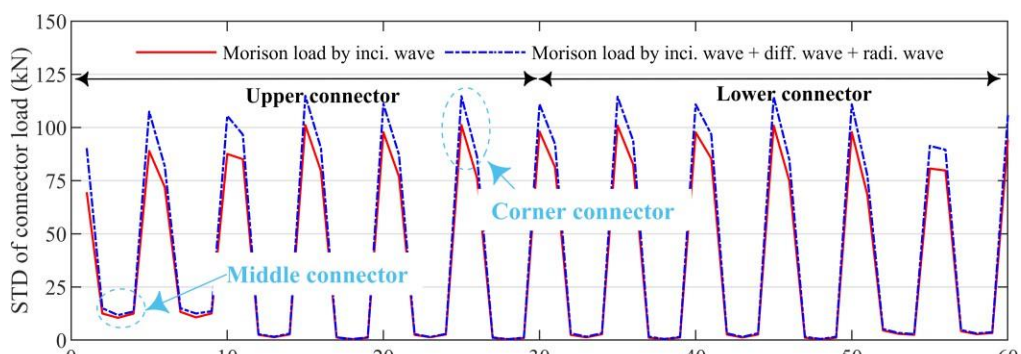
(a) 承载标准差



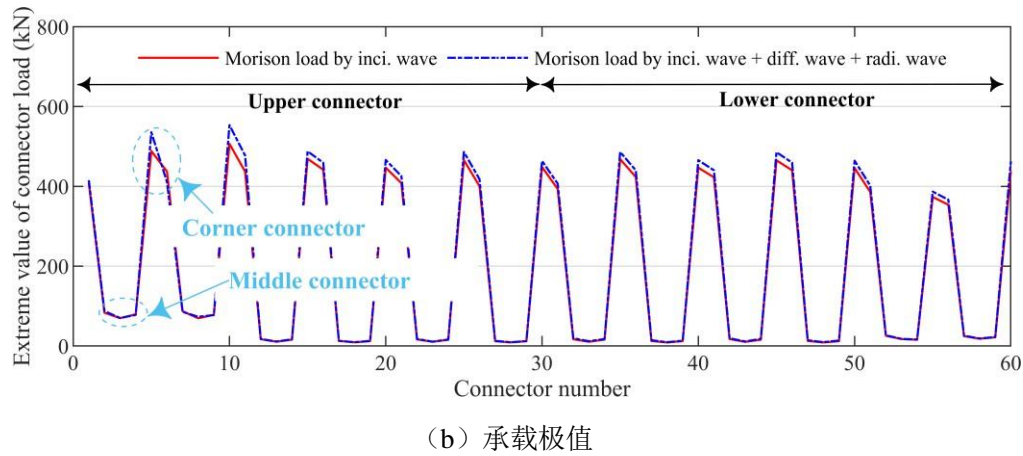
(b) 承载极值

Figure 5-20 Standard deviation and load carrying extreme results of connectors on the same side of the cage under LC1

Fig. 5-20 The Standard deviation and estimated extreme value of loads effect on connectors under LC1



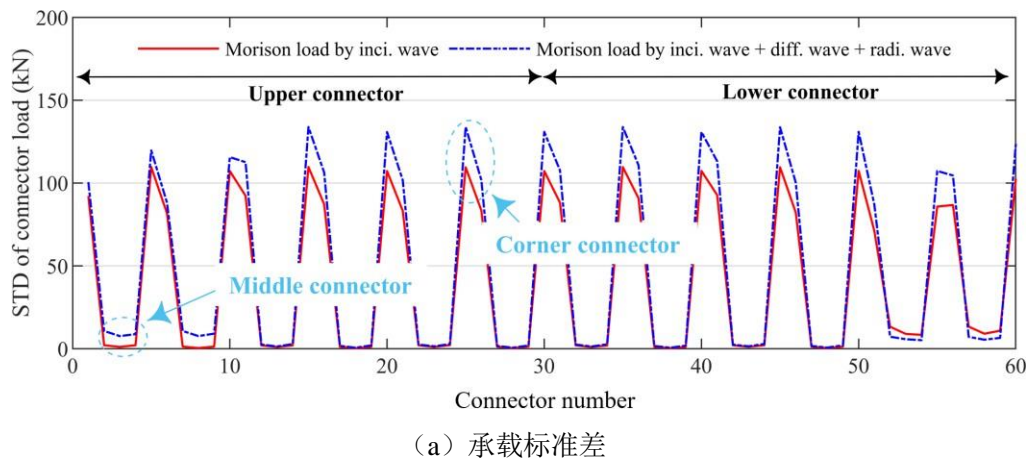
(a) 承载标准差



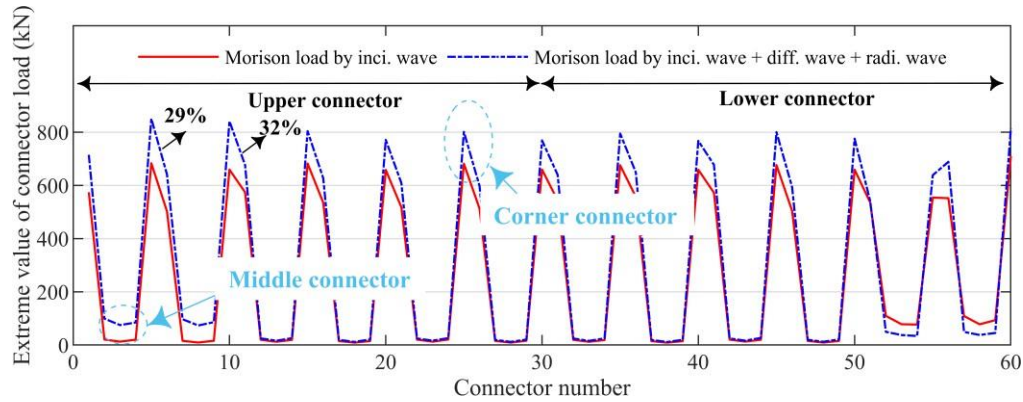
(b) 承载极值

Figure 5-21 The standard deviation and extreme load bearing results of the connector on the same side of the cage under LC2

Fig. 5-21 The Standard deviation and short term estimated extreme value of loads effect on connectors under LC2



(a) 承载标准差



(b) 承载极值

Figure 5-22 Standard deviation and short-term extreme value evaluation of connectors on the same side of the cage under LC3

Fig. 5-22 The Standard deviation and short term estimated extreme value of loads effect on connectors under LC3

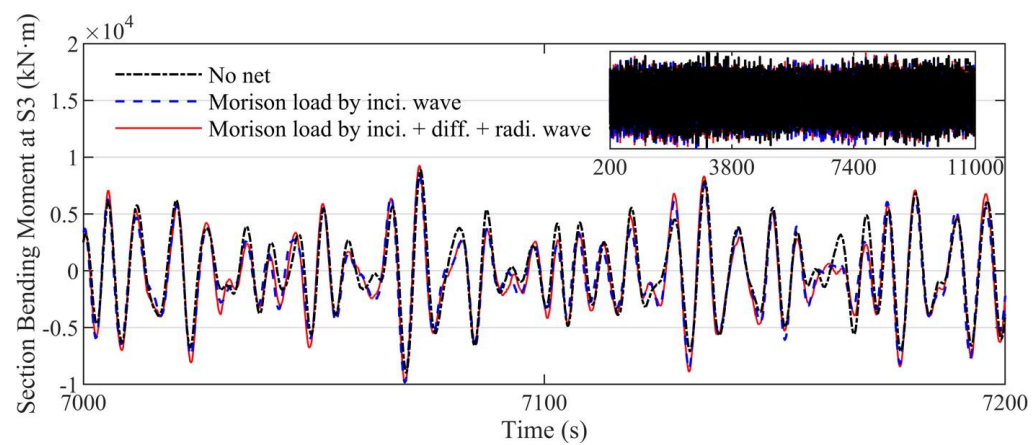
## 5.6 Analysis of the influence of cage cross-sectional load considering the influence of disturbance wave field on net clothing under irregular waves

In this section, the cross-sectional load of the steel structure of the main steel structure of a large cage is analyzed under irregular waves. The cross-section load is calculated by the quasi-static method, and the cross-section used is shown in Figure 3-19, and the cross-section from the bow to the stern is named S1~S7 respectively.

### 5.6.1 Analysis of the influence of bending moments on cross-sections

fig 5-23 It is a cross-section under different working conditions S3 vertical moment time calendar, fig 5-24 It is a cross-section under different working conditions S3 The spectral density curve corresponding to the vertical bending moment. in working conditions LC1~LC3 Bottom, cross-section S3 The vertical moment increases gradually. In the three cases, the vertical bending moment without considering the net load is not much different from the result when the net load is taken into account LC1 The cross-sectional load without taking into account the mesh load will even be slightly greater than the result with the net. When considering the mesh load, taking into account the effects of diffracted and radiant waves results in a slight change in the cross-section load, but the magnitude of the change is almost negligible. In the spectral density results, the self-operating condition LC1 reach LC3, the main frequency range of the vertical bending moment gradually shifts to the left of the coordinate axis, which is caused by the gradual decrease of the main interval of wave spectral energy with the gradual deterioration of working conditions.

Figure 5-25 shows the standard deviation of the vertical moment and the extreme value of the load for different cross-sections under LC3 considering the influence of diffracted and radiated waves. For the standard deviation and load extremum of the vertical bending moment of the cross-section, from the bow to the stern, there is a trend of "first increasing and then decreasing". Moreover, considering the net load, the vertical bending moment of the cross-section will be increased to a certain extent, but the net load has little influence on the bending moment of some cross-sections, and even the bending moment of the cross-section decreases to a certain extent. The influence of diffracted and radiated waves also has very little influence on the bending moments of the individual cross-sections, with the largest standard deviation change of bending moment at cross-section S4 increasing by only about 1.4%, and the extreme value of the load changing by less than 3%. This also verifies from another side that the influence of the disturbance of the floating body on the whole velocity field is local, and will not change the distribution of the wave field velocity as a whole.



(a) LC1

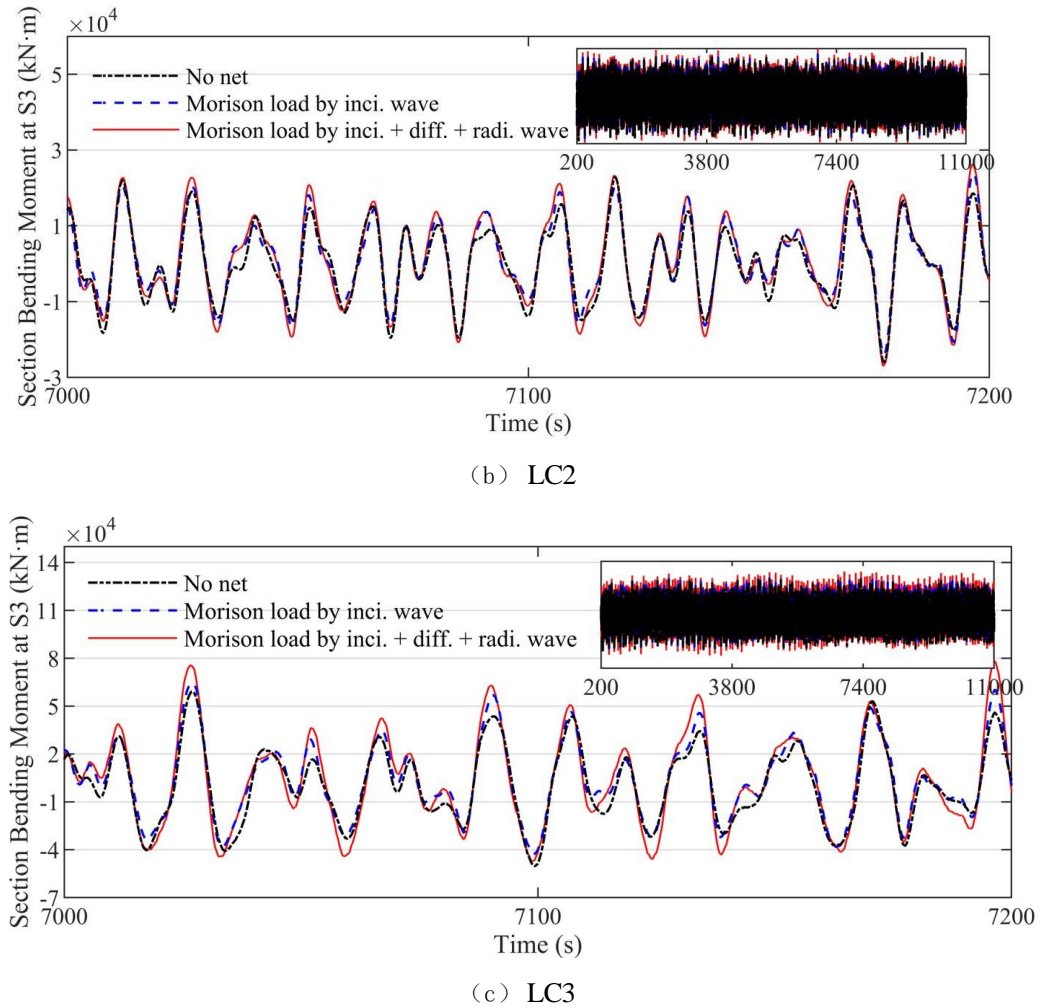
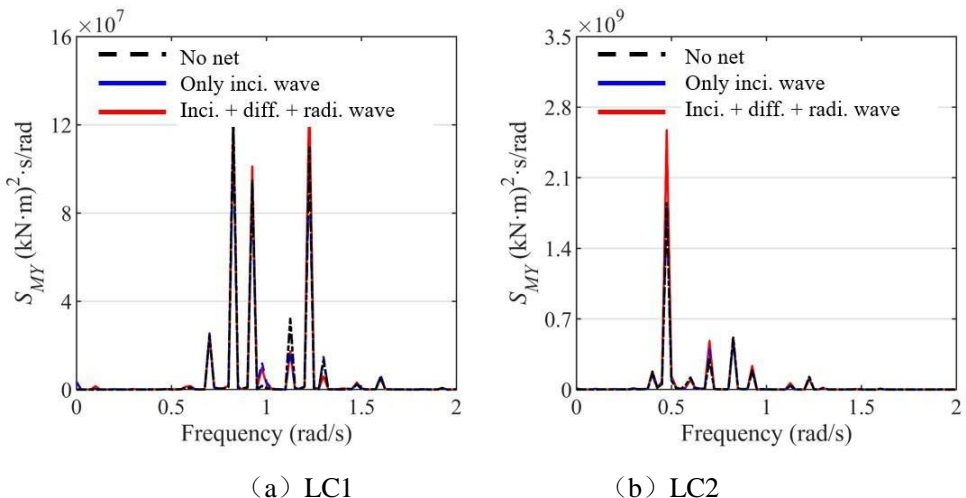
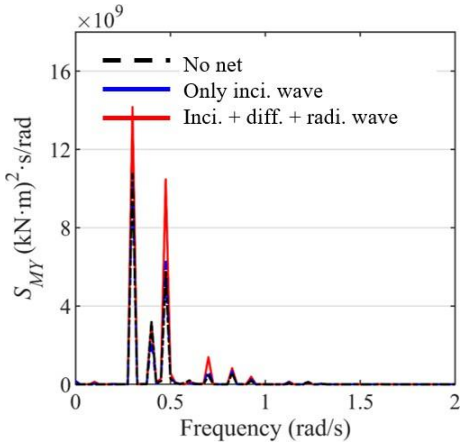


Figure 5-23 Vertical moment history of cross-section S3 under different operating conditions  
Fig. 5-23 The time history of vertical bending moment at S3 under different load cases

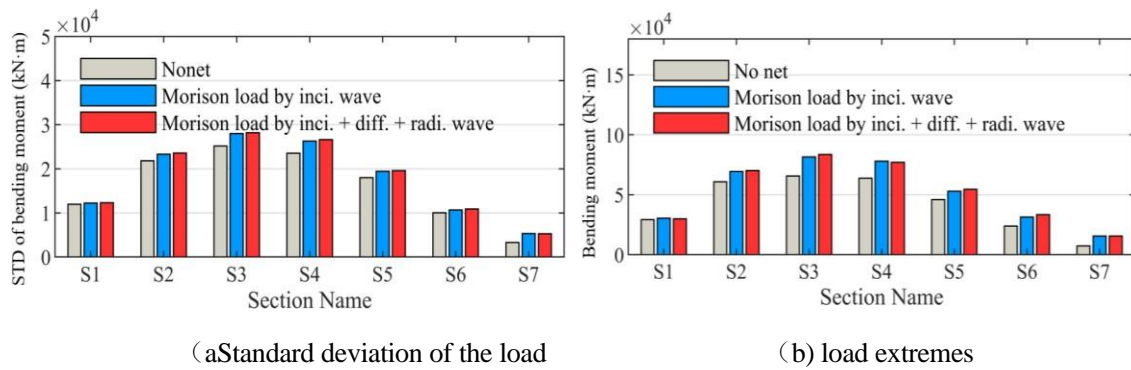




(c) LC3

Figure 5-24 Vertical moment spectral density curves of cross-section S3 under different operating conditions

Fig. 5-24 The spectral density of vertical bending moment at S3 under different condition cases



(a) Standard deviation of the load

(b) load extremes

Figure 5-25 LC3 takes into account the standard deviation and extreme values of the vertical moment for different cross-sections affected by diffracted and radiated waves

Fig. 5-25 The standard deviation and the estimated extreme of vertical bending moment under LC3 considering diffraction and radiation waves

## 5.6.2 Analysis of the influence of shear forces on cross-sections

fig 5-26 It is a cross-section under different working conditions S5 vertical shear time of ,fig 5-27 It is a cross-section under different working conditions S5 The vertical shear spectral density curve of . With the gradual deterioration of the working conditions, the cross-section S5 The vertical shear force gradually increases. When the net load is not considered, the vertical shear force is positively offset to the ordinate axis as a whole, which can be considered as the net load in *The role in the Z direction is mainly vertical sea facing downward. However, the influence of the presence of mesh load on the cross-section shear force is still relatively small. When taking into account the net load, diffracted waves and radiation are taken into account* The cross-sectional shear force under the influence of the wave is almost the same as the result considering only the action of the incident wave, and the same conclusion can be drawn in the spectral density results.

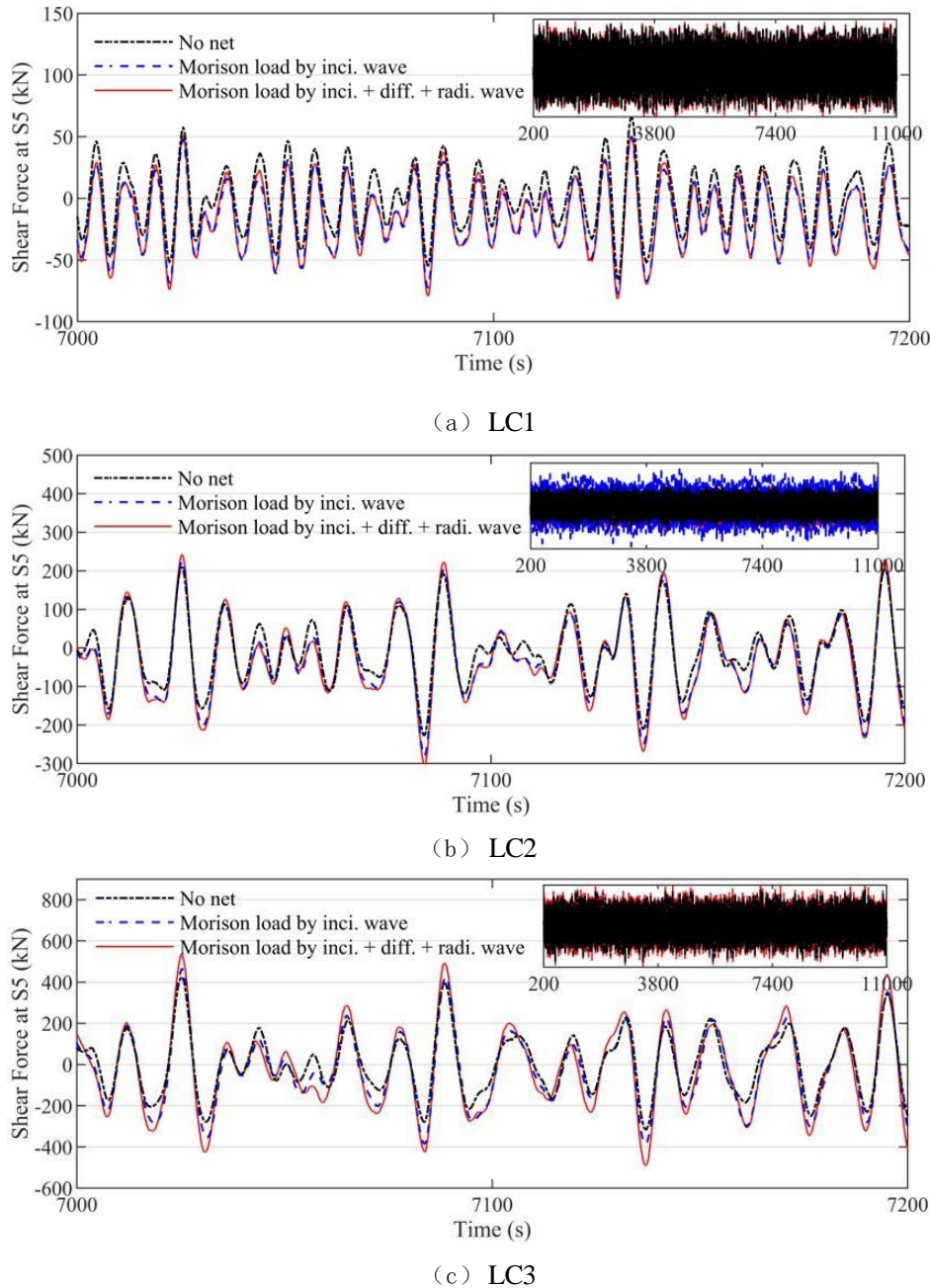


Figure 5-26 Vertical shear force history of cross-section S5 under different operating conditions

Fig. 5-26 The time history of vertical shear force at S5 under different load cases

Figure 5-28 shows the standard deviations and extrema of the vertical shear forces for different cross-sections under LC3 considering the effects of diffracted and radiated waves. For the standard deviation and load extremum of the cross-sectional shear force, from the bow to the stern, there is a trend of "first decreasing, then increasing and then decreasing". On the whole, considering the net load, the extreme value of the cross-section shear force will be increased to a certain extent, but the change range is relatively small. The presence of diffracted and radiated waves has a relatively obvious effect on individual cross-sections, but is basically the same or slightly larger than the cross-sectional shear force value that only considers the

influence of the incident wave, and the degree of influence is similar to the result of the vertical bending moment of the cross-section. This also shows that the net load changed by the buoyancy disturbance has no obvious effect on the cross-sectional shear force.

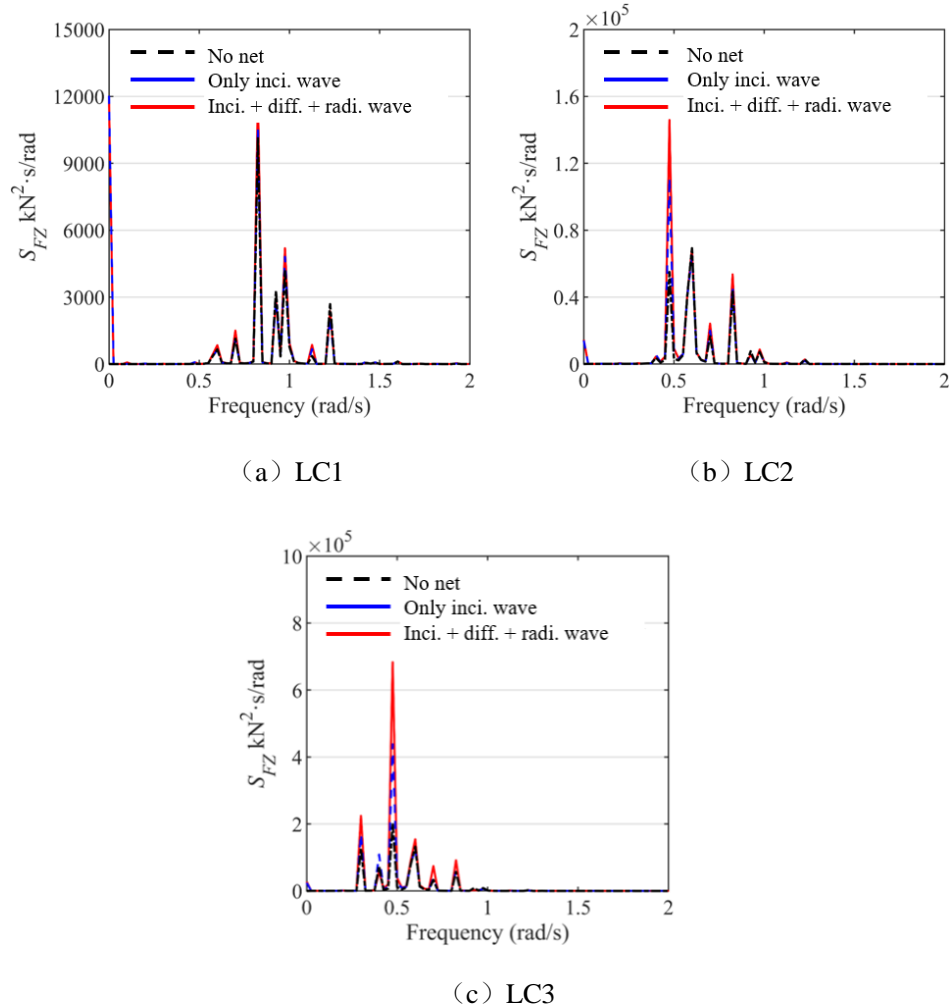
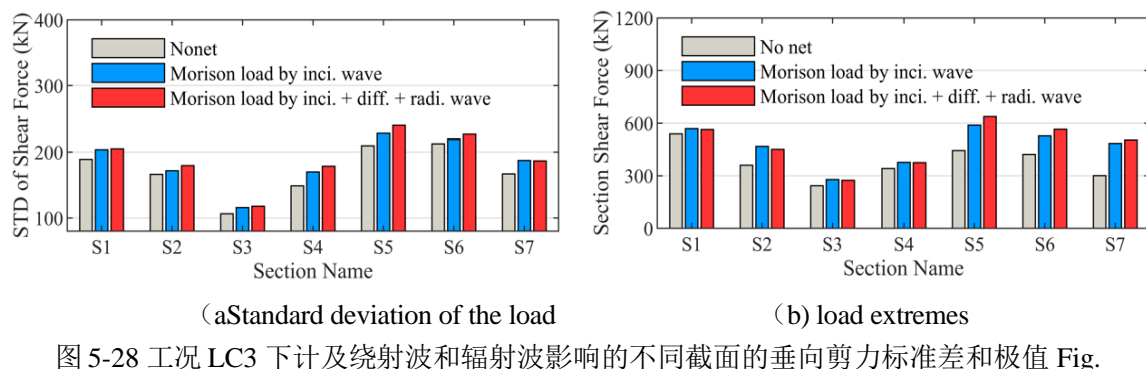


Figure 5-27 Vertical shear spectral density curves of cross-section S5 under different operating conditions

Fig. 5-27 The spectral density of vertical shear force at S5 under different condition cases



5-28 The standard deviation and the estimated extreme of vertical shear force under LC3

Fig. 18 The standard deviation and the estimated extreme of vertical shear force under ECE considering diffraction and radiation waves

## 5.7 Summary of this chapter

This chapter proposes a dynamic response analysis method for large cages considering the influence of disturbed wave fields under irregular waves

The statistical results of the response of the network cable tension, the connector bearing, and the cross-sectional load of the main steel structure of the net jacket were analyzed. Firstly, the coupling effect between the movement of the cage buoy, the disturbed wave field and the hydrodynamic load of the cage under irregular waves is considered, and the state-space method is used to simulate the radiative load related to the movement frequency in the time domain, and then the overall motion response of the large cage under the action of irregular waves is calculated. The perturbation wave field affected by diffraction wave and radiated wave is obtained by the overall motion response and velocity transfer function of the cage, and the hydrodynamic load of slender structures such as steel frame and net coat is calculated by Morrison's formula, and finally the above-mentioned coupling effect under irregular waves is realized by numerical iteration. The main big conclusions are as follows:

(1) Therefore, when the influence of the disturbance wave field on the net coat is considered, the overall motion response of the cage and the cross-sectional load of the main steel structure do not change obviously, that is, the influence of diffraction wave and radiated wave can be ignored when the motion response of the cage and the cross-sectional strength of the main steel structure are checked.

(2) The maximum cable tension is located at the edge of the mesh surface of the side nets perpendicular to the wave direction, and the disturbance wave field has a significant effect on the cable tension at these locations. This is due to the fact that although the hydrodynamic force of the net coat will not produce great changes as a whole, the influence of the local position on the force of the net coat is still very significant. Under different wave conditions, the effects of diffracted and radiated waves result in an increase of 12%, 27% and 49% in maximum cable tension, respectively. Therefore, in the structural safety assessment of the mesh system, the impact of the disturbed wave field should be studied in depth.

(3) Since the load acting on the connector is transmitted through the hydrodynamic load of the net, the diffracted wave and radiated wave also have a certain influence on the load of the connector. In this paper, the maximum load increases by 15%, 18% and 36% respectively under different working conditions, but the increase is smaller than the increase of net tension.

## Chapter 6: An analysis of the water elastic response of large cages considering the effects of perturbation wave fields on netting

### 6.1 introduction

With the continuous development of the marine aquaculture industry in recent decades, the amount of single cages in marine aquaculture cages has become more and more numerous and larger<sup>[155]</sup>. Especially in the past decade, various new forms of large-scale cage structures have emerged one after another. The length of the floating body is nearly 400 meters, and the height is only about 20 meters, and the elastic deformation in the wave is obvious, and the deformation is mainly in the vertical bending mode, so it is very necessary to study the hydroelastic response.

Hydroelasticity has evolved from two-dimensional water elasticity<sup>[156, 157]</sup> to three-dimensional water elasticity<sup>[158, 159]</sup>, and linear water elasticity<sup>[160-162]</sup> to nonlinear water elasticity<sup>[162-165]</sup>. The coupling effects of hydrodynamic, elastic, and inertial forces are considered in the response analysis of offshore structures<sup>[166]</sup>. The theory of water elasticity has been widely applied in the structural design of large ships and large buoys<sup>[167]</sup>. Among them, the two-dimensional water elasticity theory is based on the slice theory, ignoring the mutual interference of fluids in the axial direction of the structure, and is not suitable for the study of water elasticity of multihull ships and large-opening ships. Wu<sup>[159]</sup> pioneered the development of a three-dimensional linear hydroelastic frequency-domain analysis theory, which combines structural dynamics and three-dimensional seaworthiness theory, and is suitable for the water elasticity problem of arbitrarily shaped structures in waves. The three-dimensional frequency domain water elasticity theory has been widely used<sup>[167, 168]</sup>, and the modal superposition method and the direct solution method are usually used, but it is mainly applicable to steady-state processes. The traditional theory of water elasticity analysis is mostly based on modal superposition technology, which cannot consider the force of the net with strong nonlinear characteristics, let alone the influence of the wave field after the disturbance of the structure on the net coat. The theory of water elasticity in the time domain includes the direct time integration method and the Fourier transform method based on the Cummins equation<sup>[169]</sup>, the former is suitable for strong nonlinear problems but the computational efficiency is very low<sup>[142]</sup>, and the latter is suitable for solving weak nonlinear water elasticity problems on the basis of ensuring computational efficiency<sup>[170]</sup>。 Based on the three-dimensional linear hydroelastic frequency domain theory, Chen<sup>[171]</sup> studied the response of large ocean structures in waves, and found that the resonance of the structures is obvious under the action of regular waves with similar wave

periods to the intrinsic period of the structure. Kyoung et al.<sup>[172]</sup> developed a time-domain numerical method for considering fully nonlinear free surface conditions using a finite element method based on the variational principle. Wang Dayun<sup>[173]</sup> established a three-dimensional hydroelastic time-domain analysis method that directly analyzes the hydrodynamic load and hydroelastic response of ships in the time domain, based on the same basic physical assumptions as the three-dimensional hydroelastic frequency domain analysis method. Based on the three-dimensional potential flow theory and the modal superposition method, Wang Qibin et al.<sup>[174]</sup> proposed a three-dimensional time-domain nonlinear elastic analysis method that can be used for oblique waves and different velocities based on the Rankine source method, and compared it with the experimental results. Based on the frequency domain analysis of multi-floats and the Cummins equation<sup>[136]</sup>, Wei et al.<sup>[142, 166]</sup> established a water elastic model of large floating bodies by discretizing them into a multi-module system connected by equivalent elastic beams, and developed a time-domain water elasticity analysis method suitable for inhomogeneous wave fields. Li<sup>[175]</sup> combined multi-body hydrodynamics and concentrated mass method to establish a large-scale floating base and fan structure.

The coupled time-domain water elasticity model analyzes the power generation fluctuation under the hydroelastic response of the large floating base, and finds that the hydroelastic deformation of the floating body will cause the instability of the wind turbine.

In this project, the time-domain water elasticity method of cage buoys is as follows: firstly, based on the discrete water elasticity theory of the floats, the continuous buoys are discretized into a multi-module system, and then the potential flow theory is used to solve the wave load of the multi-module system. The equivalent structure model of the buoys is established by the elastic beams connecting the modules, and the hydroelastic response of the multi-module buoys is solved in the time domain based on the state-space method.

In fact, it is not only large offshore structures that exhibit a hydroelastic response. Finer and softer structures also exhibit significant hydroelastic response in waves. For example, the floating ring, net coat and other structures of traditional gravity cages. As a typical cross-scale marine structure, the study of the water elasticity of the net coating system and steel frame structure of large cages is also an important part of the study of water elasticity of cages. The steel frame structure is used for the structural reinforcement and support of large cages, the length-diameter ratio is generally large, and it is a typical slender structure, which will occur to a certain extent of elastic deformation in the marine environment, but the degree of deformation is relatively limited, and its hydrodynamic load can be calculated by Morrison's formula. The flexible deformation of the net structure in the marine environment is more significant, and the Morrison model is used to simulate it, and the hydrodynamic load can also be calculated by the Morrison formula. In other words, the range of water elasticity of the cage in this paper includes three parts: the water elasticity of the floating body, the water elasticity of the steel frame and the water elasticity of the net coat (in fact, the water elasticity of the mooring system is also included in the calculation of this paper, but it is not included because the mooring system is not the focus of this paper). Since the water elasticity analysis of steel frames and nets can be carried out based on the current numerical software, and the calculation process is relatively simple without the need to compile their own calculation programs, the water elasticity research in this chapter is mainly aimed at the floating bodies of large cages.

In this chapter, based on the hydroelastic analysis method of equivalent beams connected to multiple rigid bodies, an analysis method for the hydroelastic response of large cages considering the influence of disturbance wave field is proposed. Firstly, the continuous buoy is discretized into a multi-module system, and then the first-order wave excitation force transfer function, hydrodynamic coefficient and velocity field transfer function of the multi-module system are solved by using the three-dimensional potential flow theory, and then the equivalent buoy structure model of the buoy is established through the equivalent elastic beam connection between the buoy modules, and the motion response of the multi-module buoy in the time domain is solved by using the state space method. The hydrodynamic load of the mesh and steel frame structure is calculated by Morrison's formula, and the load of the

mesh and steel frame is transferred by coupling the motion constraint with the equivalent elastic beam model. Finally, the disturbance wave field after the equilibrium of the equivalent float motion and the hydrodynamic load of the net coat is obtained by iterative calculation, and the hydroelastic response of the large cage is obtained, and the motion deformation and cross-sectional load characteristics of the cage are analyzed.

## **6.2 Hydroelastic analysis theory of large cage based on the method of equivalent beams connecting multiple rigid body modules**

Therefore, based on the hydrodynamics and potential flow theory of multi-floats, the large floats are discretized into several rigid floats, a multi-module system is constructed, and the hydrodynamic calculations are carried out in the frequency domain. As shown in Figure 6-1 , a local motion coordinate system is set for each module, and the first-order wave excitation force transfer function, additional mass, wave damping coefficient and velocity field transmission of each buoy module are calculated by WAMIT

Recursive functions. In the frequency domain, the motion response equation for a multi-module system can be written as:

$$\begin{aligned}
 & \left[ \begin{array}{c|c} M^{(1)} & \\ \hline -\omega_2 & \end{array} \right] \cdot \cdot \cdot \left[ \begin{array}{c|c} A^{(11)} & \\ \hline + & \end{array} \right] \cdot \cdot \cdot \left[ \begin{array}{c|c} A^{(IM)} & \\ \hline \vdots & \end{array} \right] \left[ \begin{array}{c|c} \text{in} & \\ \hline \text{the}^{(1)} & \end{array} \right] \\
 & \left[ \begin{array}{c|c} M^{(M)} & \\ \hline A^{(M1)} & \end{array} \right] \cdot \cdot \cdot \left[ \begin{array}{c|c} A^{(MM)} & \\ \hline \vdots & \end{array} \right] \left[ \begin{array}{c|c} v^{(M)} & \\ \hline v & \end{array} \right] \\
 & \left[ \begin{array}{c|c} C^{(11)} & \\ \hline -i\phi & \end{array} \right] \cdot \cdot \cdot \left[ \begin{array}{c|c} C^{(IM)} & \\ \hline \vdots & \end{array} \right] \left[ \begin{array}{c|c} \text{in} & \\ \hline \text{the}^{(1)} & \end{array} \right] \left[ \begin{array}{c|c} F^{(1)} & \\ \hline + & \end{array} \right] \\
 & \left[ \begin{array}{c|c} C^{(M1)} & \\ \hline C^{(MM)} & \end{array} \right] \left[ \begin{array}{c|c} v^{(N)} & \\ \hline v & \end{array} \right] \cdot \cdot \cdot \left[ \begin{array}{c|c} K^{(1)} & \\ \hline \vdots & \end{array} \right] \left[ \begin{array}{c|c} \text{in} & \\ \hline \text{the}^{(1)} & \end{array} \right] \\
 & \left[ \begin{array}{c|c} K^{(M)} & \\ \hline v^{(M)} & \end{array} \right] \left[ \begin{array}{c|c} \Phi^{(M)} & \\ \hline \Phi & \end{array} \right]
 \end{aligned} \tag{6-1}$$

where  $\omega$  is the wave frequency,  $N$  is the number of modules in a multi-module system, and  $M^{(m)}$  and  $K_{(m)}$  are the firsts, respectively  $n$  modules

( $m = 1, \dots, m$ ) and hydrostatic recovery matrix.  $\mathbf{A}^{(nm)}$  and  $\mathbf{C}^{(nm)}$  respectively represent the motion of the  $m$ th module in the  $n$ th module ( $n, m = 1, \dots, M$ ).  $\mathbf{M}^{(m)}, \mathbf{K}^{(m)}, \mathbf{A}^{(nm)}$  and  $\mathbf{C}^{(nm)}$  are  $6 \times 6$ th order matrices.  $\mathbf{F}^{(m)}$  and  $\mathbf{u}^{(m)}$  are the  $m$ th modules respectively ( $m = 1, \dots, M$ ) is a first-order wave excitation force and displacement, both of which are  $6 \times 1$  vectors in complex form. The symbol " $\text{In}$ " indicates a parameter in the frequency domain. Since the continuous float is discretized into  $M$  rigid body modules, the number of degrees of freedom in a multi-module system is  $6M$ .

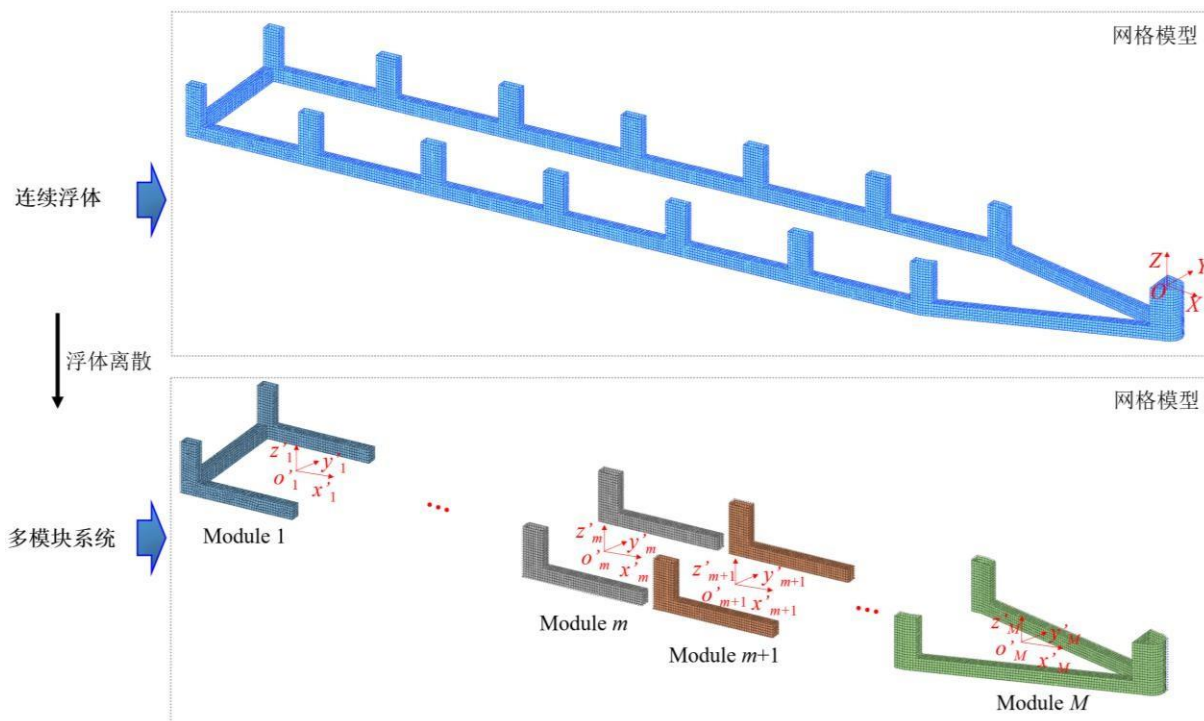


Figure 6-1 Motion coordinate system of a multi-module system

Fig. 6-1 Coordinate system of multi-modules system

For simplicity's sake, Eq. (6-1) can be rewritten as:

$$[-\omega^2(\mathbf{M} + \mathbf{A}) - i\omega\mathbf{C} + \mathbf{K}] \mathbf{u} = \mathbf{F}_{in} \quad (6-2)$$

where  $\mathbf{M}$  and  $\mathbf{K}$  represent the mass matrix and hydrostatic recovery stiffness matrix of the multi-module system, respectively, and  $\mathbf{A}$  and  $\mathbf{C}$  represent the additional mass matrix and damping coefficient matrix of the multi-module system,  $\mathbf{FW}$  and  $\mathbf{C}$ , respectively  $\mathbf{u}$  denotes the first-order wave excitation force and motion displacement of the multi-module system in the frequency domain.

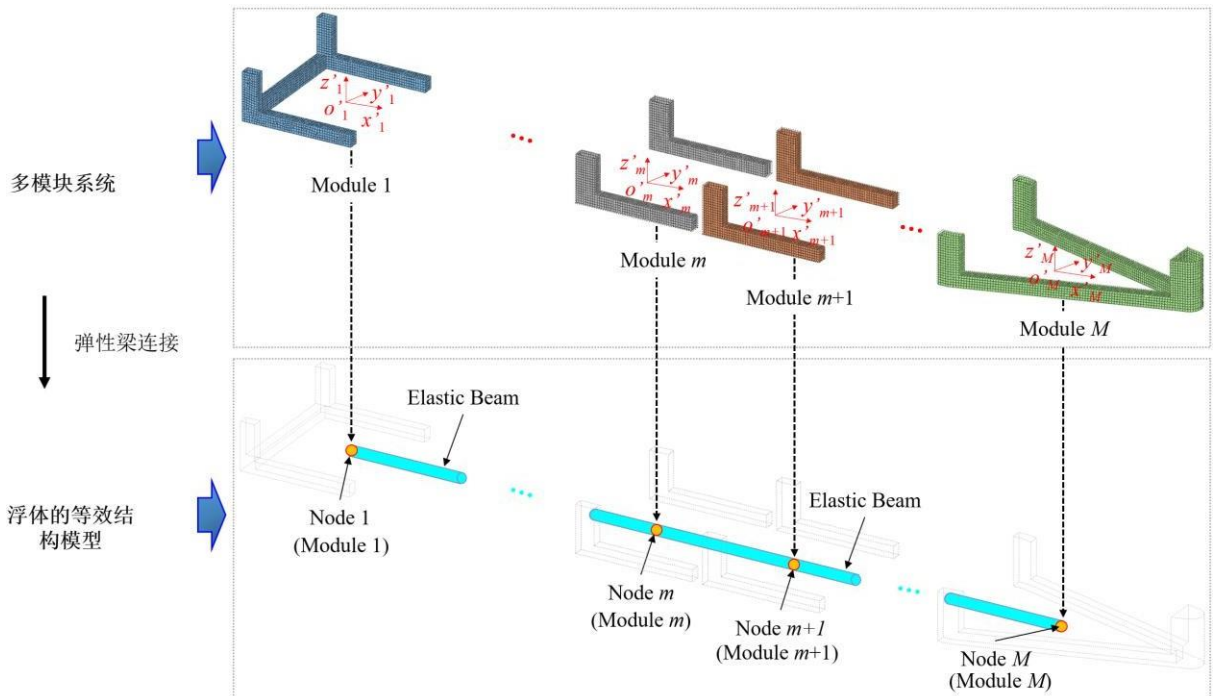


Figure 6-2 Equivalent structure model of the floating body  
Fig. 6-2 Equivalent elastic model of the floating body

In a multi-module system, the modules are discrete from each other. Because the actual large-scale floating body is a continuous structure, and there is structural stiffness between the modules, the cross-sectional stiffness of the actual floating body is simulated by connecting each module by the equivalent elastic beam, and the equivalent beam structure model of the large-scale floating body is established, as shown in Figure 6-2 . Under regular waves, the equation of motion of the equivalent structure model of the floating body in the time domain when considering the structural stiffness can be written as:

$$\begin{cases} | (\mathbf{M} + \mathbf{A})\mathbf{u}(t) + \mathbf{Cu}(t) + (\mathbf{K} + \mathbf{K}_S)\mathbf{u}(t) = \mathbf{FW}(t) \\ | \Phi\Omega(t) = \begin{bmatrix} (1) & (2) & \cdots & (N) \end{bmatrix}^T \end{cases} \quad (6-3)$$

where  $\mathbf{KS}$  is the stiffness matrix of the equivalent model of the buoy, and  $\mathbf{FW}(t)$  is the first-order wave excitation force acting on the buoy in the time domain,  $\mathbf{F}\square\mathbf{m}^l(t)$  is the *first-order wave excitation force* acting on the  $m$  block ( $m = 1, \dots, m$ ), which is a vector of  $6 \times 1$  order and can be obtained by Eq. (6-1).  $\mathbf{F}\square\mathbf{m}^l$  OK.  $\mathbf{u}(t)$ ,  $\mathbf{u}(t)$  and  $\mathbf{u}(t)$ . Represent the displacement, velocity, and acceleration of a multi-module system in the time domain, respectively.

Based on the state-space method<sup>[101, 138, 139]</sup>, the equation of motion of the equivalent structure model of the floating body in the time domain considering the structural stiffness under irregular waves can be written as:

$$(\mathbf{M} + \mathbf{A}(\infty))\ddot{\mathbf{u}}(t) + (\mathbf{K} + \mathbf{K}_S)\mathbf{u}(t) + \mathbf{z}\mathbf{R}\mathbf{a}\mathbf{d}(t) = \mathbf{F}\mathbf{W}(t) \quad (6-4)$$

where  $\mathbf{A}(\infty)$  is the additional mass at infinite frequencies, and  $\mathbf{zRad}(t)$  is the frequency-dependent radiated load term of the multi-module system, which can be obtained by fitting the frequency-dependent additional mass and wave damping.

The process of calculating the radiation load of a multi-module system is mainly divided into the following two steps:

1. Data fitting: The additional mass and wave damping of the multi-module system at different frequencies obtained by frequency domain analysis are obtained by least-squares fitting to obtain the ordinary matrices of  $D$ ,  $E$  and  $Q$  at each position (a total of  $6M \times 6M$  positions). The coefficients of the integral equation  $q_i$  and  $p_j$  ( $i = 0, \dots, a-1; j = 0, \dots, b$ ;  $a$  is the order of the higher-order ordinary differential equations,  $a = b + 1$ ) thus yielding the intermediate matrices  $D$ ,  $E$ , and of the state-space method at all positions  $Q$ .

2. Programming: According to Eq. (6-16), the subroutine UEL in ABAQUS is used for software secondary development, and the load related to the infinite frequency additional mass term is taken into account to establish a new unit with  $6M$  degrees of freedom. Implements the calculation of the radiation load, the element has  $M$  nodes with the initial coordinates of the nodes at the centroid of each module.

### (3) Equivalent beam stiffness of the floating body

In this chapter, equivalent beams are used to simulate actual continuous elastic floats. In order to ensure that the response of the equivalent beam is consistent with the response of the actual floating body, the structural parameters of the elastic beam need to be set as follows [176].

$$\begin{cases} E_e A_e = E_f A_f \\ E_e I_{MY-e} = E_f I_{MY-f} \\ E_e I_{IMZ-E} = E_f I_{IMZ-f} \\ G_e I_{p-e} = G_f I_{p-f} \end{cases} \quad (6-5)$$

where  $E$ ,  $G$ ,  $A$ ,  $IMY$ ,  $IMZ$ , and  $I_p$  denote the elastic modulus, shear modulus, cross-sectional area, and winding of the buoy, respectively. Section moment of inertia on the Y axis, section moment of inertia around the Z axis, and torsional moment of inertia on the section.  $EA$ ,  $EIMY$ ,  $EIMZ$  and  $GI_p$  represent the axial stiffness, vertical bending stiffness, transverse bending stiffness and torsional stiffness of the float cross-section, respectively. The subscripts "e" and "f" represent the parameters corresponding to the equivalent structural beam and the continuous elastic float, respectively. In the actual calculation, the influence of the slender steel frame structure on each parameter can be considered in the parameter calculation process of the equivalent structural beam, so as to simplify the calculation process and improve the calculation efficiency.

In the equivalent process, the determination of the torsional equivalent stiffness is carried out numerically. For several other parameters that require equivalence, dividing each section



$$\left\{ \begin{array}{l} And_{\text{and}}^k Ae = \sum_{i=1}^k And_f A_f i \\ I' \quad m \text{ a writer} (\quad I'm \text{ a writer}) \\ AND_{\text{tMZ-E}} = \sum_{i=1}^k And_f (I + A_f h_{Zi}^2) \end{array} \right. \quad (6-6)$$

where  $A_f i$  is the cross-sectional area of the  $i$ -th sub-section, and  $IMY_i$  and  $IMZ_i$  are the vertical and transverse moments of inertia of the  $i$ -th sub-section, respectively.  $h_{Yi}$  is the vertical distance between the centroid of the cross-sectional area of the  $i$ -th sub-section and the Y-axis of the entire cross-section, and  $h_{Zi}$  is the centroid of the cross-sectional area of the  $i$ -th sub-section with the entire cross-section Z. The vertical spacing of the axes.

As shown in Figure 6-2, after the continuous float is discretized into a multi-module system, the continuity of the elastic deformation of the float is ensured due to the limitation of the elastic beams between the modules. Combined with the axial, bending, and torsional stiffness of the floating body cross-section, the element stiffness of the equivalent elastic beam is reconstructed, and the element stiffness matrix  $k(m)$  of the  $m$ th equivalent beam element can be expressed as [166]:

$$\mathbf{k}^{(m)} = \begin{bmatrix} \mathbf{k}_{m,m}^{(m)} & \mathbf{k}_{m,m \square 1}^{(m)} \\ \mathbf{k}_{m \square 1,m}^{(m)} & \mathbf{k}_{m+1,m \square 1}^{(m)} \end{bmatrix} \quad (6-7)$$

where  $\mathbf{k}_{n,m}^{(q)}$  is a  $6 \times 6$ th order matrix composed of the parameters in Eq. (6-5), with the superscript " $(q)$ " denotes the element number of the equivalent elastic beam ( $q = 1, 2, \dots, M-1$ ") indicates the first element node of the  $q$ th equivalent elastic beam element, and the subscript ".  $m$ " denotes the second element node of the  $q$ th equivalent elastic beam element, where  $n, m = 1, 2, \dots, M$ .

The external loads on each module act on the nodes of the equivalent elastic beam model of the floating body (these are the nodes of the custom elements above), then the structural stiffness matrix between the modules in Eq. (6-3) and Eq. (6-4) can be expressed as:

$$\mathbf{K}_S = \begin{bmatrix} \mathbf{k}_{1,1}^{(1)} & & & & & \\ & \ddots & & & & \\ & & \mathbf{k}_{m,m}^{(m \square 1)} + \mathbf{k}_{m,m}^{(m)} & \mathbf{k}_{m,m \square 1}^{(m)} & & \\ & & \mathbf{k}_{m \square 1,m}^{(m)} & \mathbf{k}_{1,m \square 1}^{(m)} + \mathbf{k}_{1,m \square 1}^{(m \square 1)} & & \\ & & & & \ddots & \\ & & & & & \mathbf{k}_{M,M}^{(M-1)} \end{bmatrix} \quad (6-8)$$

where  $\mathbf{k}_{m,m}^{(m)}$  is the  $6 \times 6$ th order sub-stiffness matrix between the  $m$ -module and the  $m+1$  module, determined by the parameters of the equivalent elastic beam.

### 6.3 A method for analyzing wave fields under multi-body perturbations

When large floats are discretized, diffracted and radiated waves are generated from each

module. Since the diffraction wave is to move the floating body

Generated under the incident wave when fixed in the equilibrium position, and the discrete multi-module system is essentially the same as the continuous buoy, so the diffracted wave of the continuous buoyancy can be used instead of the diffracted wave of the multi-module system. For the discrete  $m$ th *float module*, the transfer function of the radiation wave velocity field at *wave frequency*  $\omega_l$  can be obtained by frequency domain analysis, and the water quality point velocity generated by the radiation wave at various spatial points is determined according to the motion of each module in each degree of freedom. Under the incident wave with a regular wave frequency  $\omega_l$  and amplitude  $|vI_l|$ , taking into account the influence of the radiated wave generated by the multi-module system and the diffracted wave generated by the buoy, the water quality point velocity  $v_l$  in the velocity field can be expressed as:

$$\begin{aligned}
 v_l &= v_{II} + v_{DI} + v_{fl} \\
 &= |vI_l| \left[ v_{RI_1}^T + v_{RI_2}^T + v_{RI_3}^T \right] + |vD_l| \left[ v_{DI_1}^T + v_{DI_2}^T + v_{DI_3}^T \right] \\
 &= \left| \zeta_{ToTF1} |vI_l| \cos(\omega_l t + \theta_{II}^l) \right| + \left| \zeta_{ToTF2} |vI_l| \cos(\omega_l t + \theta_{II}^l) \right| + \left| \zeta_{ToTF3} |vI_l| \cos(\omega_l t + \theta_{II}^l) \right| \\
 &\quad + \left| \zeta_{ToTF1} |vD_l| \cos(\omega_l t + \theta_{DI}^l) \right| + \left| \zeta_{ToTF2} |vD_l| \cos(\omega_l t + \theta_{DI}^l) \right| + \left| \zeta_{ToTF3} |vD_l| \cos(\omega_l t + \theta_{DI}^l) \right| \\
 &\quad + \left| \sum_{\mu=1}^{M-6} \sum_{j=1}^{(m)-\lambda} \Phi_{TFj}^{(m)R-\lambda} \cos(\omega_l t + \theta_{RI}^l + \delta_j) \right| \\
 &\quad + \left| \sum_{\mu=1}^{M-6} \sum_{j=1}^{(m)-\lambda} \Phi_{TFj}^{(m)R-\lambda} \cos(\omega_l t + \theta_{DI}^l + \delta_{(m)-\lambda}) \right| \\
 &\quad + \left| \sum_{\mu=1}^{M-6} \sum_{j=1}^{(m)-\lambda} \Phi_{TFj}^{(m)R-\lambda} \cos(\omega_l t + \theta_{RI}^l + \delta_{(m)-\lambda}) \right|
 \end{aligned} \tag{6-9}$$

where  $l$  is the ordinal number of the regular wave,  $\omega_l$  is the wave frequency of the regular wave with the ordinal number  $l$ ,  $\alpha\delta$   $\zeta_{AI}$  is the wave frequency of the regular wave

$\Phi$  The corresponding regular wave amplitude,  $vI_l$  and  $vD_l$  are respectively represented in  $k$  ( $k = X, Y, Z$ ) direction of the incident wave, around

The amplitude of the radio velocity transfer function,  $v^{(m)R-\lambda}$  is the  $j$ -th degree of freedom of the  $m$ -th module of a *multi-module system*

( $j = 1, 2, \dots, 6$ ) 上的运动在  $k$  ( $k = X, Y, Z$ ) 方向产生的辐射波速度传递函数的幅值,

Symbols "||" indicates the amplitude of the parameter,  $N$  represents the number of modules of the multi-module system,  $\lambda$  indicates in

$k$  ( $k = X, Y, Z$ ) 方向的入射波、绕射波和辐射波速度传递函数与波面之间的相位角,

$\theta_{Rkj}^{(m)-\lambda}$  δενοτεσ της μοτιον οφ της mth module of a *multi-module system* in its j-th degrees of freedom ( $j = 1, 2, \dots, 6$ ).

$k(k = X, Y, Z)$  方向产生的辐射波速度传递函数与波面升高之间的相位角,  $\mathbf{v}_{RI}$ ,  $\mathbf{v}_{DI}$ ,

$\mathbf{v}_{RI}$  denotes the point velocity of the water quality generated by the incident, diffracted, and radiated waves, respectively, and the subscripts I, D, and R represent the parameters corresponding to the incidence, diffraction, and radiated waves, respectively.  $u^{(m)-\lambda}$  and  $\square^{(m)-\lambda}$  represent the m-th module of a multi-module system, respectively

The amplitude of motion and the phase angle of motion of the block in j degrees of freedom ( $j = 1, 2, \dots, 6$ ).

Based on the linear superposition theory, the water quality points of the wave field under irregular waves are considered for incident waves, diffracted waves and radiation waves

Velocity can be expressed as:

$$\begin{aligned}
 \mathbf{v}^{\text{irre}} &= \sum_{l=1}^N \boldsymbol{\omega}_l \\
 \mathbf{vI} &= \mathbf{vII} + \mathbf{vDI} + \mathbf{v}_{\text{fl}} \\
 &= \sum_{l=1}^N v_{\text{II}l} \mathbf{e}_2^T + v_{\text{III}l} \mathbf{e}_3^T + \sum_{l=1}^N \boldsymbol{\omega}_l \Delta \lambda l \mathbf{e}_1^T + v_{\text{DI}l} \mathbf{e}_2^T + v_{\text{DII}l} \mathbf{e}_3^T \\
 &+ \sum_{l=1}^N \boldsymbol{\omega}_l P \lambda l \mathbf{e}_1^T + v_{\text{RI}l} \mathbf{e}_2^T + v_{\text{RII}l} \mathbf{e}_3^T \\
 &= \left| \sum_{l=1}^N \zeta_{\text{TFI}l} |vI| l \cos(\omega_l t + \theta_{\text{II}l} + \epsilon_l) \right| \\
 &+ \left| \sum_{l=1}^N \zeta_{\text{TF2}l} |vI| l \cos(\omega_l t + \theta_{\text{II}l} + \epsilon_l) \right| \\
 &+ \left| \sum_{l=1}^N \zeta_{\text{TF3}l} |vI| l \cos(\omega_l t + \theta_{\text{II}l} + \epsilon_l) \right| \\
 &+ \left| \sum_{l=1}^N \zeta_{\text{TFI}l} |vD| l \cos(\omega_l t + \theta_{\text{DI}l} + \epsilon_l) \right| \\
 &+ \left| \sum_{l=1}^N \zeta_{\text{TF2}l} |vD| l \cos(\omega_l t + \theta_{\text{DI}l} + \epsilon_l) \right| \\
 &+ \left| \sum_{l=1}^N \zeta_{\text{TF3}l} |vD| l \cos(\omega_l t + \theta_{\text{DI}l} + \epsilon_l) \right| \\
 &+ \left| \sum_{\mu=1}^M \sum_{j=1}^{6\lambda} \bar{\alpha}_{\text{TFI}j}^{(m)-\lambda} \left| \bar{\alpha}_{\text{TFI}j}^{(m)\text{R}-\lambda} \cos(\omega_l t + \bar{\alpha}_{\text{RI}j}^{(m)-\lambda} + \delta_{\text{TFI}j}^{(m)-\lambda} + \epsilon_j) \right| \right| \\
 &+ \left| \sum_{\mu=1}^M \sum_{j=1}^{6\lambda} \bar{\alpha}_{\text{TF2}j}^{(m)-\lambda} \left| \bar{\alpha}_{\text{TF2}j}^{(m)\text{R}-\lambda} \cos(\omega_l t + \bar{\alpha}_{\text{R}2j}^{(m)-\lambda} + \delta_{\text{TF2}j}^{(m)-\lambda} + \epsilon_j) \right| \right| \\
 &+ \left| \sum_{\mu=1}^M \sum_{j=1}^{6\lambda} \bar{\alpha}_{\text{TF3}j}^{(m)-\lambda} \left| \bar{\alpha}_{\text{TF3}j}^{(m)\text{R}-\lambda} \cos(\omega_l t + \bar{\alpha}_{\text{R}3j}^{(m)-\lambda} + \delta_{\text{TF3}j}^{(m)-\lambda} + \epsilon_j) \right| \right|
 \end{aligned} \tag{6-10}$$

where  $\mathbf{v}_{\text{irre}}$  denotes the point velocity of the disturbed wave field under the irregular wave,  $N$  denotes the number of regular wave components constituting the irregular wave, and  $\epsilon_l$  is the random phase angle of the corresponding regular wave components at a wave frequency of  $\omega_l$ . The remaining parameters have the same meaning as the parameters above.

## 6.4 Water elasticity analysis method of large cages based on state space method

The continuous float body was discretized and simulated using an equivalent elastic beam, and the mesh was connected to the steel frame structure by a hinged connector. For large cages, the mesh and steel frame structures are connected to the boxes of the floating body. The nodes of the equivalent elastic beam elements are established with the corresponding steel frame nodes as the master-From constraints (Master-Slave constraint). The motion coupling of the steel frame system with the equivalent elastic beam establishes a water elastic analysis model of a large cage, such as fig 6-3 show. The cage is an axial symmetrical structure, with the equivalent elastic beams at the same height as the centroid of each module. Therefore, the mass parameters of the individual modules can be directly assigned to the corresponding

position of the elastic beam. When the effect of the net and the steel frame on the equivalent elastic beam is taken into account, the formula (6-4) It can be rewritten as:

$$\begin{cases} Mv(\tau) + KS_u(\tau) = F_{All}(\tau) \\ (\tau) = \Phi(\tau) + \Phi(t \square \square F(\tau)) + \Phi(t \square \square F \\ (\tau) + \Phi(t \square \square z(\tau) - K_v(\tau) - A(\infty)u \square t \square \\ \left. \begin{array}{l} \Phi^A \lambda \lambda \\ \Phi^S \end{array} \right\} \begin{array}{l} And \\ In \end{array} \quad \begin{array}{l} N \\ Line \end{array} \quad \begin{array}{l} I \\ G \\ B \end{array} \end{cases} \quad (6-11)$$

where  $\mathbf{M}$  and  $\mathbf{KS}$  are the mass matrix and the structural stiffness matrix of the equivalent structure, respectively, which are  $6N \times 6N$  order matrices.  $\mathbf{u} \square \mathbf{t} \square$  and  $\mathbf{u} \square \mathbf{t} \square$  represent the velocity and acceleration vectors of the equivalent structure, respectively,  $\mathbf{FAll}(\tau)$  is the external load on the large cage,  $\mathbf{FN}(\tau)$  is the component generated by the hydrodynamic load of the net coat, and  $\mathbf{FS} \square \mathbf{t} \square$  It is the component generated by the hydrodynamic load of the steel frame,  $\mathbf{FW}(\tau)$  represents the first-order wave excitation force on the buoy,  $\mathbf{FI}(\tau)$  is the inertial load generated by the steel frame structure, and  $\mathbf{FB}(\tau)$  is the hydrostatic buoyancy and  $\mathbf{FG}(\tau)$  is the structural gravity.  $\mathbf{FE}(t)$  denotes the external load to which the buoy is subjected, and  $\mathbf{zRad}(\tau)$  denotes the radiated load term that is only related to the wave frequency,  $\mathbf{Ku} \square \mathbf{t} \square$  and  $\mathbf{A}(\infty) \mathbf{u} \square \mathbf{t} \square$  denotes the inertial force load terms resulting from the hydrostatic recovery load and the infinity frequency additional mass, respectively, where  $\mathbf{K}$  and  $\mathbf{A}(\infty)$  is the hydrostatic recovery matrix and infinite frequency of a multi-module system

#### Additional Mass Matrix.

In the case of regular waves, the *first-order wave excitation force acting on the m module* ( $m = 1, \dots, M$ ) can be expressed in the time domain as:

$$\left\{ \begin{array}{l} \mathbf{F}_{(t)}^{(m)} = \left[ \Phi_{W_1}^{(m)}(t) \ F_{In_2}^{(m)}(t) \ \dots \ F_{W_6}^{(m)} \right] \\ \Phi_{W_j}^{(m)}(t) = \left| F^{(m)} \right| \cos(\omega_l t + \theta_{lj}^{(m)} - (k_l X \cos \varphi + k_l Y \sin \varphi)) \end{array} \right. \quad (6-12)$$

where  $F_{W_j}^{(m)}(t)$  is used in the  $j$  direction of the  $n$ th module ( $j = 1, 2, \dots, 6$ ). First-order wave excitation, down

The "l" mark indicates the ordinal number of the wave frequency  $\omega_l$ ,  $|F^{(n)}|$  and  $\theta^{(n)}$  represent  $F^{(n)}$ , respectively, of the transfer function amplitude and phase

$\angle \zeta_{Al}$  is the corresponding amplitude at the wave frequency  $\omega_l$ ,  $k_l$  is the corresponding wave number at the wave frequency  $\omega_l$ , and  $\varphi$  is the wave direction angle  
 $k_l X \cos \varphi + k_l Y \sin \varphi$  is position phase.

Irregular waves can be seen as the superposition of multiple regular wave components, so the first-order wave excitation force of the  $n$ th module of a multi-module system in the time domain can be expressed as:

$$\left\{ \begin{array}{l} \mathbf{F}_{In}^{(m)}(t) = \left[ \Phi_{W_1}^{(m)}(t) \ F_{In_2}^{(m)}(t) \ \dots \ F_{W_6}^{(m)}(t) \right]^T \\ \Phi_{W_j}^{(m)}(t) = \left| F^{(m)} \right| \cos(\omega_l t + \theta_{lj}^{(m)} + \varepsilon - (k_l X \cos \varphi + k_l Y \sin \varphi)) \end{array} \right. \quad (6-13)$$

where  $\mathbf{F}_{In}^{(m)}(t)$  is the wave excitation force of the  $m$  module, and  $N$  constitutes the number of regular wave components of the irregular wave, below

The mark "l" indicates the l-th regular wave component number ( $l = 1, 2, \dots, N$ ),  $\lambda$  denotes the l-th rule stochastic phase of the wave component,  $\zeta_{To the Yes l}$  amplitude of  $\sqrt{\text{regular wave}}$  components,  $\zeta_{To the} = 2S(\omega \lambda) \Delta \omega$ ,  $S$  is the wave-spectral density  $Doh$  Wave frequency interval of irregular waves.

The radiated load of a frequency-dependent multi-module system can be expressed in the frequency domain as:

$$\bar{\mathbf{zRad}}(\omega) = \mathbf{H}(\omega)\dot{\mathbf{u}}(\omega) \quad (6-14)$$

where  $\bar{\mathbf{zRad}}(\omega)$  is the frequency-domain expression of the radiated load of the frequency-dependent multi-module system, and  $\dot{\mathbf{u}}(\omega)$  is the frequency domain

, both of which are plural.  $\mathbf{H}(\omega)$  is the hydrodynamic transmission function

$\mathbf{H}(\omega) = i\Box m(\omega) + \mathbf{C}(\omega)$ . The number of degrees of freedom in a multi-module system is  $6M$ .

According to the Chinese equation (3-13) in Chapter 3, the frequency-dependent radiative load  $\mathbf{zRad}(t)$  of the multi-module system in the time domain can be obtained by performing the inverse Fourier transform *on Eq. (6-14)*, And expressed in the form of convolutional integrals:

$$\mathbf{zRad}(t) = \int_0^t \mathbf{h}(t-\tau) \mathbf{u}(\tau) d\tau \quad (6-15)$$

where  $\mathbf{h}(t)$  is the inverse Fourier transform of  $H(\omega)$ ,  $\mathbf{u}(\tau)$  Represents the velocity of a multi-module system in the time interval  $[0, t]$  and is a  $6N \times 1$  order vector.

Based on the state-space approach,  $\mathbf{zRad}(t)$  for multi-module systems can be written in the time domain as:

$$\left| \begin{array}{l} \text{with} \\ \zeta_{(m)}(t) = \begin{bmatrix} \text{Line} & \text{Line} & \text{Line} & \dots & \text{Line} \\ \text{with}^{(m)}(t) & \text{with}^{(m)}(t) & \text{with}^{(m)}(t) & & \text{with}^{(m)}(t) \\ \text{with}^{(m)}(t) & \text{with}^{(m)}(t) & \text{with}^{(m)}(t) & & \text{with}^{(m)}(t) \\ \text{with}^{(m)}(t) & \text{with}^{(m)}(t) & \text{with}^{(m)}(t) & & \text{with}^{(m)}(t) \\ \text{with}^{(m)}(t) & \text{with}^{(m)}(t) & \text{with}^{(m)}(t) & & \text{with}^{(m)}(t) \\ f_{ij}^{(m)}(t) = \sum_{j=1}^{6M} f^{(m)}(t), i = 1, 2, \dots, 6 \\ f_{ij}^{(m)}(t) = \mathbf{Q}\mathbf{X}(t), i = 1, 2, \dots, 6; j = 1, 2, \dots, 6M \\ \mathbf{X}(t) = \mathbf{D}\mathbf{X}(t) + \mathbf{E}\mathbf{u}^{(m)}(t), j = 1, 2, \dots, 6M \end{array} \right| \quad (6-16)$$

式中,  $\mathbf{z}_{(m)}(t)$  是第  $m$  个模块 ( $m = 1, 2, \dots, M$ ) 的与频率相关的辐射载荷,  $\zeta_{(m)}(t)$  是

The Line component of  $\mathbf{z}_{(m)}(t)$  in the  $i$ -direction ( $i = 1, 2, \dots, 6$ ),  $f_{ij}^{(m)}(t)$  is due to the multi-module system in the  $j$ th free Line Runs

The motion of the degree ( $j = 1, 2, \dots, 6M$ ) is the component of the  $i$ -th degree of freedom ( $i = 1, 2, \dots, 6$ ) of the  $m$  module,  $\mathbf{X}(t)$  is a state-space vector, and  $\mathbf{D}$ ,  $\mathbf{E}$ , and  $\mathbf{Q}$  represent intermediate matrices of state-space methods, respectively, which are not the same in  $6M \times 6M$  positions, i.e., at each position  $\mathbf{X}(t)$ ,  $\mathbf{D}$ ,  $\mathbf{E}$ , and  $\mathbf{Q}$  correspond to different orders.  $N$  denotes the number of buoy modules.

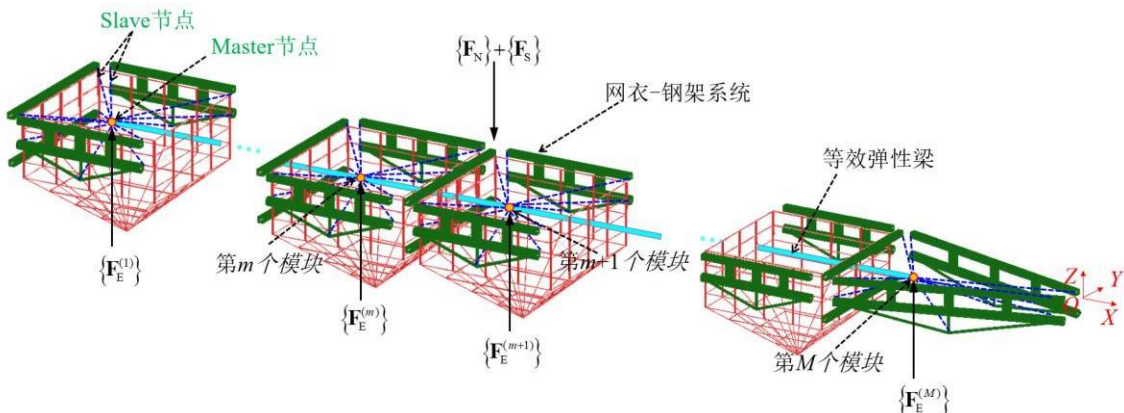


Figure 6-3 Water elasticity analysis model of large cages  
Fig. 6-3 Coupling hydroelasticity model of large fish cages

According to the above analysis, the water elasticity analysis method of large cage of ship type can be obtained, such as: fig6-4 Shown:

1. Hydrodynamic analysis in the frequency domain: The continuous floating body is

discretized into a multi-module system, and the first-order wave excitation force transfer function, additional mass, wave damping coefficient and wave field velocity transfer function of the multi-module system considering the interaction between modules are solved in the frequency domain by using the multi-body hydrodynamics and potential flow theory.

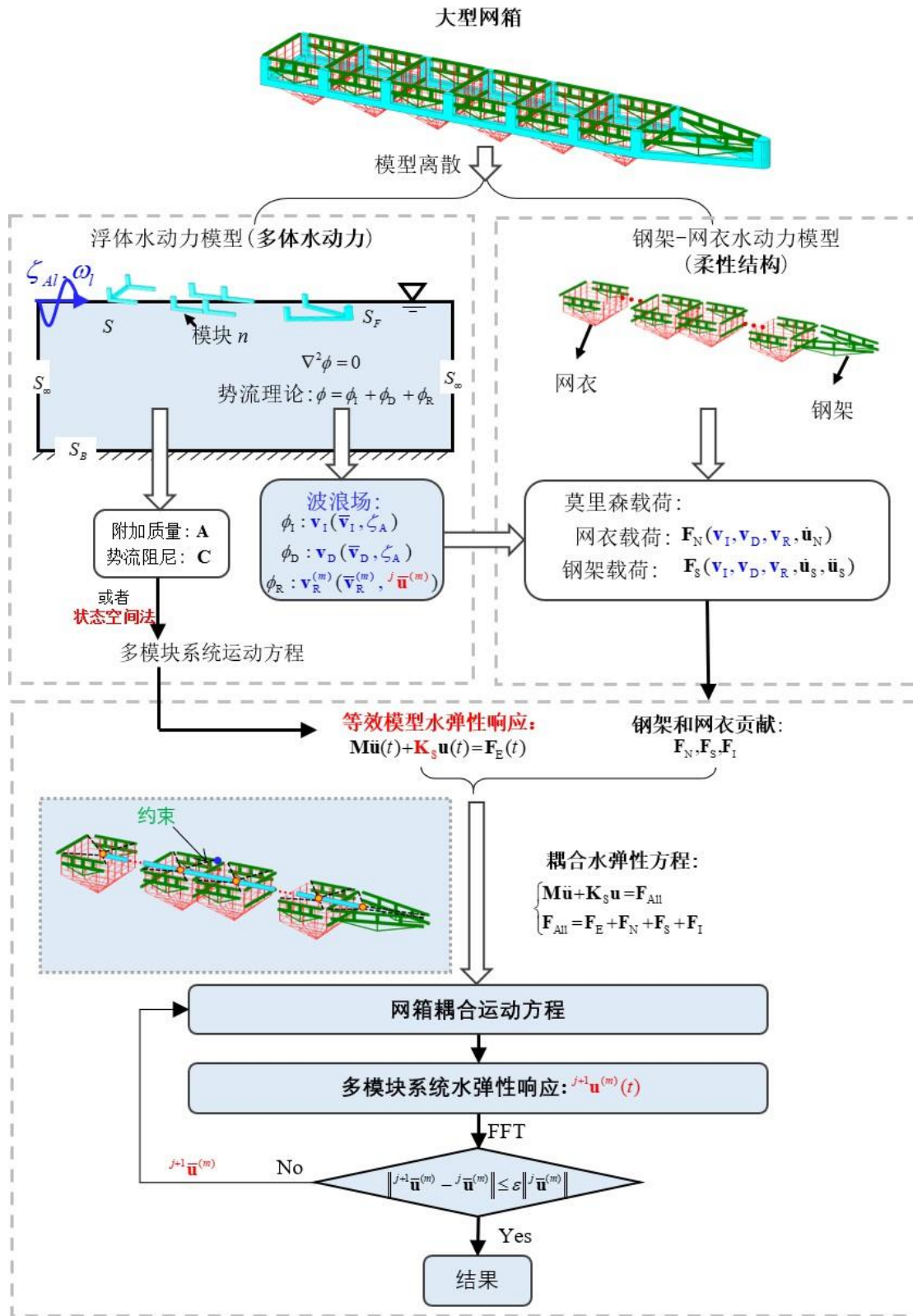


Figure6-4 Flow chart of water elasticity response analysis of large cages

Fig. 6-4 Flowchart of the hydroelasticity response analysis of the large fish cage

2. Time domain load calculation: establish the equivalent elastic beam model of the floating body and the steel frame structure, and the wave excitation force of the floating

body

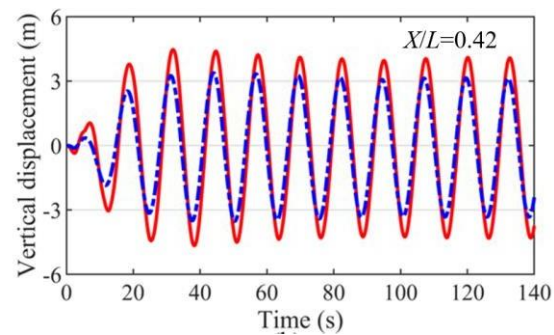
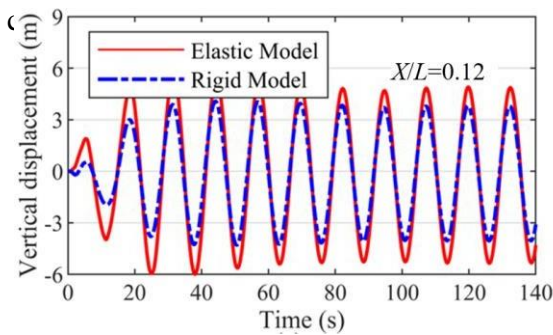
The radiative load of the buoy is determined by the additional mass and the wave damping (direct application of the additional mass and the wave damping, or the state space method), the hydrodynamic load of the steel frame and the net can be calculated by the Morrison formula, and the preliminary wave velocity field only considers the influence of the incident wave and the diffracted wave.

3. Time-domain iterative calculation: Establish a water elasticity analysis model of large-scale cages, solve the water elasticity response of large-scale cages under waves in the time domain, and obtain the motion response of each float module. According to the motion response of each module and the velocity transfer function of the radiation wave, the point velocity of the water quality generated by the radiation wave is determined, and the velocity field generated by the incident wave, the diffraction wave and the radiation wave is reconstructed, and then the water elastic time domain response of the new large cage under the wave is solved. Finally, through numerical iteration, the final disturbance wave field is determined, and the balance between the motion of the multi-module system and the hydrodynamic load of the net coat and the steel frame is obtained, and the dynamic calculation of the hydroelastic model of the large-scale cage is realized, and the hydroelastic response analysis of the cage is carried out. Figure 6-4 is a flowchart of the water elasticity analysis of a large cage.

## 6.5 Analysis of water elasticity response of large cages under regular waves

### 6.5.1 Analysis of the influence of cage cross-sectional stiffness on water elastic response

The large cages in this article are moored at a single point, so the oblique and cross-wave conditions do not occur in practice, and only the  $180^\circ$  wave direction is considered in this



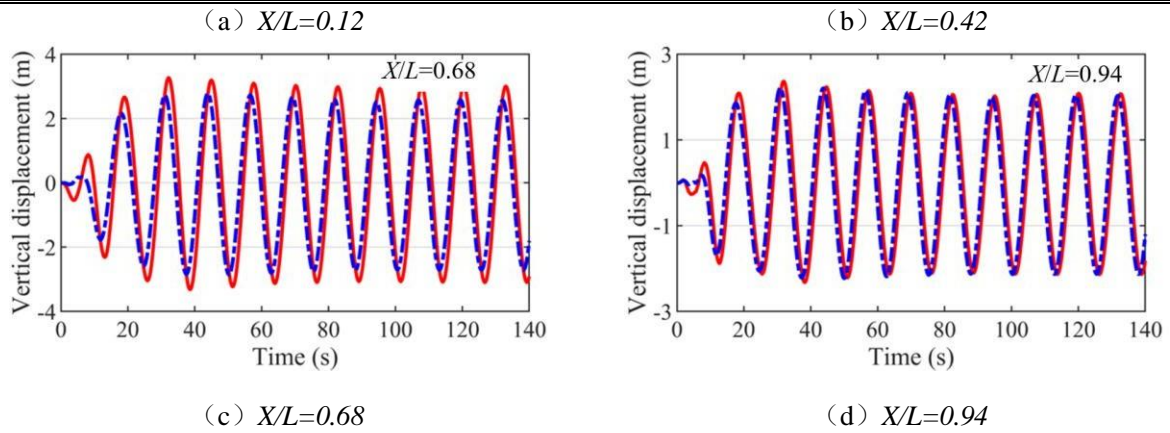
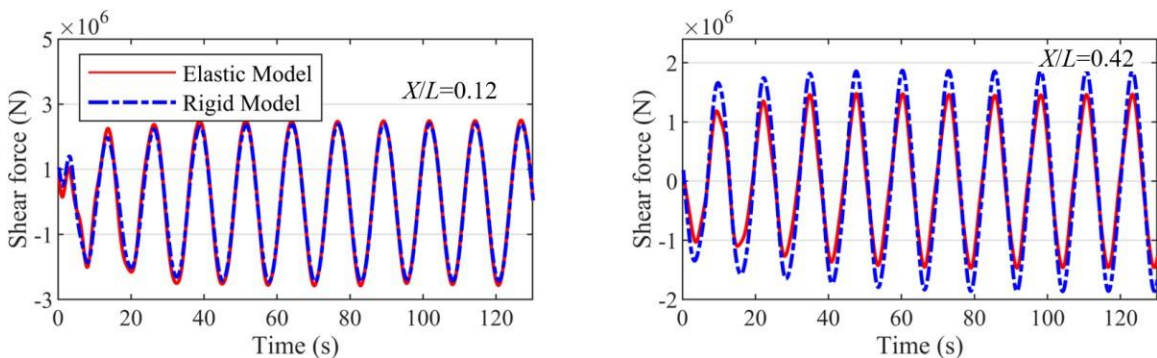


Figure 6-5 Vertical motion calendar of the cage at a wave height of 19.2 m

Fig. 6-5 Time series of the vertical displacement in the wave height 19.2 m.

Figure 6-5 shows the time history of the vertical movement of the cage at different cross-sectional positions at a wave height of 19.2 m, corresponding to the wave frequency 0.5 rad/s. It can be seen from the figure that under the rigid model, the vertical displacement of different cross-section positions decreases to varying degrees. As the  $X/L$  increases (from bow to stern), the magnitude of the decrease decreases, and the *vertical motion response of*



*the elastomer model and the rigid model is almost identical at the stern section ( $X/L=0.94$ ).*

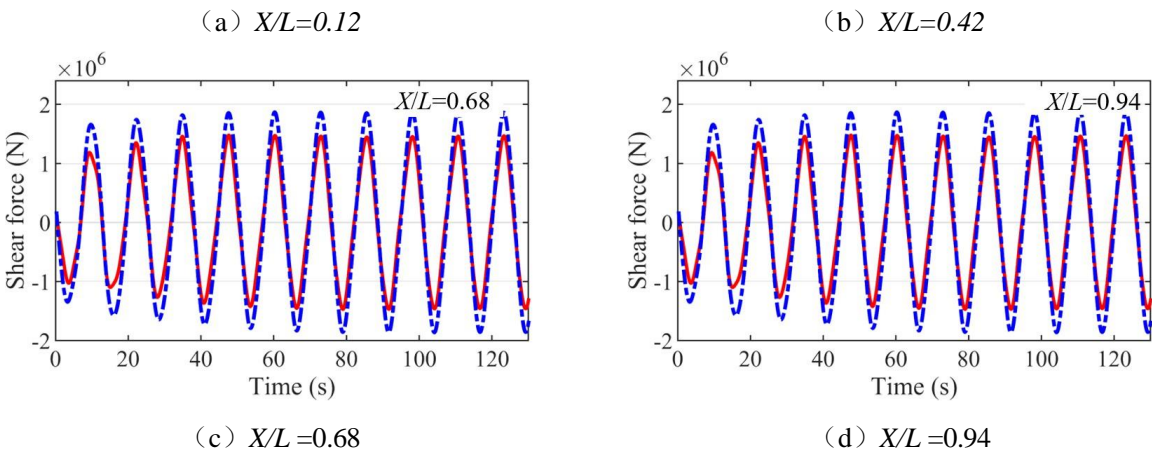


Figure 6-6 Cage cross-section shear time history at wave height of 19.2 m

Fig. 6-6 Time series of the cross-sectional shear force in the wave height 19.2 m

fig 6-6 It's wave height 19.2 m Time history of vertical cross-section shear force at different cross-section positions of the cage, fig 6-7 It's wave height

The time lapse of the vertical cross-section moment at different cross-section positions of the cage at 19.2 m, corresponding to a wave frequency of 0.5 rad/s. For the cross-sectional shear force, the cross-sectional shear force of the two models is almost the same in the cross-section near the bow of the cage, and with the increase of  $X/L$ , the cross-sectional shear force in the rigid model is significantly higher than that in the elastic model. In the cross-section close to the bow of the cage, the cross-sectional moments of the elastic model are even slightly greater than those of the rigid cross-sections. However, at other cross-section locations, the cross-sectional moment of the rigid model is much greater than that of the elastic model, where the bending moment of the rigid model is twice that of the elastic model in the cross-section near the middle. However, the specific analysis process of this problem is still very complex, and the reason for this can be explained by a simple analysis: assuming that the cage is in a

central arch state at a certain time, the cage is split along the amidships. For the left part of the cage, the bending moment  $M$  of the middle section is counterclockwise, and the direction of the hydrodynamic load  $F_U$  near the amidship is vertically upward (from the amidship  $L_U$ ), ~~Hydro~~ is vertically downward (from the amidship).  $L_B$  direction is vertically downward (from the amidship  $LG$ ), ~~Hydro~~ is vertically upward (from Amidship  $L_{buoy}$ )~~Hydro~~

Lambert's theorem shows that the force of inertia  $ma$  is perpendicular upwards (from the amidship  $L/2$ ) to the hull surface. This is highly non-dimensionalized by the weight of the cage, which is proportional to the volume of the cage.

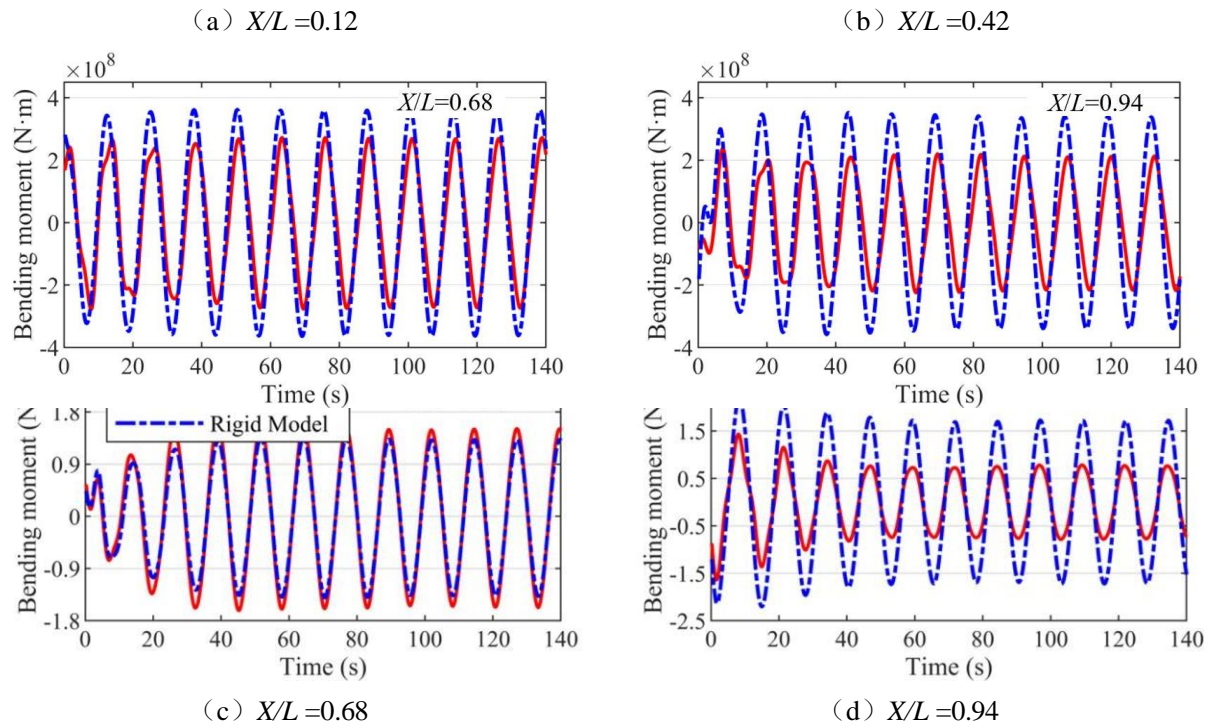


Figure 6-7 Vertical moment history of cage section at wave height of 19.2 m

Fig. 6-7 Time series of the cross-sectional vertical bending moment in the wave height 19.2 m

In order to obtain a comprehensive and in-depth understanding of the cage cross-section response, the cross-section stiffness is changed by changing the elastic modulus of the cage cross-section material, and the cross-section stiffness is selected over a very large range. Although this can be difficult in reality and cannot be achieved by optimizing the cross-section design. However, correlation analysis in numerical research is still of great significance. In order to further study the influence of cross-section stiffness on the hydroelastic response, this section *calculates the hydroelastic response of the cage under different cross-sectional stiffness K based on the cross-section stiffness K0 above.*

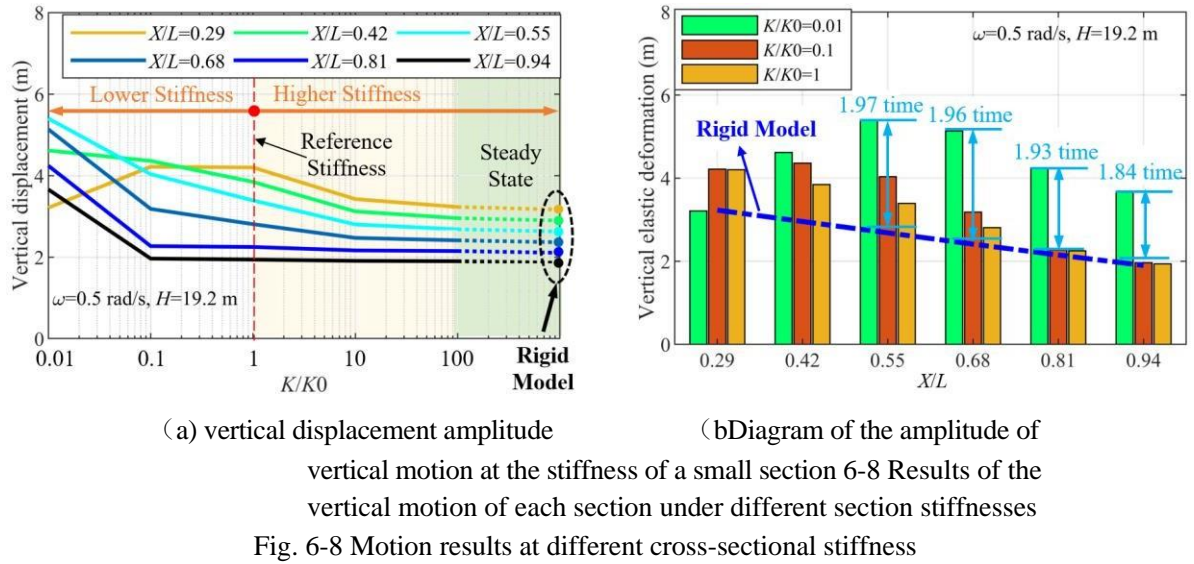
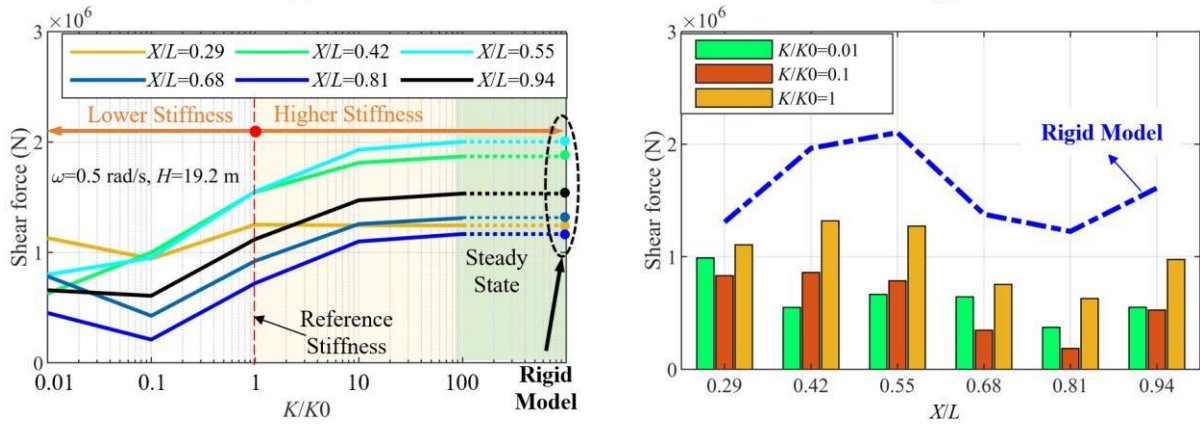


Fig. 6-8 Motion results at different cross-sectional stiffness

Fig. 6-8(a) shows the amplitude of the vertical motion response for each cross-section position under different cross-section stiffnesses. Under small cross-sectional stiffness, the amplitude of vertical motion increases first and then decreases as  $X/L$  increases. With the increase of cross-section stiffness, the vertical response amplitude of different cross-sections gradually decreases and tends to be stable. The cross-section closer to the stern enters the stabilization phase earlier. As the cross-section stiffness increases to a certain extent, the vertical motion of the individual cross-sections decreases linearly along the x-axis.

Fig. 6-8(b) shows the *vertical motion amplitude of each section of the cage under the stiffness of the small section ( $K/K_0 \leq 1$ )*. By comparing the vertical motion time calendar under different cross-section stiffness with the motion time calendar under the rigid model, the normal deformation of the cage caused by the cross-section elasticity can be obtained. At small cross-section stiffness, the elastic deformation tends to increase and then decrease along the x-axis. With the gradual increase of cross-section stiffness, the elastic deformation also decreases, and the *maximum deformation amplitude at  $K/K_0=1$*  is only 1.3 m, while  $K/K_0=0.01$  The maximum deformation amplitude is 4.7 m, which is 3.6 times that of the



former. In addition, the *elastic deformation of some cross-sections at  $K/K_0=0.01$*  is almost 2

times greater than the rigid body motion. This indicates that the cross-section stiffness has a significant effect on the vertical motion of the cross-section, and improving the cross-section stiffness to a certain extent is conducive to reducing the motion response.

(a)Vertical shear force amplitude  
(b)Diagram of the amplitude of the vertical shear force under the stiffness of a small section 6-9 Results of the vertical shear force of each section under different cross-section stiffnesses.

Fig. 6-9 Cross-sectional bending moment at different cross-sectional stiffness

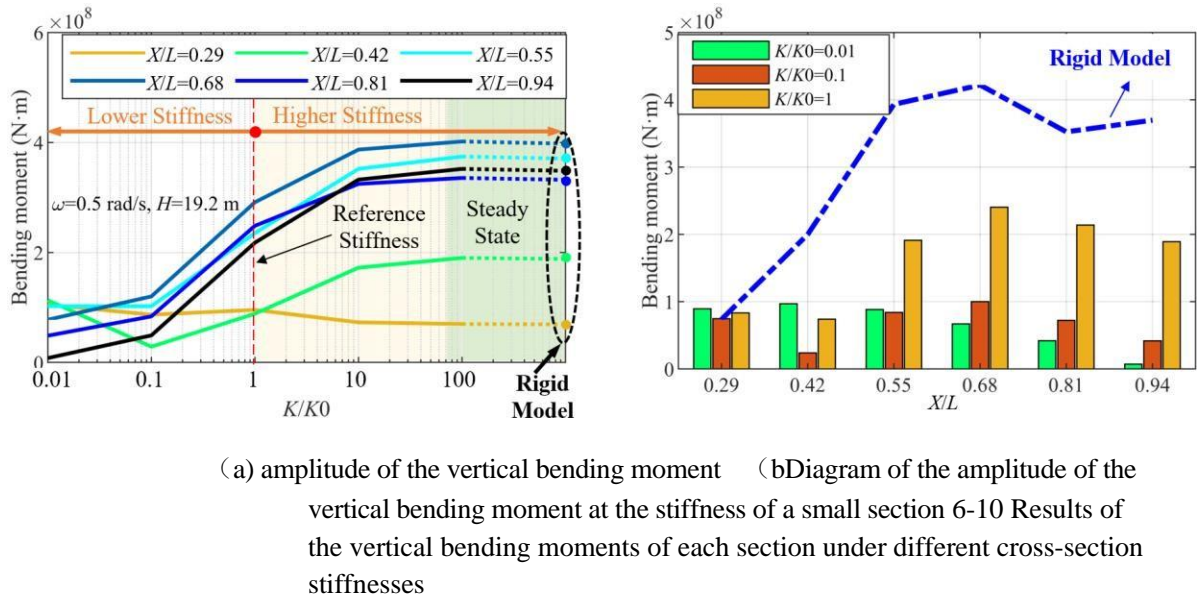


Fig. 6-10 Cross-sectional bending moment at different cross-sectional stiffness

fig 6-9 and fig 6-10 They are the load amplitudes of the cross-sectional shear force and vertical bending moment under different cross-sectional stiffnesses and the vertical load amplitudes under the elastic stiffness of small cross-sections. With the increase of cross-section stiffness, the overall cross-section shear force and vertical bending moment will increase to a certain extent, and when the cross-section stiffness increases to a certain extent, the cross-sectional load gradually tends to be stable, such as  $K/K_0=100$ . The results are almost identical to those of the rigid body model. As can be seen from the figure, the reduction of the cross-section load due to the elastic deformation is of the same order of magnitude as the cross-section load under the rigid model. Moreover, the smaller the cross-sectional stiffness of the cage, the greater the reduction of the cross-sectional load caused by elastic deformation. Thereinto  $K/K_0=0.01$  The maximum amplitude of the reduction in cross-section shear force and vertical bending moment are respectively  $1.4e6 \text{ N}$  and  $3.7e8 \text{ N}\cdot\text{m}$  whereas  $K/K_0=1$  The cross-sectional shear force and vertical bending moment reduction at the corresponding position are respectively  $4e5 \text{ N}$  and  $1.3e8 \text{ N}\cdot\text{m}$ , respectively 3.5 times and more 2.8 Fold. This shows that reducing the cross-sectional stiffness significantly reduces the cross-sectional load of the cage.

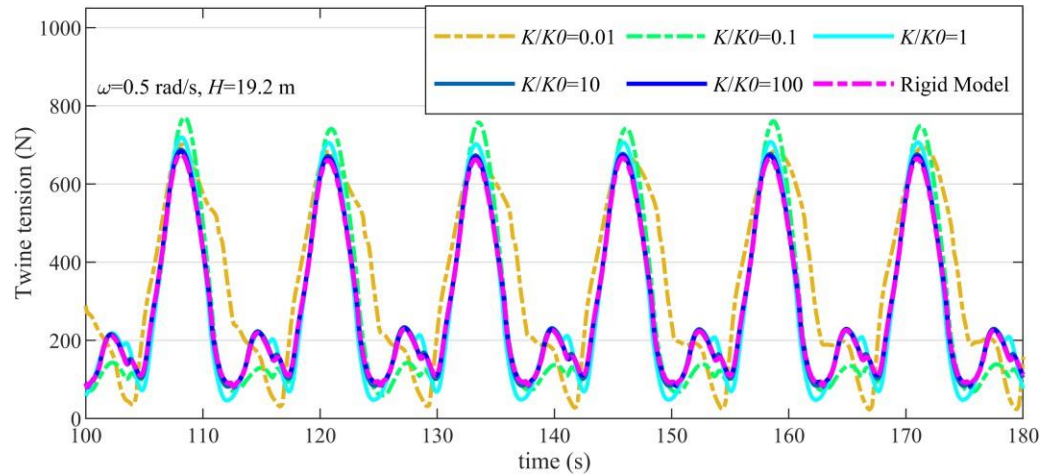


Figure 6-11 Tension time of the horizontal network cable near the water surface at the bow of the cage at different stiffnesses

Fig. 6-11 Time series of twine tension of the horizontal net element near the water surface at cage bow at different cross-sectional stiffness

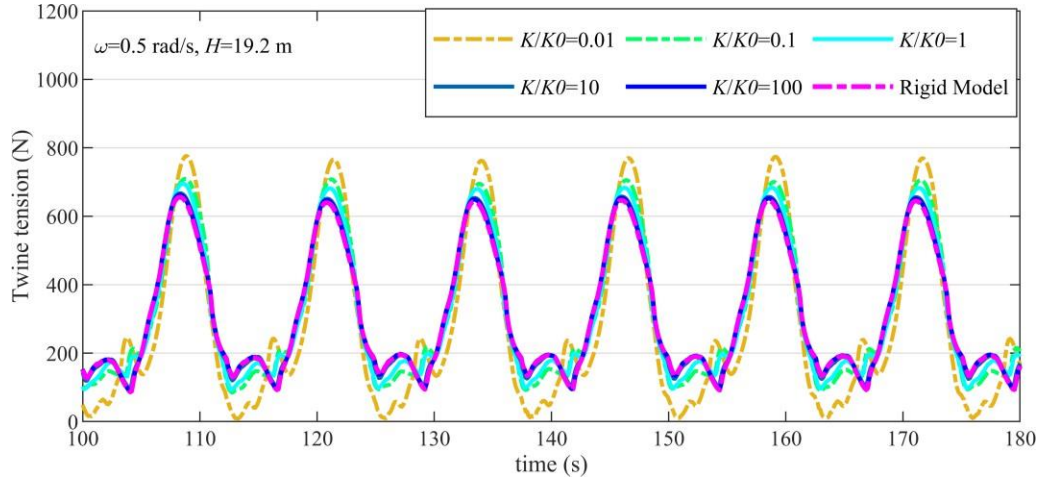


Figure 6-12 Tension duration of the horizontal network cable near the water surface at the amidship of the cage under different stiffnesses

Fig. 6-12 Time series of twine tension of the horizontal net element near the water surface at cage midship at different cross-sectional stiffness

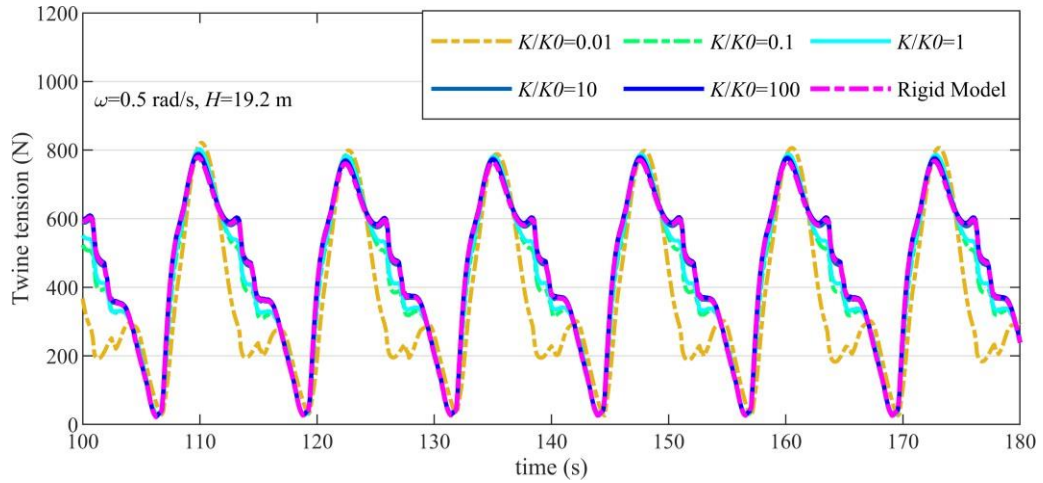


Figure 6-13 Tension history of the horizontal network cable near the water surface at the stern of the cage under different stiffnesses

Fig. 6-13 Time series of twine tension of the horizontal net element near the water surface at cage stern at different cross-sectional stiffness

Fig. 6-11~Fig. 6-13 are the tension time of the horizontal network line near the water surface of the cage bow and amidship and stern breeding units under different stiffnesses, the wave height of the working conditions is 19.2m, and the wave frequency is 0.5rad/s. As can be seen from the figure, there is little difference between the network cable tensions at different stiffness at the selected three positions. Even at the stiffness  $K/K_0=10$  vs.  $K/K_0=100$  It almost coincides with the tension curve under the rigid model. This is due to the fact that the cable tension of the net is determined by the hydrodynamic force to which the net is subjected. According to Morrison's formula, the calculation of the hydrodynamic

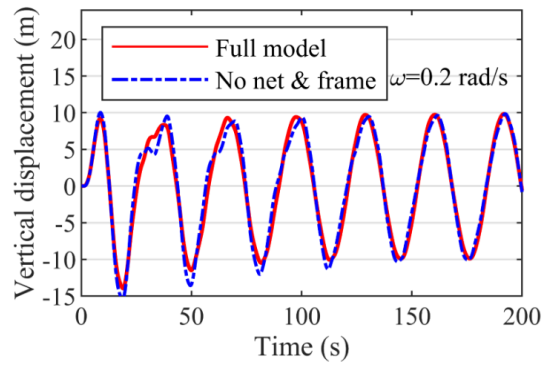
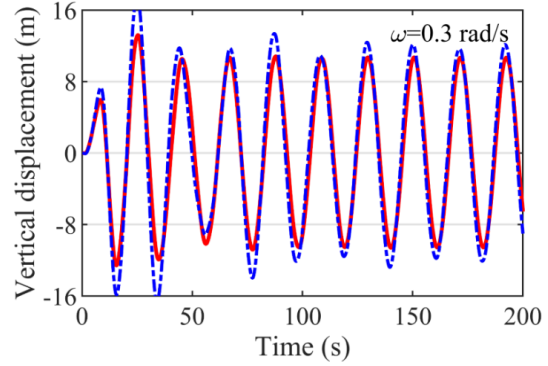
force of the net coat is only related to the relative water quality point velocity. The influence of the elastic deformation of the main steel structure on the velocity of water quality points is mainly reflected in two aspects: the change of the motion response of the cage directly caused by the elastic deformation leads to the change of the movement speed of the network cable; The change in the water depth position of the net due to elastic deformation leads to the change in the water quality point velocity. However, the above two points have an effect on the velocity of the relative water quality point

The sound is limited, so it does not significantly change the cable tension of the net. Compared with the tension results under the rigid model, the network line tension of the model with less cross-section stiffness of the main steel structure is slightly larger. This is mainly due to the fact that the cage motion response is more significant under the smaller cross-sectional stiffness, which leads to a larger relative velocity between the net motion and the water quality point velocity in the flow field, thus increasing the hydrodynamic load on the net. However, on the whole, the structural elasticity of the main steel structure has a relatively limited effect on the cable tension of the net coat.

Through the above analysis of large cages, it is helpful to fully understand the influence of cross-sectional stiffness of large cages on water elasticity. In particular, it should be noted that when the cross-sectional stiffness of the cage is reduced, the motion response of the cage will increase, while the vertical bending moment and shear force of the cross-section will decrease as a whole. The maximum vertical bend inherent period of the cage is about 5 s. The results show that reducing the flexibility of the structure (i.e., the bending stiffness  $EI$  of the cage as a whole, which is *the product of the elastic modulus E of the section and the moment of inertia of the section I*) can be used for the structural design of the cage, thereby reducing the cost. However, in the actual design, the options for changing the modulus E of the cross-section are very limited, because they are the same for the most common steel materials . Therefore, the main option is to reduce the cross-section moment of inertia  $I$ , *but this also leads to a certain reduction in the cross-section modulus and thus an increase in the cross-section stress level. Theoretically, it is possible to adopt materials with higher yield strength and pay attention to the fatigue design of welded joints, so as to achieve an acceptable structural design.*

### **6.5.2 Analysis of the influence of hydrodynamic load of net clothing and steel frame on the overall hydroelastic response of large cages**

Figure 6-14 shows the vertical motion calendar at the center of the cage section at different wave frequencies. It can be seen from the figure that when the hydrodynamic load of the net and the steel frame is not considered, the vertical motion amplitude of the cage increases to a certain extent, and when the wave frequency is 0.4 rad/s, the vertical motion amplitude of the cage increases most obviously, which is due to the damping effect of the hydrodynamic load of the net coat, thus slowing down the motion response. Figure 6-15 shows the *cross-sectional shear force of the cage at different wave frequencies at X/L=0.5*. When the hydrodynamic forces of the net and steel frame are taken into account, the cross-sectional shear force of the cage increases at all frequencies. This is due to the fact that the hydrodynamic force of the mesh is transmitted to the main steel structure through the connector, resulting in an increase in the cross-section shear force.

(a)  $\omega=0.2 \text{ rad/s}$ (b)  $\omega=0.3 \text{ rad/s}$

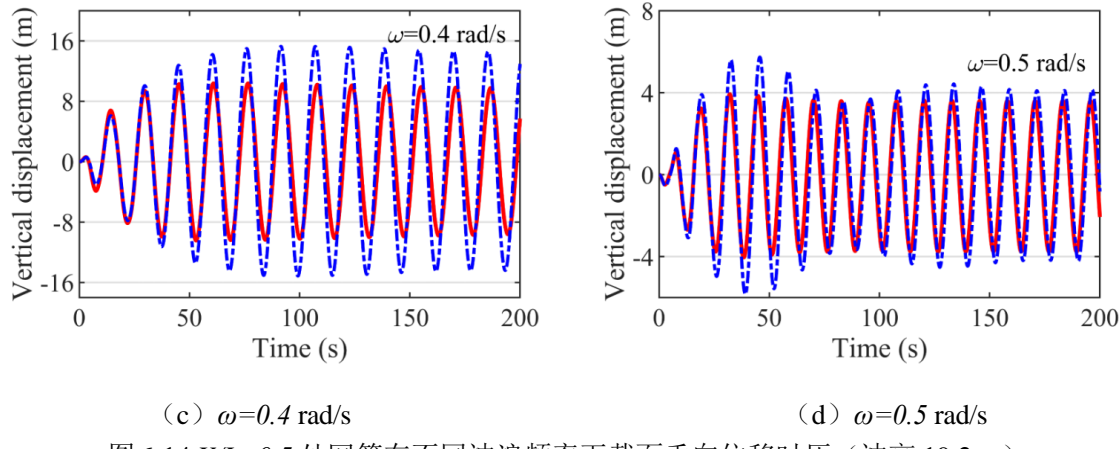


图 6-14  $X/L=0.5$  处网箱在不同波浪频率下截面垂向位移时历 (波高 19.2 m)

Fig. 6-14 Time series of the vertical displacement at  $X/L=0.5$  in the wave height 19.2 m

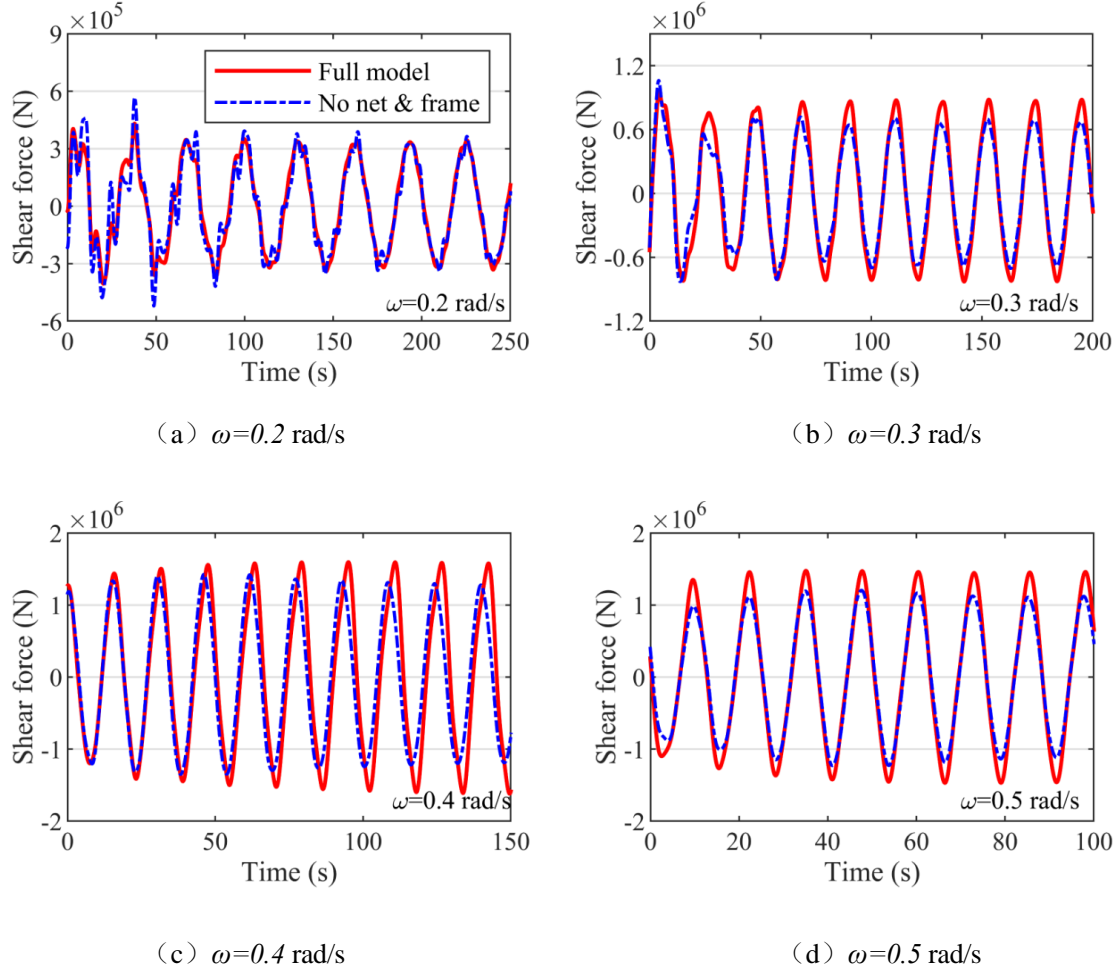


Figure 6-15 Vertical shear duration of the cage at different wave frequencies at different wave frequencies (wave height 19.2 m).

Fig. 6-15 Time series of the cross-sectional shear force at  $X/L=0.5$  in the wave height 19.2 m

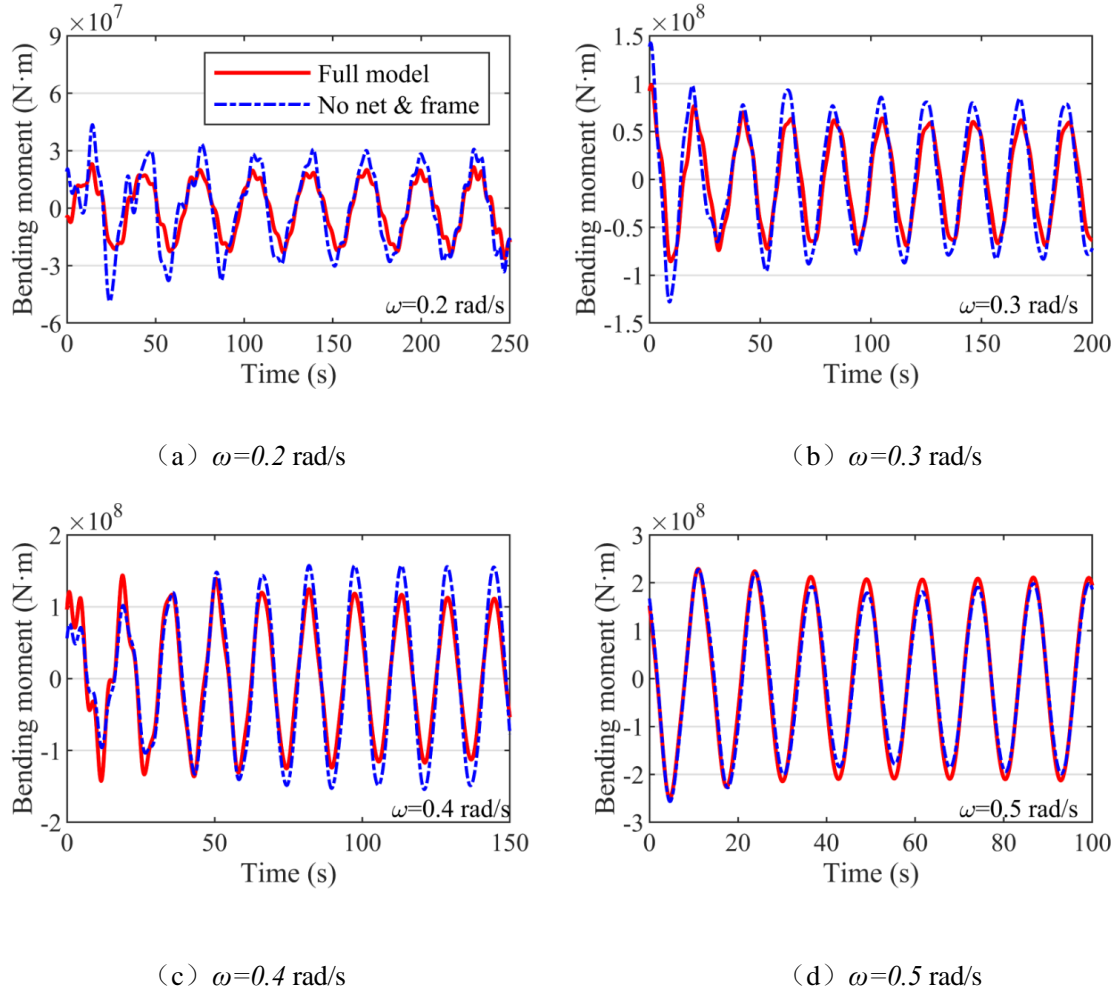


Figure 6-16 Perpendicular moment history of the cage at  $X/L=0.5$  at different wave frequencies (wave height 19.2 m).

Fig. 6-16 Time series of the cross-sectional vertical bending moment at  $X/L=0.5$  in the wave height 19.2 m

Figure 6-16 shows the vertical moment history of the cage at *different wave frequencies* at  $X/L=0.5$ . At lower wave frequencies, the presence of net and hydrodynamic loads will reduce the vertical bending moment of the cage cross-section, and when the wave frequency is 0.5 rad/s, the load of the net and steel frame will increase the cross-sectional bending moment. In contrast, the influence of mesh and steel frame load on the cross-sectional shear force is more obvious, and the influence on the bending moment will change with the change of wave frequency. However, this change introduces uncertainty in the calculation of the cross-section load, so more attention should be paid to it in the safety analysis.

### 6.5.3 Analysis of the influence of incident wave frequency and amplitude on the water elastic response of large cages

Figure 6-17(a) and (b) are the amplitudes of vertical motion of the cage at different

wave frequencies and heights, respectively. With the increase of wave frequency, the vertical motion amplitude near the bow of the cage increases first and then decreases, and the vertical motion amplitude near the stern decreases gradually. With the increase of wave height, the vertical motion of each section gradually increases. Under the conditions shown in Figure 6-17, the vertical motion of the cross-section gradually decreases as  $X/L$  increases, i.e., the vertical motion response from bow to stern decreases.

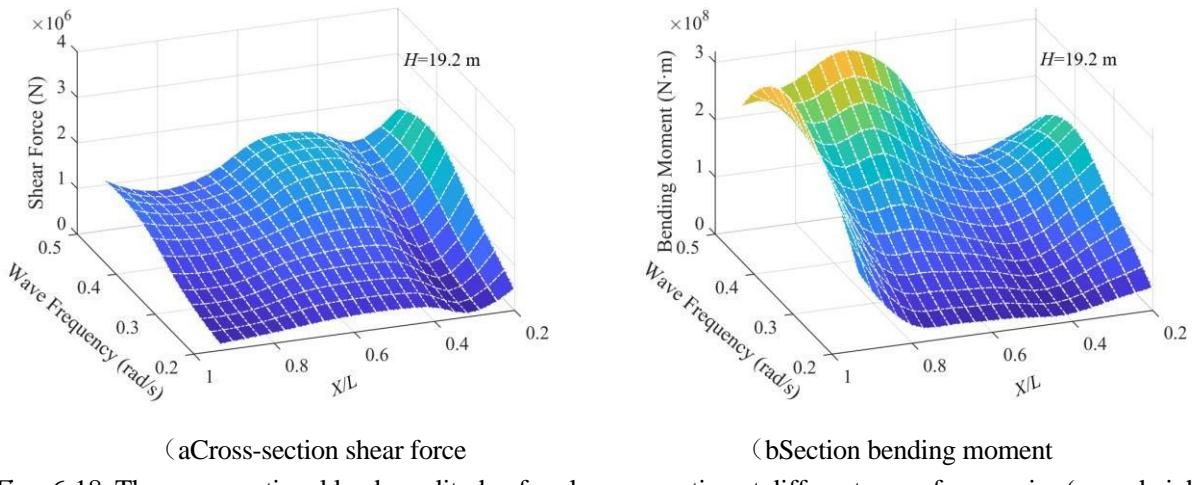
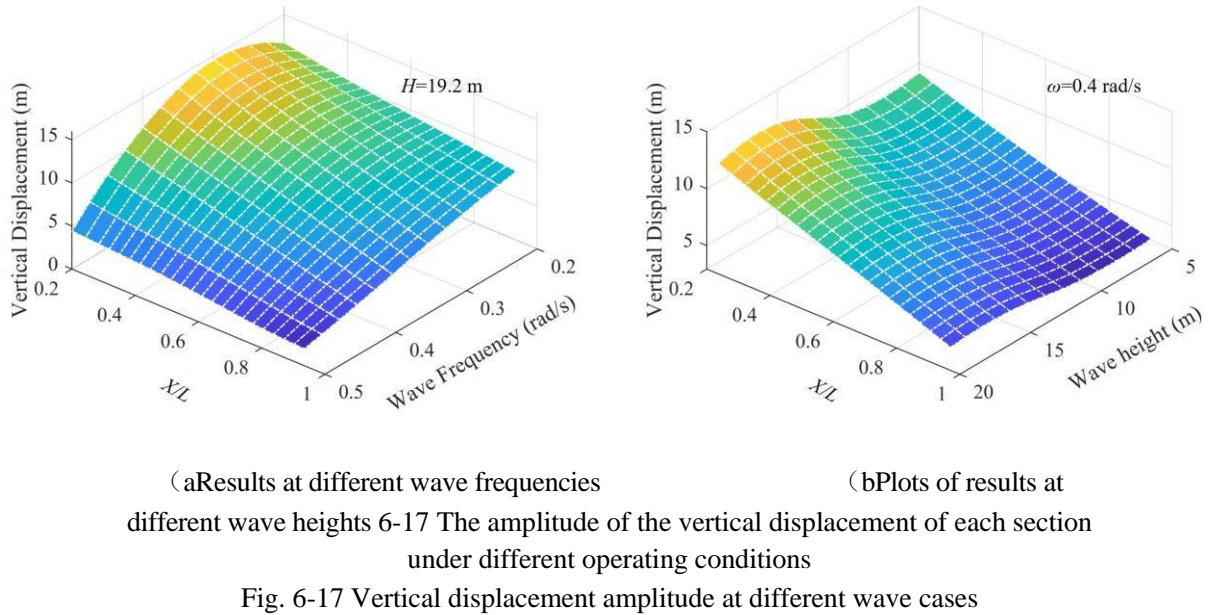


Figure 6-18 The cross-sectional load amplitude of each cross-section at different wave frequencies (wave height 19.2m).

Fig. 6-18 Cross-sectional force amplitude at different wave frequencies in wave height 19.2 m

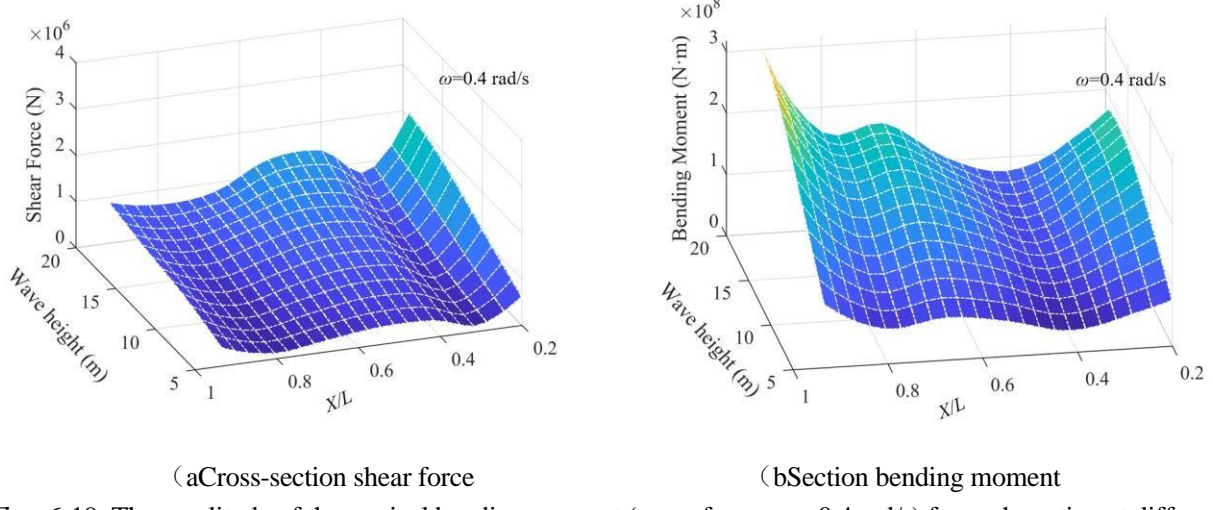


Figure 6-19 The amplitude of the vertical bending moment (wave frequency 0.4 rad/s) for each section at different

wave heights

Fig. 6-19 Cross-sectional force amplitude at different wave heights in the wave frequency 0.4 rad/s

fig 6-18 and fig 6-19 They are the shear force and vertical bending moment amplitude of cages under different cross-sections under different wave frequencies and wave heights. On the whole, with the increase of wave frequency, the cross-section shear force and cross-section bending moment will gradually increase, but the cross-section shear force and bending moment at individual positions will be 0.4 rad/s. The peak decreases at this point, where the wavelength is slightly larger than the cage length. According to the relevant code, when the wavelength is equal to the length of the structure or slightly greater than the length of the structure, the cross-section load is prone to the maximum value. As the wave height increases, both the cross-section shear force and the bending moment increase. However, with the increasing wave height, the growth rate of cross-section shear force increases, while the growth rate of cross-section bending moment slows down.

#### 6.5.4 Analysis of the influence of the number of discrete modules on the water elastic response of large cages

As can be seen from the previous analysis, the correlation matrix in the equilibrium equation of a floating body is considered as a rigid body with 6 degrees of freedom. For order  $6 \times 6$ , the number of data (or intermediate matrices) that need to be fitted when solving the radiation load using the state-space method is  $6 \times 6 = 36$  sets, and when the discrete is  $N$  floats, the number of data (or intermediate matrices) that need to be fitted reaches  $6N \times 6N = 36N^2$  group, which greatly reduces computational efficiency; Using the convolutional integration method to solve for radiation loads can have a similar computational efficiency drop.

In order to realize the rapid analysis of water elastic response of large cages, this paper tries to improve the computational efficiency by appropriately reducing the number of discrete modules of the floating body. Fig. 6-20~Fig. 6-22 is the result of discretizing the continuous float into 4 modules and 7 modules, respectively. For the vertical motion amplitude of the cross-section, the reduction of the number of modules will reduce the motion response to a certain extent, the motion amplitude is reduced by an average of 9%, while the shear amplitude of the cross-section changes by 12% on average, and the bending moment amplitude of the cross-section changes by 11% on average, and the overall trend of the cross-section load under the 4 modules is the same. 7 Module results are consistent. Based on this, In the next section, the Irregular Wave case selects the 4-module model for the calculation.

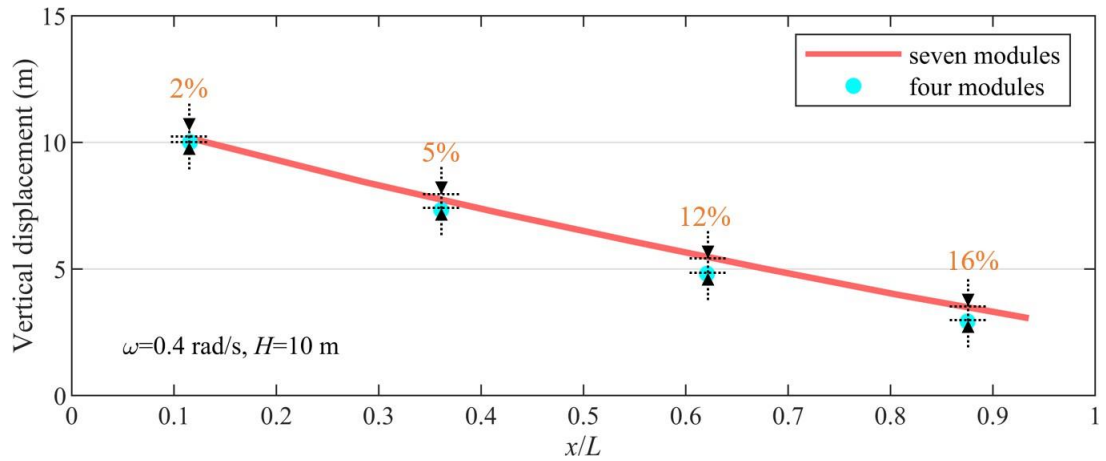


Figure 6-20 Vertical displacement response results for different cross-section positions with different number of modules

Fig. 6-20 Vertical displacement at different cross-section under different number of modules

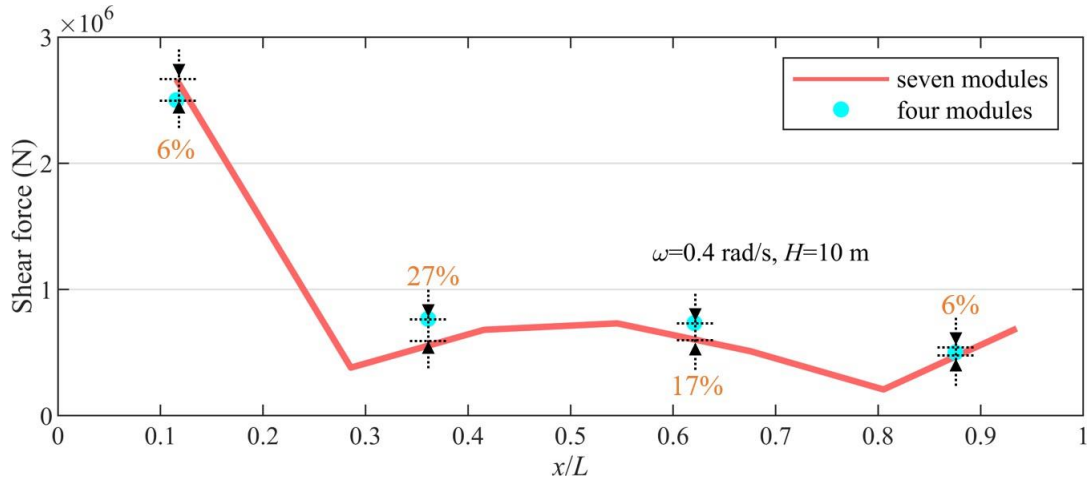


Figure 6-21 Vertical shear response results for different cross-section positions with different number of modules  
Fig. 6-21 Cross-sectional shear force at different cross-section under different number of modules

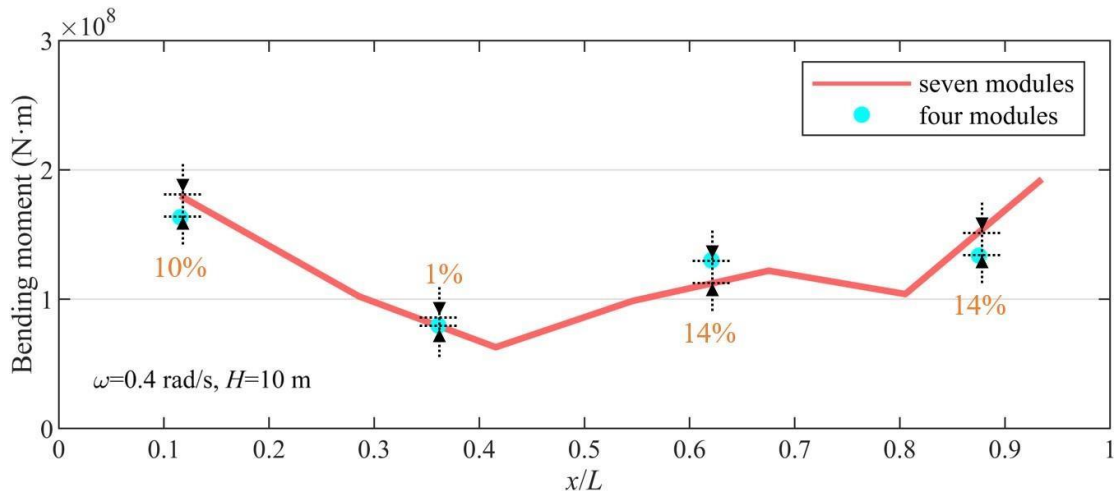


Figure 6-22 Vertical moment response results of different cross-section positions under different number of modules  
Fig. 6-22 Cross-sectional bending moment at different cross-section under different number of modules

## 6.6 Analysis of water elasticity response of large cages under irregular waves

In this section, the sense wave height of the irregular wave is 10.4 m, the peak period is 15.7 s, and the wave direction is 180°. In the response extremum analysis below, the response is assumed to satisfy the Weibull distribution, and the 99% quantile is selected as the response extremum.

### 6.6.1 Analysis of the influence of cage cross-sectional stiffness on the hydroelastic response of large cages

Figure 6-23 is the vertical displacement time lapse of the rigid and elastic models at  $X/L=0.5$  under irregular waves. It can be seen from the figure that the vertical displacement

of the cage will slow down to a certain extent under the rigid model, but it is consistent with the movement trend of the vertical displacement of the elastic model on the whole, which is also consistent with the results under the regular wave in the previous article.

Figure 6-24 is the statistical results of the vertical displacement of the rigid model and the elastic model at different cross-sections under irregular waves. With the *gradual increase* of  $X/L$ , the extreme value of vertical motion response and RMS value of the cross-section of the cage gradually decrease. Compared with the results of the elastic model, the vertical motion response and RMS values of the cage under the rigid model are reduced, and the average reduction of the extreme motion response and RMS values under the cross-section shown in the figure are 35% and 23%, respectively. From the energy point of view, the reason why the vertical displacement of the cross-section under the elastic model is greater is that the elastic model can convert the wave energy into the strain energy of the structure through elastic deformation, resulting in a more significant motion response.

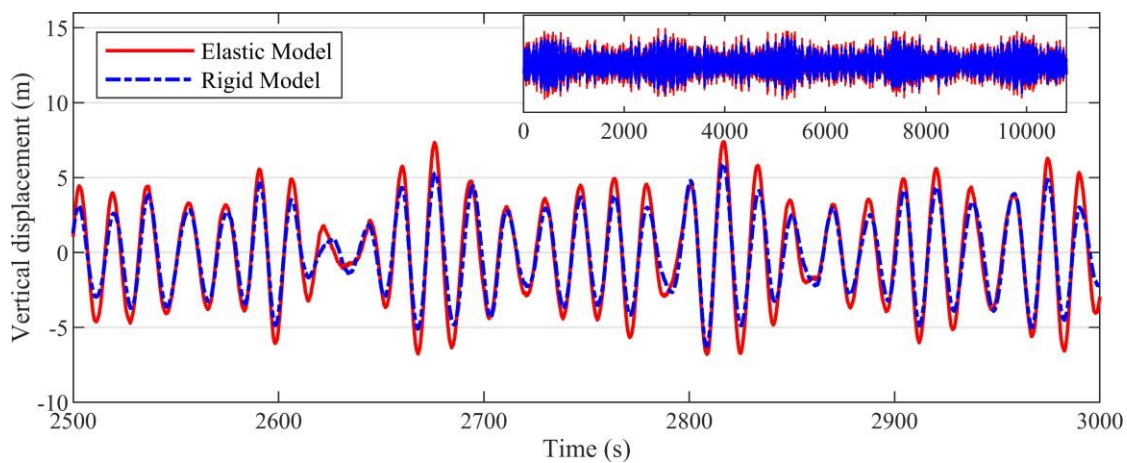


Figure 6-23 Vertical displacement time lapse of the rigid and elastic models at  $X/L=0.5$  under irregular waves

Fig. 6-23 Time series of the vertical displacement of rigid model and elastic model at  $X/L=0.5$  under irregular waves

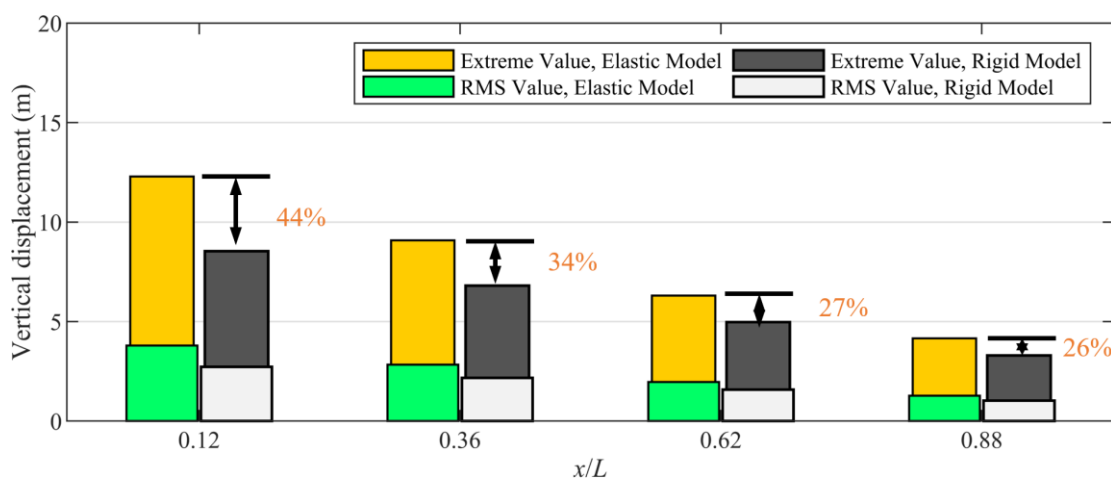


Figure 6-24 Statistical results of vertical displacement of rigid model and elastic model at different cross-sections under irregular waves

Fig. 6-24 Vertical displacement statistical results of rigid model and elastic model at different cross-sections under irregular waves

fig 6-25 and fig 6-26 It is a rigid model and an elastic model under irregular waves  $X/L=0.5$ . The vertical section load time calendar at . As can be seen from the figure, compared with the results under the elastic model, the cross-sectional shear force under the rigid model has a certain range

The degree increases, but the change is not obvious. In the rigid model, the vertical moment of the cross-section increases very significantly.

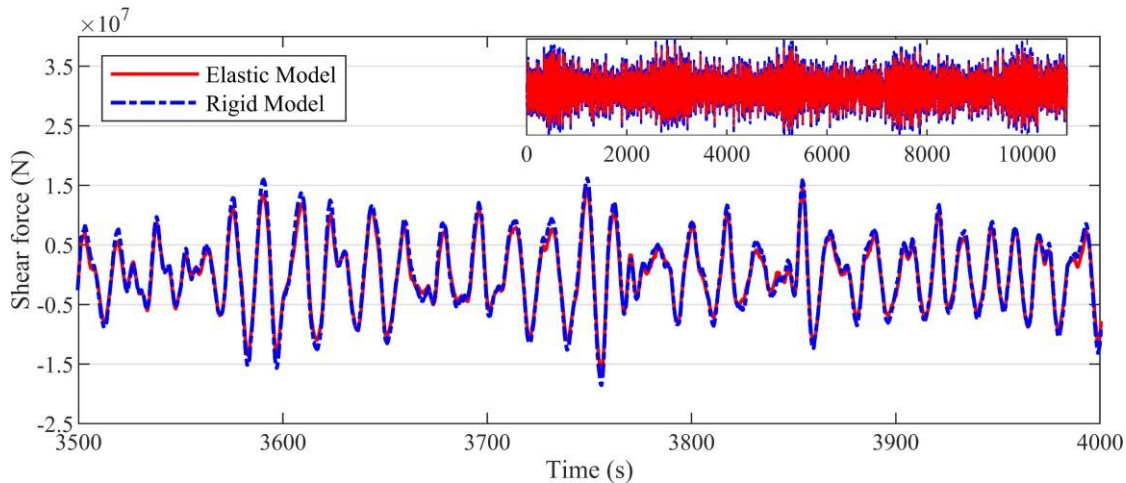


Figure 6-25 Vertical cross-section shear force history at  $X/L=0.5$  for the rigid and elastic models under irregular waves

Fig. 6-25 Time series of the cross-sectional shear force of rigid model and elastic model at  $X/L=0.5$  under irregular waves

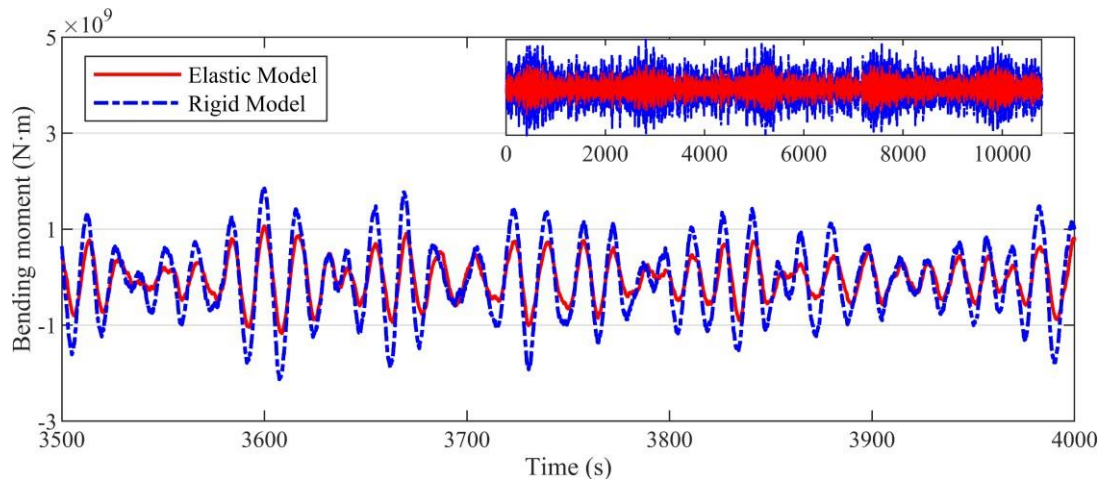


Figure 6-26 Vertical cross-section moment history at  $X/L=0.5$  for the rigid and elastic models under irregular waves

Fig. 6-26 Time series of the cross-sectional vertical bending moment of rigid model and elastic model at  $X/L=0.5$  under irregular waves

Fig. 6-27 and Fig. 6-28 are the statistical results of the vertical cross-section load of the rigid model and the elastic model at different cross-sections under irregular waves. As  $X/L$  increases (from bow to stern), the cross-sectional shear forces of both the elastic and rigid models gradually decrease, while the cross-sectional moments increase rapidly, which may be due to the structural characteristics of the cage itself. Compared with the results of the elastic model, the cross-sectional shear force of the rigid model increases to a certain extent, with an average increase of 10% and 9% in the extreme and RMS values of the cross-section. In the rigid model, the vertical moment of the bow section is significantly reduced, and the

average value of the extreme moment and RMS of the section are reduced by 41% and 40%, respectively.

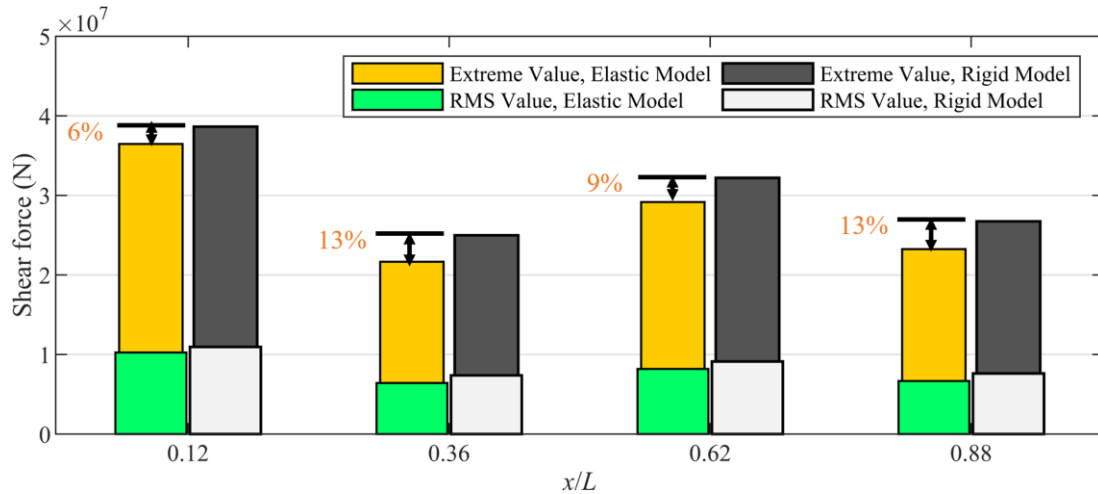


Figure 6-27 Statistical results of vertical cross-section shear force of rigid model and elastic model at different cross-sections under irregular waves

Fig. 6-27 Vertical shear force statistical results of rigid model and elastic model at different cross-sections under irregular waves

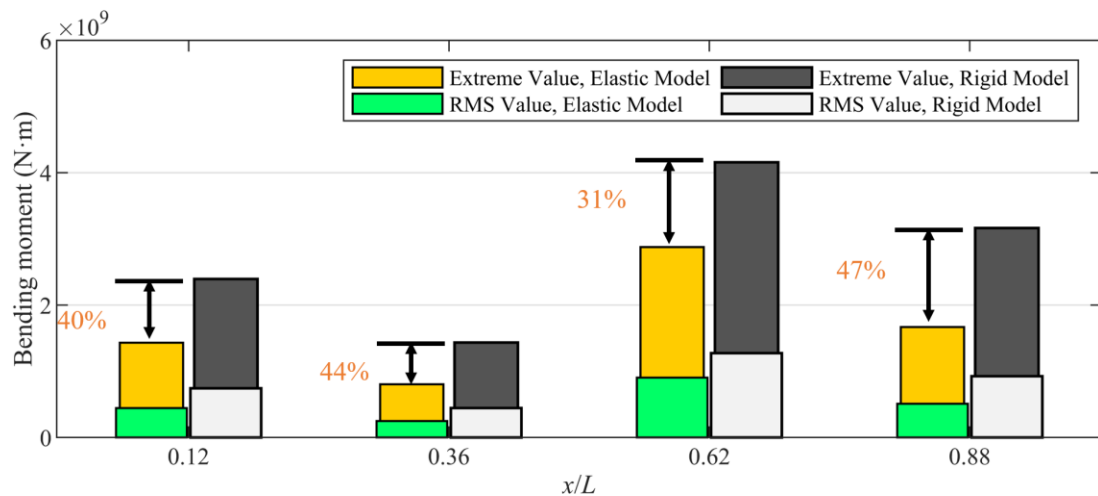


Figure 6-28 Statistical results of vertical cross-section bending moments of the rigid model and the elastic model at different cross-sections under irregular waves

Fig. 6-28 Vertical bending moment statistical results of rigid model and elastic model at different cross-sections under irregular waves

## 6.6.2 Analysis of the influence of hydrodynamic load of net clothing and steel frame on the overall hydroelastic response of large cages

Figure 6-29 is the time lapse of the cross-sectional vertical displacement of a large cage at  $X/L=0.5$  when the hydrodynamic load of the net and steel frame is taken into account under irregular waves, and the irregular calculation time is 11000s. Figure 6-30 Statistical results of vertical displacement of cross-sections at different cross-sections when the hydrodynamic forces of mesh clothing and steel frame are taken into account under irregular

waves. The model used is an elastic cage model, and the cross-section stiffness is the reference stiffness ( $K/K_0=1$ )

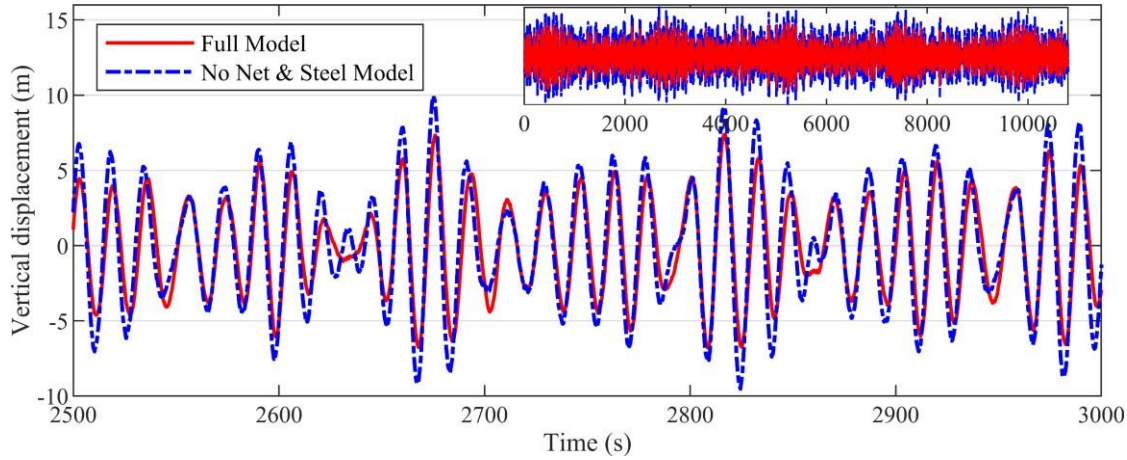


图 6-29 不规则波下是否计及网衣和钢架水动力时网箱在  $X/L=0.5$  处的垂向位移时历

Fig. 6-29 Time series of the vertical displacement at  $X/L=0.5$  of under irregular waves when considering hydrodynamic loads on the net and frame or not

As can be seen from Figure 6-30 , the hydrodynamic force of the net and the steel frame will lead to the decrease of the vertical motion of the cage to a certain extent, which is due to the damping effect of the net and the steel frame. The response and RMS values of the vertical movement of the bow of the cage to the stern of the cage gradually decreased. When the hydrodynamic load of the mesh and steel frame is not considered, the vertical motion response increases, with the average increase in response extremum and RMS value reaching 33% and 34%, respectively.

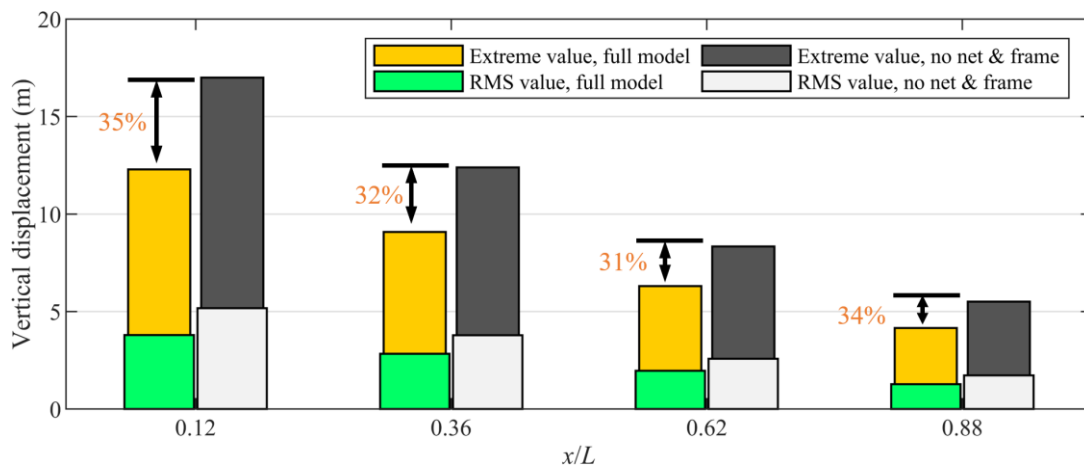


Figure 6-30 Statistical results of vertical displacement of cross-sections at different cross-sections when the hydrodynamic forces of mesh and steel frame are taken into account under irregular waves

Fig. 6-30 Vertical displacement statistical results of different cross-sections under irregular waves when considering hydrodynamic loads on the net and frame or not

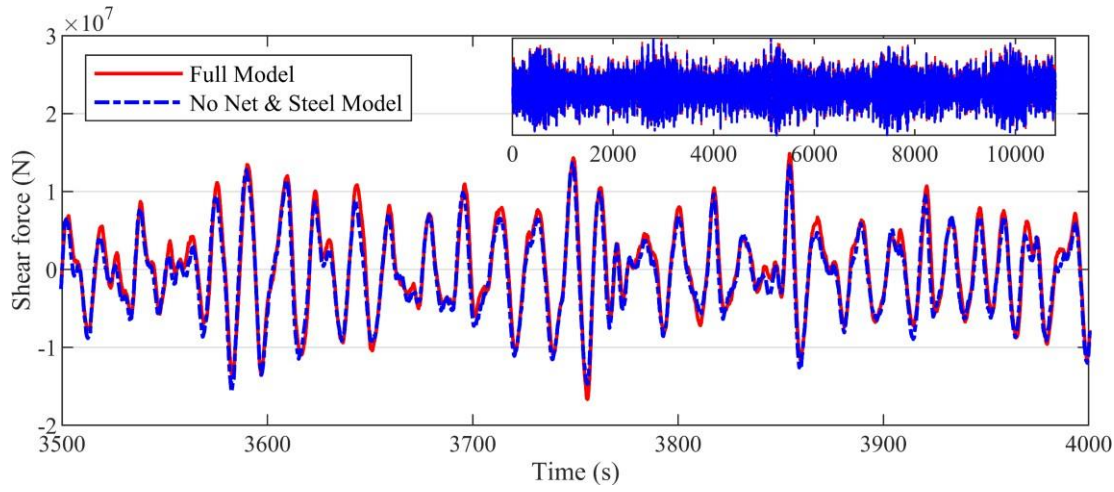
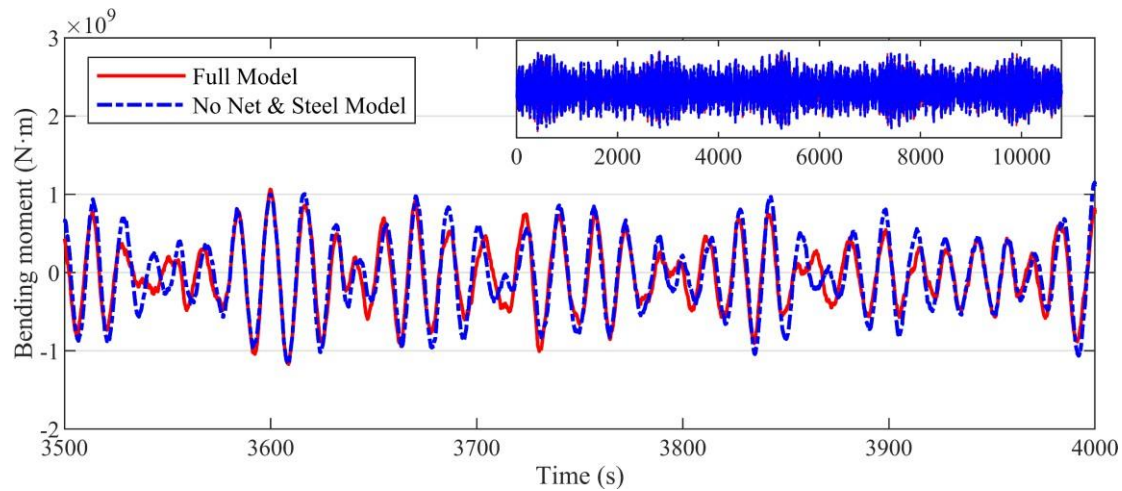


Figure 6-31 Whether the vertical shear force at  $X/L=0.5$  of the cage is taken into account under irregular waves

Fig. 6-31 Time series of the cross-sectional shear force at  $X/L=0.5$  under irregular waves when considering hydrodynamic loads on the net and frame or not

Fig. 6-31 and Fig. 6-32 are the cross-sectional vertical shear time and vertical moment time calendars of a large cage under irregular waves at  $X/L=0.5$ , respectively. As can be seen from Figure 6-31, the cross-sectional shear force will occur when the hydrodynamic load of the mesh and steel frame is taken into account

There is a slight increase, but the overall trend does not change the shear force. As can be seen from Figure 6-32, the presence of hydrodynamic forces on the net and steel frame will have a certain influence on the cross-sectional bending moment, and the influence on the cross-



sectional bending moment is different at different times, but in general, the influence of the hydrodynamic forces of the net and the steel frame on the cross-sectional bending moment is very limited.

Figure 6-32 Whether the vertical bending moment time calendar at  $X/L=0.5$  of the cage at the hydrodynamic force of the net and steel frame is taken into account under irregular waves

Fig. 6-32 Time series of the cross-sectional vertical bending moment at  $X/L=0.5$  under irregular waves when considering hydrodynamic loads on the net and frame or not

Fig. 6-33 and Fig. 6-34 are the statistical results of the vertical shear force and bending moment of the cross-section at different cross-sections under irregular waves, respectively. When the hydrodynamic load of the mesh and steel frame is not considered, the shear force of each section will decrease to a certain extent, but the change amplitude is small, and the average decrease of the extreme shear force and RMS value is only 9% and 2%, respectively. However, the hydrodynamic load of the net coat and the steel frame have different effects on the bending moments of different sections, and the bending moments of the cross-sectional parts of the bow of the cage increase slightly (two in the bow

The average increase in the extreme value of the cross-section moment and the RMS value is 15% and 18%, respectively. The average increase in the RMS value is within 1%. At  $X/L=0.62$ , the cross-section moment even decreases when the hydrodynamics of the mesh and steel frame are not considered. On the whole, the hydrodynamic force of the mesh and steel frame has limited influence on the shear force and bending moment of the cross-section.

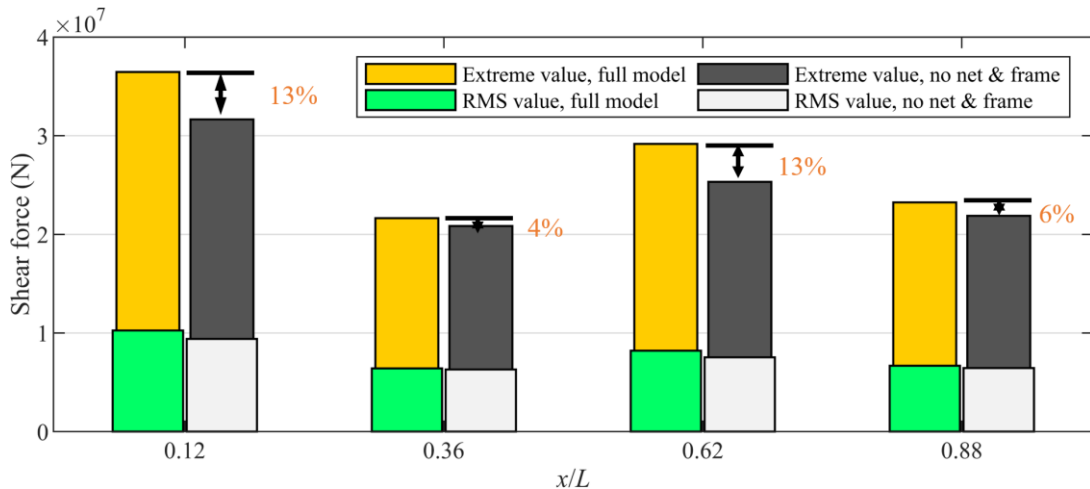


Figure 6-33 Statistical results of cross-sectional vertical shear force at different cross-sections when the hydrodynamic force of the net and steel frame is taken into account under irregular waves

Fig. 6-33 The statistical results of cross-sectional shear force under irregular waves when considering hydrodynamic loads on the net and frame or not

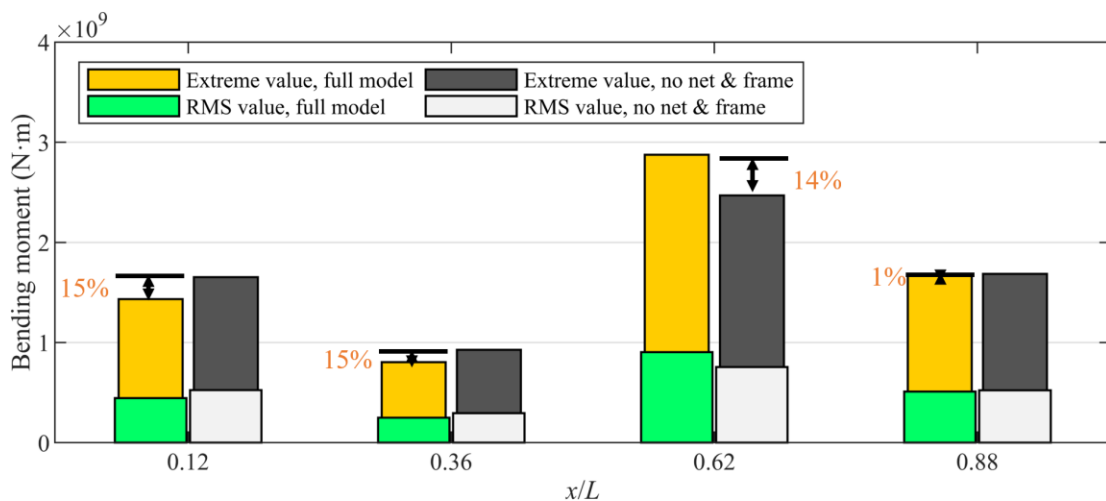


Figure 6-34 Statistical results of vertical bending moments of cross-sections at different cross-sections when the hydrodynamic forces of the net and steel frame are taken into account under irregular waves

Fig. 6-34 The statistical results of cross-sectional vertical bending moment under irregular waves when considering hydrodynamic loads on the net and frame or not

## 6.7 Summary of this chapter

This chapter proposes a new numerical method for considering the hydroelastic sound of large cages under the influence of disturbed wave fields

should be analyzed. Firstly, based on the multi-body hydrodynamics, the wave excitation force, additional mass and wave damping of the discrete module system in the wave domain are calculated in the frequency domain, and the velocity transfer function of the wave field is obtained, which is used to solve the hydrodynamic load of the net coat and steel frame under the action of the disturbed wave field in the time domain. Then, the equivalent beam structure model of the large cage is established to calculate the hydroelastic response of the buoy, and the master-slave constraint and the steel frame-mesh model are used for dynamic coupling, and the hydroelastic model of the large cage based on the method of equivalent beam connection multi-rigid body module is established, which is used to carry out the analysis of the hydroelastic response of the large cage in the time domain. According to the results of the analysis, the following conclusions are obtained:

(1) Compared with the results of the elastic model, the vertical displacement of different cross-section positions will be significantly reduced under the rigid model. As  $X/L$  increases, the difference in vertical displacement between the rigid and elastic models decreases. For the cross-sectional shear force and bending moment, the results under the rigid model will increase significantly, especially under irregular waves. From the perspective of structural strength checking, the results of strength verification using the rigid model are biased towards safety, but from the perspective of cost control, the analysis of the elastic model is conducive to eliminating structural redundancy and reducing the construction cost.

(2) There is no significant difference in the tension of the net under different cross-sectional stiffnesses, and the cross-sectional elasticity of the main structure of the cage has no significant effect on the tension of the net coat. Therefore, from the perspective of mesh strength checking, the influence of the elastic deformation of the main structure on the results can be ignored in the analysis, so as to achieve the purpose of optimizing the verification method.

(3) When the damping effect of the hydrodynamic load of the net and steel frame is not considered, the vertical motion of the cage will increase significantly under different wave frequencies, and it also has a certain influence on the cross-sectional shear force and vertical bending moment, but the influence is limited. With the increase of cross-section stiffness, the vertical response of the cage will gradually decrease and eventually tend to a stable value, while the cross-section shear force and vertical bending moment will gradually increase to a constant value with the increase of cross-section stiffness. Therefore, reducing the cross-section stiffness will significantly reduce the cross-section load of the cage.

(4) Appropriately reducing the number of modules of the buoy will improve the calculation efficiency and maintain the accuracy of the cage cross-sectional load and motion response to a certain extent. However, due to the reduction of the number of modules, the accuracy of the description of the distribution characteristics of the cross-section load and motion response along the axial direction decreases. By calculating the response in the

irregular wave of the cage by reducing the number of modules, it can be seen that the net coat and the steel frame have a significant amplification effect on the vertical response of the cage, but the influence on the cross-sectional load is not obvious, which is consistent with the results of the regular wave.